A Random Channel Sounding Decision Feedback Receiver for Two-way Relay Communication with Pilot-less Orthogonal Signaling and Physical Layer Network Coding

by

Xiaobin Li

B.A.Sc(Electronic Engineering), Simon Fraser University, 2012

Thesis Submitted in Partial Fulfillment of the
Requirements for the Degree of
Master of Applied Science

in the
School of Engineering Science
Faculty of Applied Science

Approval

Name: **Xiaobin Li**

Degree: **Master of Applied Science**

Title: **A Random Channel Sounding Decision Feedback Receiver for Two-way Relay Communication with Pilot-less Orthogonal Signaling and Physical Layer Network Coding**

Examining Committee: **Chair:** Jie Liang

                                 Assoicate Professor

Paul Ho
Senior Supervisor
Professor

Rodney Vaughan
Supervisor
Professor

Daniel Lee
Internal Examiner
Professor

2015-05-23

Date Defended/Approved:

.

Abstract

Cooperative/relay communication system is an active field of research as it promises extended coverage in weak reception areas, for example at cell edges. Furthermore, with physical-layer network coding (PNC) in a two-way relaying (TWR) setting, the transmission rate of the system can be restored back to unity (one packet of data per unit time), just like in conventional point-to-point transmission. This dissertation addresses the issue of signal detection in a two-phase (2P) TWR communication system that employs pilot-less orthogonal modulation and physical network coding operating in a time-selective Rayleigh fading environment. We first introduce a partial-coherent receiver for detecting (at the relay) the modulo-M sum symbol of the uplink pilot-less orthogonal modulations. Through clever exploitation of the orthogonal property of the modulation, this receiver is able to provide a 3 dB improvement in power efficiency over standard non-coherent detector even in the absence of pilot symbols. To further increase the receiver performance, we propose a novel decision feedback (DFB) receiver built upon the partial-coherent detector. The proposed DFB receiver provides another 6 dB improvement in power efficiency over the already impressive partial-coherent detector and attains a performance very close to that of the ideal coherent detector. It exploits the fact that when the uplink symbols from the users are different, then the fading gains affecting these symbols can be separated and individually tracked at the relay. In essence, the proposed DFB receiver performs random channel sounding even though no actual pilots are transmitted. The channel estimates obtained this way can then be used subsequently in a coherent detector to improve the reliability of the relay's detected data. To further demonstrate the usefulness of the proposed DFB receiver, we compare it against a similar 2P-TWR system that employs differential PSK (DPSK) in the uplink and decision-feedback multiple-symbol differential detection at the relay. We found that the proposed pilot-less orthogonal modulation system can actually attain a significantly lower bit-error-rate (BER) than its DPSK counterpart. For static fading and a BER of 10^{-3}, the signal-to-noise ratio gap between the two approaches is 1 dB in the binary case,

Abstract

Cooperative/relay communication system is an active field of research as it promises extended coverage in weak reception areas, for example at cell edges. Furthermore, with physical-layer network coding (PNC) in a two-way relaying (TWR) setting, the transmission rate of the system can be restored back to unity (one packet of data per unit time), just like in conventional point-to-point transmission. This dissertation addresses the issue of signal detection in a two-phase (2P) TWR communication system that employs pilot-less orthogonal modulation and physical network coding operating in a time-selective Rayleigh fading environment. We first introduce a partial-coherent receiver for detecting (at the relay) the modulo-M sum symbol of the uplink pilot-less orthogonal modulations. Through clever exploitation of the orthogonal property of the modulation, this receiver is able to provide a 3 dB improvement in power efficiency over standard non-coherent detector even in the absence of pilot symbols. To further increase the receiver performance, we propose a novel decision feedback (DFB) receiver built upon the partial-coherent detector. The proposed DFB receiver provides another 6 dB improvement in power efficiency over the already impressive partial-coherent detector and attains a performance very close to that of the ideal coherent detector. It exploits the fact that when the uplink symbols from the users are different, then the fading gains affecting these symbols can be separated and individually tracked at the relay. In essence, the proposed DFB receiver performs random channel sounding even though no actual pilots are transmitted. The channel estimates obtained this way can then be used subsequently in a coherent detector to improve the reliability of the relay's detected data. To further demonstrate the usefulness of the proposed DFB receiver, we compare it against a similar 2P-TWR system that employs differential PSK (DPSK) in the uplink and decision-feedback multiple-symbol differential detection at the relay. We found that the proposed pilot-less orthogonal modulation system can actually attain a significantly lower bit-error-rate (BER) than its DPSK counterpart. For static fading and a BER of 10 3 , the signal-to-noise ratio gap between the two approaches is 1 dB in the binary case,and 8 dB in the quaternary case. These gaps increase further with time-selective fading. Based on the result obtained from the new proposed DFB receiver, the overall decision feedback methodology has strong potential for applications in other similar systems, and it worth being studied further and refined.

This page intentionally left blank.

Table of Contents

List of Tables

List of Figures

List of Acronyms

Term	Initial components of the term
2P	Two-phase
3P	Three-phase
4P	Four-phase
AaF	Amplify-and-forward
ANC	Analog network coding
AWGN	Additional white Gaussian noise
BER	Bit-error-rate
BSNR	Bit signal-to-noise ratio
CF	Characteristic function
CSI	Channel state information
DaF	Decode-and-forward
DFB	Decision feedback
DPSK	Differential phase-shift-keying
FC	Full-Coherent
FSK	Frequency-shift-keying
i.i.d	Independent and identically distributed
LS	Least square
MAD	Multiple –and-add
MMSE	Minimum-mean-square-error
MSDD	Multiple-symbol differential detector
NB	Natural-binary
NC	Non-coherent
NMSE	Normalized mean-square error
NSE	Normalized square error
PC	Partial-coherent
PEP	Pairwise error probability
PNC	Physical-layer network coding

PNCF	Physical-layer network coding over finite field
PNCI	Physical-layer network coding over an infinite field
PS	Per-symbol
PSK	Phase-shift-keying
Res	Residue
SNC	Straightforward network coding
SNR	Signal-to-noise ratio
SSNR	Symbol signal-to-noise ratio
TWR	Two-way relaying
UWB	Ultra-wideband

List of Symbols

Symbol	Definition
Φ	Waveforms set
$s_l(t), l = A, B$	Source signals from user A/B
$g_l(t)$	Complex uplink channel gain
$n(t)$	White additional Gaussian noise at the relay receiver
$r(t)$	Received signal at the relay
$R(\tau)$	Autocorrelation function
$J_0(\cdot)$	Bessel function of the first kind of order zero
f_d	Doppler frequency
$s_l[k], l = A, B$	Users A/B' discrete-time data symbol in k^{th} symbol interval
$g_l[k]$	The fading gains in the kth interval
$u[k]$	The sum fading gains in the kth interval
γ_s	The symbol signal-to-noise ratio
γ_b	The bit signal-to-noise ratio
$c[k]$	The network-coded symbol
$v[k]$	The difference fading gains in the kth interval
N_0	Noise variance
σ_g^2	Variance of uplink gain
$\mathbf{\Phi}_{I,J}$	Covariance matrix
d_H	Hamming distance
M	Modulation size
D	Quadratic form
$\|\cdot\|$	Determinant
S	Symbol set at the logic level
$x_l[k], l = A, B$	Differentially encoded transmitted symbols

K_T	Threshold value for decision feedback
$diag(\cdot)$	Diagonal Matrix
Δ	Phase offset
$\tilde{s}$	Alternative symbol
$\hat{u}[k]$	Estimate of the sum fading gain in the kth interval
$\boldsymbol{\varphi}_k$	The kth row of the covariance matrix.
$\varepsilon_0^2[k]$	Mean square error in the kth symbol interval
ε_N^2	Normalized mean square error
$\hat{g}_i, i = A, B$	Final channel estimate
$\tilde{g}_i, i = A, B$	Initial channel estimate
$O(\cdot)$	Complexity
χ_N^2	The per-symbol normalized square error across a block of N symbols
$\chi^2[k]$	Normalized square error in the kth symbol interval
η	Transmission rate
N	Processing block size
K	Observation interval
T	Symbol interval

Chapter 1.

Introduction

1.1. Literature Review

Signal transmitted over wireless communication channels are commonly plagued by fading, shadowing or path loss. In recent years, cooperative communication [1]-[4] has been widely acknowledged by the wireless communication industry as a promising technology to combat these impairments, by involving one or more relays to assist in transmission. According to [5], relay promises extended coverage in weak reception areas, e.g relay provides better performance for out of coverage end user than no relay. Also, Comparing to conventional point-to-point transmission, using relay leads to shortening the transmission distance at each time, and the average power loss from the source to the final destination can be sufficiently reduced. In [2], it is pointed out that two common relaying protocols, namely, decode-and-forward (DaF) and amplify-and-forward (AaF), can be used to achieve cooperative diversity. They have been studied and their performance evaluated in [3]. In DaF, the cooperative relay detects the received data, remodulates, and then broadcasts the remodulated signal to the destination. In AaF, there is no decision made at the relay. The relay simply scales and retransmits the received signal in the final phase. Comparing the AaF method to DaF method, the AF relay has cost effective implementation complexity as the demodulation and remodulation steps can be bypassed; but at the same time, it also forward some disturbance, such as fading and noise, to the user's terminal. In contrast, a DaF relay attempts to remove these disturbances when it makes decisions at the relay.

In earlier research in cooperative communication, only one-way relay was considered. Given a half-duplex relay, a cooperative communication system with a single, always active relay requires two transmission phases to transmit one unit of data from the source terminal to the receiver terminal. In the other words, the transmission rate of a

cooperative communication system, η, is half the value of conventional non-cooperative transmission. In order to improve the transmission efficiency, two-way relaying (TWR) [6] was proposed.

TWR communication is a transmission methodology that enables two users, A and B, to exchange information through a relay R. TWR networks can be classified according to the number of transmission phases. For example, four-phase two-way relaying (4P-TWR) with a traditional non-network-coding approach [7] is interference-free but requires four orthogonal time slots to exchange two packets of data, one in each direction. The throughput is thus identical to one-way relaying, i.e. an $\eta = 1/2$. This approach is also referred to as Traditional Scheme in some <mark>of the</mark> literatures [6, 8].

Comparing to 4P-TWR, three-phase two-way relaying (3P-TWR) employing bit-level network coding [8]-[9] is proposed to increase the throughput. In 3P-TWR, the uplink signal from each user to the relay does not interfere with the other. This allows the relay to easily decode the data symbols (s_A and s_B) from the users separately. In the downlink, the users' signals are mixed, for example using modulo addition of their data $s_A \oplus s_B{}^1$, and broadcasted back to the users. By doing so, both users A and B can recover each other data packets while reducing the number of transmission phases in the traditional approach by one. The transmission rate of this scheme is 2/3, or $\eta = 2/3$. In the literature, this approach is sometimes referred to as straightforward network coding (SNC); see for example [7] [11].

To further improve the efficiency, physical-layer network coding (PNC) [10] [11] is used to further reduce the number of transmission phases down to two. In a two-phase two-way relaying (2P-TWR) system with PNC, both mutual interference in the uplink transmission and signal mixing in the downlink are allowed so that the two users can transmit their data to the relay simultaneously. It means that the transmission rate of

---

^{1} $\oplus$ Denotes bit-wise mod-M addition of signal s_A and s_B

communication can be restored to 1, just ==as== that in conventional non-cooperative transmission. ==It is a simple fact in physics that when two uplink EM wave signals come together within the same physical space, they add. This mixing of EM wave signals is a form of network coding, performed by nature [7].== The relay deduces the downlink mixed signal from the superimposed waveforms and broadcasts in the second transmission phase. The relay can adopt either AaF or DaF in a PNC setting. The former approach is referred to as *analog network coding* (ANC) [12] and PNC *over an infinite field* (PNCI) in [13]. The latter is referred to as PNC *over finite field* (PNCF) in [13].

The three types of TWR networks mentioned above are summarized in Figure 1 below. Since 2P-TWR has the highest transmission rate, we focus on this particular protocol in the thesis
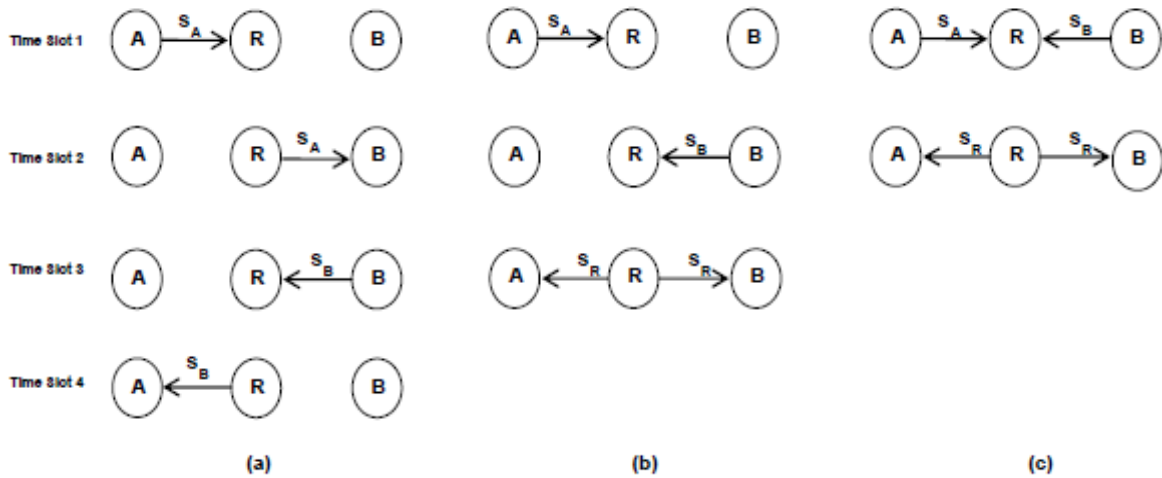
Fig. 1.1: Transmission timing in TWR communication systems with (a) traditional scheme, (b) straightforward network coding, and (c) physical network coding.

On the detection issue in 2P-TWR systems, if perfect channel state information (CSI) of all the links in the system is available at the users' terminals, for example, via embedded pilot symbols, then the useful data in the received downlink signal can be detected at the user's terminals by using self-interference cancellation followed by coherent detection. Similarly, if the uplinks' CSI is available at the relay, a DaF-based

3

2P-TWR can use a coherent multi-user detector to select proper quantized symbols from its constellation for the broadcasting phase. The training and channel estimation issues associated with pilot-based coherent detectors in TWR can be found in [14]-[15]. On the other hand, if CSI is not available, differential detection [16]-[18] is used instead. Differential detection doesn't require pilot symbol and it is relatively simple to implement. However, the performance of this simple detector would be much worse than that provided by a pilot-aided detector. Furthermore, differential detection is only applicable to phase-shift-keying (PSK) modulation. A third approach is to employ blind or semi-blind channel estimation and detection; see example [19]-[21]. Although the performance of this type of detector can be substantially better than differential detection, it requires extra amount of processing. This could be problematic for DaF, as we would like to keep the relay as simple as possible.

1.2. Motivation and Contribution of the Thesis

There are a number of investigations of TWR communication with PNC in the literature already. Most of their investigations are focus on PSK modulation [15, 17]. In [22]-[23], the authors undertook different modulations, specifically frequency-shift-keying (FSK). They proposed non-coherent detections of FSK in DaF-based TWR networks. However, [22] is restricted to only additive white Gaussian noise channel while [23] designs a very complicated detector. Moreover, [23] is limited to static fading amplitudes, though the phase is allowed to vary randomly.

This thesis investigates the performance of general orthogonal modulations in 2P-TWR communication, with FSK being a special case. Intuitively, the higher dimensionality of orthogonal modulations seems more compatible with the multiple-access nature of PNC than PSK, which will be explained later in the dissertation. Besides, as stated above, they receive much less attention in the literature than PSK modulations. The investigation focuses on the detection of pilot-less uplink orthogonal signals at the relay of a DaF-based 2P-TWR network. The reason why we choose DaF

over AaF is because, as stated in [9, 23], a DaF-based 2P-TWR has a higher sum rate than an AaF-based 2P-TWR. On a similar note, we prefer pilot-less transmission because it does not require any overhead for channel estimation.

In this thesis, we first design a much simpler detector for pilotless orthogonal modulations that achieves the same performance as the more complicated receiver in [23]. A bit-error-rate (BER) analysis of this new detector, for both binary and 4-ary modulations, is performed and the results indicate a 3 dB improvement in signal-to-noise ratio over conventional non-coherent detector, even though no pilot signal is transmitted. Rather than employing this new detector as a stand-alone device, we use it to kick start a decision feedback (DFB) receiver for the purpose of reaching an even better BER performance. We demonstrat that with proper decision-aided channel estimation, the relay DaF receiver can attain a performance that is very close to ideal coherent detection (i.e. perfect CSI), even with time-selective Rayleigh fading. The last contribution of this thesis is to demonstrate the usefulness of the proposed DFB receiver for orthogonal modulations against a multiple-symbol differential detector (MDSS) [16] for differential PSK (DPSK) modulation. Contrary to conventional point-to-point transmission where DPSK always outperforms non-coherent orthogonal modulation in the presence of Rayleigh fading and additive white Gaussian noise [24], we discover that our proposed orthogonal modulation system for 2P-TWR substantially outperforms DPSK with MSDD in a 2P-TWR setting. The gain in power efficiency is 1 dB in the binary case and 8 dB in the quaternary case.

1.3. Thesis Outline

The thesis is organized as follows.

Chapter 2 provides the signal and system model of a 2P-TWR system with PNC and pilot-less orthogonal signaling. Based on the received signal model, three baseline receivers at the relay are considered: the non-coherent detector, the ideal full-coherent

detector, and the proposed partial-coherent detector. The bit-error-rate (BER) performance of the three detectors is analyzed using the pair-wise error event and characteristic function approach, for both binary and quaternary modulations. It was found that with minimal additional processing, the proposed partial-coherent detector provides a 3 dB improvement over the non-coherent detector, even no pilot is transmitted. However, there is still a 7 dB performance gap between the partial-coherent detector and the ideal coherent detector.

The performance gap between the ideal full-coherent detector and our proposed partial-coherent detector leads us to introduce the decision feedback receiver in Chapter 3. As illustrated in this chapter, the proposed decision feedback receiver performs random channel sampling for channel indentification and interpolation for the purpose of the generating channel estimates for a coherent detector. Details about the channel identification, tracking, and interpolation issues are provided in the chapter.

Chapter 4 provides a proper perspective of the performance of the decision feedback receiver in Chapter 3 by comparing it against DPSK with MSDD. The chapter begins with a brief review of the modulation and the structure of a decision feedback-based MSDD. The BER performance of the MSDD is then evaluated via simulation under similar conditions as the ones employed in Chapter 3 for orthogonal modulations. Conclusions are then made about the relative advantages and disadvantages of pilot-less orthogonal modulations and DPSK.

Finally, the last chapter provides the summary of this thesis research as well as suggestions for further investigation.

Chapter 2.

Proposed Partial-coherent Detector for Orthogonal Signaling

This chapter provides the details of how to construct 3 types of detectors at the relay of a TWR system that uses PNC and M-ary orthogonal signalling. These are the standard non-coherent detector and full-coherent detector, and the proposed partial-coherent detector. Section 2.1 sets up the signal and system model of a 2P-TWR system with PNC and M-ary orthogonal signaling. Based on the received signal model, Section 2.2 shows how a non-coherent detector can be constructed if CSI is unavailable, and how coherent detection can be achieved without the aid of pilot symbol by alternating the polarity of one of the users' signal in successive intervals. Section 2.3 lists the main disadvantage of alternating the signal's polarity and then proposes a detector that is able to derive partial channel information without the need to alternate the polarity of any signal. Also included in this section is a BER analysis of this partial-coherent detector. Section 2.4 presents numerical results for the BER performance of the 3 types of detector. Comparisons and conclusions are made in Section 2.5

2.1. Signal and System Model for TWR Network with PNC

We consider a 2P-TWR network with users A and B communicating bilaterally through a half-duplex relay R. The modulation format adopted by both users is M-ary orthogonal modulation with equiprobable waveforms $\Phi \equiv \{ \phi_0(t), \phi_1(t), ... \phi_{M-1}(t) \}$, where $\int_{kT}^{(k+1)T} \phi_i(t)\phi_j^*(t)dt = \delta_{i,j}$, T is the symbol interval, and $\delta_{i,j}$ is the Kronecker delta

function with $\delta_{i,j}=1$ when $i=j$ and $\delta_{i,j}=0$ otherwise. The uplinks (A→R, B→R) and downlinks (R→A, R→B) all exhibit Rayleigh flat fading. In particular, the first transmission phase in the 2-P TWR network is illustrated in Fig 2.1.

AWGN~ $CN(0,N_0)$

R

S_A

S_B

Uplink channel 1

Uplink channel 2

A

B
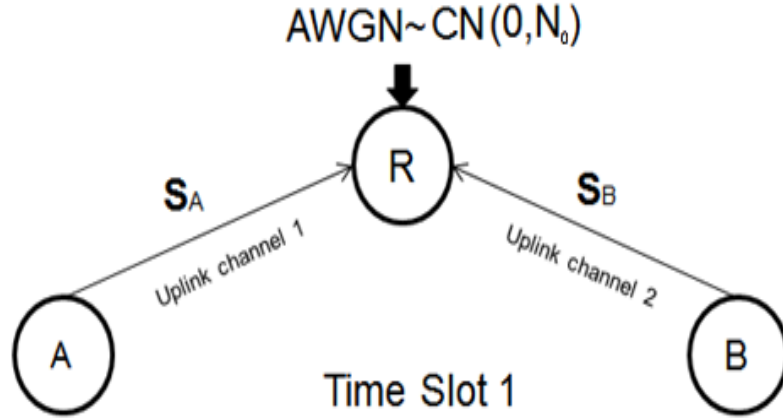
Time Slot 1

Fig. 2.1: The first time slot in a 2P-TWR network.

The signal received at the relay is of the form of

$$r(t) = g_A(t)s_A(t) + g_B(t)s_B(t) + n(t), \qquad nT \leq t < nT + T, \qquad (2.1)$$

where $s_A(t), s_B(t) \in \Phi$ are the source signals, $g_A(t)$ and $g_B(t)$ are $CN(0,\sigma_g^2)$ random processes representing fading in the uplinks, and $n(t)$ is the AWGN at the receiver, whose power spectral density (psd) is N_0. The two fading processes are based on the Jake's channel model with isotropic scattering and vertical polarized antenna. They have an identical autocorrelation function of $R_{g_i}(\tau) = \frac{1}{2}E\left(g_i(t+\tau)g_j^*(t)\right) = \sigma_g^2 J_0(2\pi f_d \tau)$, $i = A, B$, where $J_0(\cdot)$ is the Bessel function of the first kind of order zero, and f_d is the Doppler frequency.

The relay correlates the received signal in (1) with the M orthogonal waveforms in the set Φ, yielding the observations

$$r_i[k] = \int_{kT}^{kT+T} r(t)\phi_j^*(t)dt = g_A[k]\delta_{i,s_A[k]} + g_B[k]\delta_{i,s_B[k]} + n_i[k]; \qquad i = 0,1,...,M-1, \qquad (2.2)$$

where $s_A[k]$ and $s_B[k]$ are users A' and B' equivalent discrete-time data symbols taken from the set $S \equiv \{0,1,...,M-1\}$; $s_A[k] = i$ and $s_B[k] = j$ if only if $s_A(t) = \phi_i(t)$ and $s_B(t) = \phi_j(t)$ in the kth interval, respectively. The terms $g_A[k]$ and $g_B[k]$ are the fading gains in the kth interval, and both $g_A[k]$ and $g_B[k]$ have a common autocorrelation function of $R_{g_j}(\ell) = \frac{1}{2}E(g_j[k+\ell]g_j^*[k]) = \sigma_g^2 J_0(2\pi\ell f_d T)$, $j = A, B$. Finally, $n_i[k] = CN(0, N_0)$ is the noise term of the ith correlator, and all the noise terms are independent and identically distributed (i.i.d). An interesting property of the signal structure in (2) is that the sum correlator output is always the sum fading process plus noise, i.e.

$$\tilde{u}[k] = \sum_{i=0}^{M-1} r_i[k] = g_A[k] + g_B[k] + CN(0, MN_0), \qquad (2.3)$$

irrespective of the transmitted data symbols. This suggests that (2.3) can be used to estimate the sum <mark>complex</mark> fading gain

$$u[k] = g_A[k] + g_B[k]. \qquad (2.4)$$

This observation would be exploited to form the pilot-less coherent detector in Section 2.2 as well as the proposed partial-coherent detector in Section 2.3. Finally, the symbol signal-to-noise ratio (SSNR) is defined as

$$\gamma_s = \sigma_g^2 / N_0, \qquad (2.5)$$

and the bit signal-to-noise ratio (BSNR) is

$$\gamma_b = \gamma_s / \log_2 M. \qquad (2.6)$$

The BER of different detectors will be plotted against γ_b in dB. <mark>In this dissertation, we aim to compare the performances of different modulation schemes in TWR communications, whereas is not between the relay communications versus the conventional point-to-point transmission. Therefore, there is no need to scale SNR further more.</mark>

Upon receiving the signal $r(t)$ in (2.1), the DaF-relay selects a symbol from a pre-defined discrete constellation S_R that best matches $\mathbf{r}[k] = \left[r_0[k], r_1[k], ..., r_{M-1}[k] \right]^T$, the correlators' output in (2.2). In this investigation, the relay continues to use the same M-ary orthogonal modulation, so that, the forwarded symbol is also taken from the set $S \equiv \{0, 1, ... M-1\}$. The mapping of different pairs of ($s_A[k]$, $s_B[k]$) from the Cartesian product $S \times S$ onto the symbols $c[k]$ in S will be done using the natural-binary (NB) mapping. Let $\mathbf{s_A}[k]$ and $\mathbf{s_B}[k]$ be the NB representations of the data symbols $s_A[k]$ and $s_B[k]$. Then the network-coded symbol $c[k]$ is the simply the decimal equivalent of $\mathbf{c}[k] = \mathbf{s_A}[k] \oplus \mathbf{s_B}[k]$. Tables 2.1 and 2.2 provide full details of the mappings in the $M = 2$ and $M = 4$ cases respectively.

Symbol s_A (decimal format)	Symbol s_A as a Binary pattern $\mathbf{s_A}$	Symbol s_B (decimal format)	Symbol s_B as a Binary pattern $\mathbf{s_B}$	Symbol c as a Binary pattern $\mathbf{c} = \mathbf{s_A} \oplus \mathbf{s_B}$	Symbol c (decimal format)
0	0	0	0	0	0
1	1	1	1		
$L_0 = p(\mathbf{r}|(0,0), f(\mathbf{g})) + p(\mathbf{r}|(1,1), f(\mathbf{g}))$					
0	0	1	1	1	1
1	1	0	0		
$L_1 = p(\mathbf{r}|(1,0), f(\mathbf{g})) + p(\mathbf{r}|(0,1), f(\mathbf{g}))$					

Table. 2.1: Mapping of the source symbol pair (s_A, s_B) into the network-coded symbol c for $M = 2$ systems.

Symbol s_A (decimal format) s_A	Symbol s_A as a Binary pattern s_A	Symbol s_B (decimal format)	Symbol s_B as a Binary pattern s_B	Symbol c as a Binary pattern $c = s_A \oplus s_B$	Symbol c (decimal format)
0	(0,0)	0	(0,0)		
1	(0,1)	1	(0,1)	(0,0)	0
2	(1,0)	2	(1,0)		
3	(1,1)	3	(1,1)		
$L_0 = p(\mathbf{r}\,|\,(0,0), f(\mathbf{g})) + p(\mathbf{r}\,|\,(1,1), f(\mathbf{g})) + p(\mathbf{r}\,|\,(2,2), f(\mathbf{g})) + p(\mathbf{r}\,|\,(3,3), f(\mathbf{g}))$					
0	(0,0)	1	(0,1)		
1	(0,1)	0	(0,0)	(0,1)	1
2	(1,0)	3	(1,1)		
3	(1,1)	2	(1,0)		
$L_1 = p(\mathbf{r}\,|\,(0,1), f(\mathbf{g})) + p(\mathbf{r}\,|\,(1,0), f(\mathbf{g})) + p(\mathbf{r}\,|\,(2,3), f(\mathbf{g})) + p(\mathbf{r}\,|\,(3,2), f(\mathbf{g}))$					
0	(0,0)	2	(1,0)		
1	(0,1)	3	(1,1)	(1,0)	2
2	(1,0)	0	(0,0)		
3	(1,1)	1	(0,1)		
$L_2 = p(\mathbf{r}\,|\,(0,2), f(\mathbf{g})) + p(\mathbf{r}\,|\,(2,0), f(\mathbf{g})) + p(\mathbf{r}\,|\,(1,3), f(\mathbf{g})) + p(\mathbf{r}\,|\,(3,1), f(\mathbf{g}))$					
0	(0,0)	3	(1,1)		
1	(0,1)	2	(1,0)	(1,1)	3
2	(1,0)	1	(0,1)		
3	(1,1)	0	(0,0)		
$L_3 = p(\mathbf{r}\,|\,(0,3), f(\mathbf{g})) + p(\mathbf{r}\,|\,(3,0), f(\mathbf{g})) + p(\mathbf{r}\,|\,(1,2), f(\mathbf{g})) + p(\mathbf{r}\,|\,(2,1), f(\mathbf{g}))$					

Table. 2.2: Mapping of the source symbol pair (s_A, s_B) into the network-coded symbol c for $M = 4$ systems.

As shown in the tables, the decision metric associated with each network-coded symbol P, $P = 0,1,...M-1$, is

$$L_P = \sum_{(I,J)\to P} p(\mathbf{r}[k]\,|\,I, J, f(\mathbf{g}));\qquad(2.7)$$

where $p(\mathbf{r}[k]\,|\,I,J,f(\mathbf{g}))$ is the probability density function (pdf) of the received vector $\mathbf{r}[k]$ if I and J are the transmitted symbols and when $f(\mathbf{g})$, $\mathbf{g}=(g_A,g_B)$, is the available CSI. The sum in (5) is taken over all pairs of (I,J) that are mapped into the symbol P from the relay's constellation S_R. The decoded symbol $\hat{c}[k]$ at the relay is the one that has the largest metric

$$\hat{c}[k]=\arg\max_{P\in\{0,1,...,M\text{-}1\}} L_P[k]. \tag{2.8}$$

In the following sections, three types of detectors will be considered: standard non-coherent detector, a pilot-less coherent detector, and the proposed pilot-less partial-coherent detector.

2.2. Non-Coherent and Coherent Detectors

Two standard detectors are presented in this section to serve as performance benchmarks. These are the non-coherent detector and the ideal full-coherent detector. They correspond to extremes of CSI availability: none and full knowledge of the channel gains.

2.2.1.　Non-coherent Detector - No CSI Available

When $g_A[k]$ and $g_B[k]$ are not known, $f(\mathbf{g})$ is simply the empty set. In the absence of any CSI, the non-coherent detector at the relay simply uses the data-dependent variances of the received vector $\mathbf{r}[k]=\left[r_0[k],r_1[k],...,r_{M\text{-}1}[k]\right]^T$ in (2.2) to identify the uplink data symbols I and J. Since such a detector makes symbol-by-symbol decisions, we can ignore the time index k in the receive vector $\mathbf{r}[k]$.

In the absence of CSI and when $s_A[k] = s_B[k] = I$, then the I-th correlator output, r_I, is simply treated as a zero-mean complex Gaussian random variable with a variance of $2\sigma_g^2 + N_0$. All the remaining r_m, $m \neq I$, have a common variance of N_0; refer to (2.2). Since the noise components in the receive vector $\mathbf{r} = [r_1, r_2, ..., r_M]^T$ are independent, its pdf when conditioned on the data symbols becomes

$$p(\mathbf{r} \mid I, J) = \begin{cases} \dfrac{1}{(2\pi)^M (2\sigma_g^2 + N_0)(N_0)^{M-1}} \exp\left\{ -\dfrac{|r_I|^2}{2(2\sigma_g^2 + N_0)} \right\} \exp\left\{ -\displaystyle\sum_{\substack{i=0 \\ i \neq I}}^{M-1} \dfrac{|r_i|^2}{2N_0} \right\}, & I = J; \\[3em] \dfrac{1}{(2\pi)^M (\sigma_g^2 + N_0)^2 (N_0)^{M-2}} \exp\left\{ -\dfrac{|r_I|^2 + |r_J|^2}{2(\sigma_g^2 + N_0)} \right\} \exp\left\{ -\displaystyle\sum_{\substack{i=0 \\ i \neq I, J}}^{M-1} \dfrac{|r_i|^2}{2N_0} \right\}, & I \neq J. \end{cases}$$

$$(2.9)$$

The decision metric for this non-coherent detector is obtained by substituting (2.9) into (2.7). The decoded symbol $\hat{c}$ is decided based on (2.8).

Although the above non-coherent detector is easy to implement, it does not provide the best BER performance, as we shall see later on in this chapter.

2.2.2.   Full Knowledge of the Fading Gains

To achieve a better BER performance, a full-coherent detector can be considered, if CSI is available. Specifically, if the individual fading gains $g_A[k]$ and $g_B[k]$ can be accurately estimated by the relay's receiver, coherent detection can be performed. Below is a method to estimate these fading gains without resorting to transmit any pilot symbol.

As mentioned in (2.3), the sum of the components in the receive vector $\mathbf{r}[k]$ always provides a noisy copy of the sum fading gain $u[k]$ in (2.4). The result suggests that, in the case of static fading, u can be estimated by simply taking the average of the sums

$\sum_{i=0}^{M-1} r_i[k]$ over a number of consecutive symbol intervals. In the event of time-selective fading, the sums $\sum_{i=0}^{M-1} r_i[k]$ at different symbol intervals are passed to a minimum-mean-square-error (MMSE) estimator to generate the final estimate of $\mathbf{u} = [u[1], u[2],..., u[N]]^T$. Details of MMSE estimation will be provided in next chapter. Since each sum $\sum_{i=0}^{M-1} r_i[k]$ serves as an implicit pilot symbol [25], the estimate of $u[k]$ obtained this way can be very accurate, even with time-selective fading, as we shall we see in the next chapter. For this reason, we assume, perfect estimation here.

While knowing the sum fading gain in (2.4) is useful, it alone does not lead to a coherent detector. As mentioned earlier, coherent detection requires knowledge of both $g_A[k]$ and $g_B[k]$. To extract this information from the received signal without resorting to transmitting pilot symbols, we can consider alternating the polarity of user B's signal from one symbol interval to the next, i.e. allowing B to adopt the constellation $\{v_0, v_1,..., v_{M-1}\}$ in the even symbol intervals and the constellation $\{-v_0, -v_1,..., -v_{M-1}\}$ in the odd intervals. In doing so, the signal components of the received vectors in the odd intervals in (2.2) can be rewritten as

$$r_i[k] = \int_{kT}^{kT+T} r(t)j^*(t)dt = g_A[k]\delta_{i,s_A[k]} - g_B[k]\delta_{i,s_B[k]} + n_i[k]; \qquad k \text{ is odd}, \ i=0,1,...,M-1.$$

(2.10)

According to (2.10), the sum correlator output in the odd intervals is always the difference fading process plus the noise term

$$\tilde{v}[k] = \sum_{i=0}^{M-1} r_i[k] = g_A[k] - g_B[k] + CN(0, MN_0); \qquad k \text{ is odd}. \qquad (2.11)$$

At this point, we can deduce that (in the case of static fading) the channel estimates requires for coherent detection can be obtained from the sum and difference of

$\left(\overline{\sum_{i=0}^{M-1} r_i[k]}\right)_{k \text{ even}}$ and $\left(\overline{\sum_{i=0}^{M-1} r_i[k]}\right)_{k \text{ odd}}$, where $\left(\overline{\sum_{i=0}^{M-1} r_i[k]}\right)_{k \text{ even}}$ and $\left(\overline{\sum_{i=0}^{M-1} r_i[k]}\right)_{k \text{ odd}}$ are the

averages of $\sum_{i=0}^{M-1} r_i[k]$ over the even and odd intervals. In the case of time-selective

fading, the sum fading gain $\mathbf{u} = [u[1], u[2], ..., u[N]]^T$ and the difference fading gain

$\mathbf{v} = [v[1], v[2], ..., v[N]]^T$ can be estimated by passing the $\left(\sum_{i=0}^{M-1} r_i[k]\right)_{k \text{ even}}$ and the

$\left(\sum_{i=0}^{M-1} r_i[k]\right)_{k \text{ odd}}$ to interpolators designed based on the minimum mean square error

criterion. The detail of this MMSE interpolation is presented in the next chapter.

Assuming perfect channel estimation is achieved through the above procedure, i.e.
$f(\mathbf{g})=\mathbf{g}$, we can ignore the time index k in the receive vector
$\mathbf{r}[k] = [r_0[k], r_1[k], ..., r_{M-1}[k]]^T$ in (2.2). When g_A and g_B are known, and when
$s_A[k] = s_B[k] = I$, then r_I has a mean of $g_A + g_B$ and a variance of N_0. As for the
remaining r_m, $m \neq I$, they all have zero mean and variance of N_0; refer to (2.2). On the
other hand, when g_A and g_B are known but $s_A[k] = I$ and $s_B[k] = J$, then r_I has a mean
of g_A and a variance of N_0, r_J has a mean of g_B and a variance of N_0, and all the
remaining r_m, $m \neq I$, $m \neq J$, have zero mean and a common variance of N_0. Since all
the noise terms in the receive vector $\mathbf{r} = [r_1, r_2, ..., r_M]^T$ are independent, its pdf when
conditioned on the data symbols and the CSI is thus

$$p(\mathbf{r} \mid I, J, (g_A, g_B)) = \begin{cases} \dfrac{1}{(2\pi)^M (N_0)^M} \exp\left\{-\dfrac{|r_I - g_A - g_B|^2}{2N_0}\right\} \exp\left\{-\sum_{\substack{i=0 \\ i \neq I}}^{M-1} \dfrac{|r_i|^2}{2N_0}\right\}, & I = J; \\[2em] \dfrac{1}{(2\pi)^M (N_0)^M} \exp\left\{-\dfrac{|r_I - g_A|^2 + |r_J - g_B|^2}{2N_0}\right\} \exp\left\{-\sum_{\substack{i=0 \\ i \neq I, J}}^{M-1} \dfrac{|r_i|^2}{2N_0}\right\}, & I \neq J. \end{cases}$$

(2.12)

15

Similar to the non-coherent detector, the decoded symbol $\hat{c}$ is decided by substituting (2.12) into (2.7) and (2.8).

2.3. Partial-coherent Detection

The pilot-less coherent detection strategy presented in the last section is achieved by alternating the polarity of the constellation of one of the users from one symbol interval to the next. However, these polarity changes or switching will increase the transmission bandwidth, as the spectrum of the switched signal is the convolution of the spectrum of the non-switched signal and a $\text{sinc}^2(\cdot)$ function. A good compromise appears to be a detector that simply makes use of the knowledge of the sum fading gain in (2.4) during detection. We call this a partial-coherent detector. Intuitively, the error performance of this new detector will be in-between those of the ideal full-coherent and non-coherent detectors. We first derive below the decoding metric of this partial-coherent detector, followed by a general error probability analysis that is applicable to all three detectors.

It should be noted that the term "partial-coherent detection" is used commonly in the literature to refer to differential detection of differentially encoded PSK (DPSK). In this thesis, partial-coherent detection refers to a detector that has knowledge of the sum fading gain but not individual fading gains in the uplink of a TWR system.

2.3.1. The optimal partial-coherent detector

In deriving the optimal partial-coherent detector, we assume the sum fading gain $u[k] = g_A[k] + g_B[k]$ is estimated perfectly and as such, we drop the index k in the discussion. Practical estimation of the sum fading gain will be addressed in the next chapter.

When u is known, and when $s_A[k] = s_B[k] = I$, then r_I is complex Gaussian with a mean of $u = g_A + g_B$ and a variance of N_0. All the remaining r_m, $m \neq I$, have zero mean and variance of N_0. As a result, the conditional pdf of $\mathbf{r} = [r_1, r_2, ..., r_M]^T$ given u for this scenario is

$$p(\mathbf{r} \mid I = J, u) = \frac{1}{(2\pi)^M (N_0)^M} \exp\left\{ -\frac{|r_I - u|^2}{2N_0} \right\} \exp\left\{ -\sum_{\substack{i=0 \\ i \neq I}}^{M-1} \frac{|r_i|^2}{2N_0} \right\}, \tag{2.13}$$

Basically, this scenario is identical to that of the ideal coherent detector.

For the scenario of different transmitted symbols, say $s_A[k] = I$ and $s_B[k] = J$, then $r_I = g_A + n_I$, $r_J = g_B + n_J$, and $r_m = n_m$, $m \neq I, J$. Knowing $u = g_A + g_B$ will provide partial knowledge of the means and variances of the complex Gaussian random variables r_I and r_J, but none about the rest of the received samples. Let

$$\mathbf{r}_{I,J} = \begin{pmatrix} r_I \\ r_J \end{pmatrix} = \begin{pmatrix} g_A \\ g_B \end{pmatrix} + \begin{pmatrix} n_I \\ n_J \end{pmatrix}, \tag{2.14}$$

and define

$$\mathbf{\varphi} = \tfrac{1}{2} E\left[\mathbf{r}_{I,J} u^* \right] = \sigma_g^2 \cdot \mathbf{1}, \tag{2.15}$$

$$\mathbf{\Phi} = \tfrac{1}{2} E\left[\mathbf{r}_{I,J} \mathbf{r}_{I,J}^\dagger \right] = \left(\sigma_g^2 + N_0 \right) \mathbf{I}_2, \tag{2.16}$$

where $\mathbf{1} = [1,1]^T$ and $\mathbf{I}_2$ is an identity matrix of size 2. It can be easily shown that given $u = g_A + g_B$, $\mathbf{r}_{I,J}$ has a <mark>conditional</mark> mean of

$$\mathbf{m}_{I,J} = \left(\frac{\mathbf{\varphi}}{\sigma_u^2} \right) \cdot u = \frac{1}{2} \mathbf{1} \cdot u, \tag{2.17}$$

17

and a covariance matrix of

$$\boldsymbol{\Phi}_{I,J} = \boldsymbol{\Phi} - \boldsymbol{\varphi} \cdot \frac{1}{\sigma_u^2} \boldsymbol{\varphi}^\dagger = \tfrac{1}{2}\sigma_g^2 \begin{pmatrix} 1 & -1 \\ -1 & 1 \end{pmatrix} + N_0 \mathbf{I}_2 . \tag{2.18}$$

Note that the inverse of $\boldsymbol{\Phi}_{I,J}$ is

$$\boldsymbol{\Phi}_{I,J}^{-1} = \frac{1}{N_0\left(\sigma_g^2 + N_0\right)} \cdot \left(\tfrac{1}{2}\sigma_g^2 \mathbf{U}_2 + N_0 \mathbf{I}_2\right), \tag{2.19}$$

where $\mathbf{U}_2$ is an all-one matrix of size 2. Since u provides no information on the remaining received samples, this means the conditional pdf of $\mathbf{r} = [r_1, r_2, ..., r_M]^T$ given $I \neq J$ and u is

$$p(\mathbf{r} \mid I \neq J, u) =$$

$$\frac{1}{(2\pi)^M (\sigma_g^2 + N_0)(N_0)^{M-1}} \exp\left\{ -\frac{\left(\mathbf{r}_{I,J} - \tfrac{1}{2}u\mathbf{1}_2\right)^\dagger \left(\tfrac{1}{2}\sigma_g^2 \mathbf{U}_2 + N_0 \mathbf{I}_2\right)\left(\mathbf{r}_{I,J} - \tfrac{1}{2}u\mathbf{1}_2\right)}{2N_0(\sigma_g^2 + N_0)} \right\} \exp\left\{ -\sum_{\substack{i=0 \\ i \neq I,J}}^{M-1} \frac{|r_i|^2}{2N_0} \right\}, \quad I \neq J, \tag{2.20}$$

Summarizing the results of the two scenarios, the condition pdf of the correlators' output is

$$p(\mathbf{r} \mid I, J, u) =$$

$$\begin{cases} \dfrac{1}{(2\pi)^M (N_0)^M} \exp\left\{ -\dfrac{|r_I - u|^2}{2N_0} \right\} \exp\left\{ -\displaystyle\sum_{\substack{i=0 \\ i \neq I}}^{M-1} \dfrac{|r_i|^2}{2N_0} \right\}, & I = J; \\[4ex] \dfrac{1}{(2\pi)^M (\sigma_g^2 + N_0)(N_0)^{M-1}} \exp\left\{ -\dfrac{\left(\mathbf{r}_{I,J} - \tfrac{1}{2}u\mathbf{1}_2\right)^\dagger \left(\tfrac{1}{2}\sigma_g^2 \mathbf{U}_2 + N_0 \mathbf{I}_2\right)\left(\mathbf{r}_{I,J} - \tfrac{1}{2}u\mathbf{1}_2\right)}{2N_0(\sigma_g^2 + N_0)} \right\} \exp\left\{ -\displaystyle\sum_{\substack{i=0 \\ i \neq I,J}}^{M-1} \dfrac{|r_i|^2}{2N_0} \right\}, & I \neq J, \end{cases} \tag{2.21}$$

Substituting (2.21) into (2.7) generates the optimal decision metric for the proposed partial-coherent detector.

2.3.2. BER Upper bounds of the three Detectors

The decision metrics of the three detectors presented in the previous sections can all be expressed in terms of quadratic forms of complex Gaussian random variables. As a result, their error performance can be easily analyzed using the characteristic function and residue approach. Since CSI is either known perfectly or not at all, the time index k can be ignored in the analysis.

To begin, upper bounds on the symbol error rate (SER), P_s, and the BER, P_b, of the three detectors mentioned in (2.9), (2.12) and (2.21), can be derived using the pairwise error probability (PEP) approach. Specifically,

$$P_s \leq \frac{1}{M^2} \sum_{(s_A, s_B)} \sum_{\substack{(\tilde{s}_A, \tilde{s}_B) \\ \tilde{c} \neq c}} \Pr\left[p(\mathbf{r}|s_A, s_B, f(\mathbf{g})) < p(\mathbf{r}|\tilde{s}_A, \tilde{s}_B, f(\mathbf{g})) \right] \qquad (2.22)$$

and

$$P_b \leq \frac{1}{M^2 \log_2 M} \sum_{(s_A, s_B)} \sum_{\substack{(\tilde{s}_A, \tilde{s}_B) \\ \tilde{c} \neq c}} d_H(\tilde{c}, c) \Pr\left[p(\mathbf{r}|s_A, s_B, f(\mathbf{g})) < p(\mathbf{r}|\tilde{s}_A, \tilde{s}_B, f(\mathbf{g})) \right], \quad (2.23)$$

where (s_A, s_B) are the data symbols whose network-coded symbol is c, $(\tilde{s}_A, \tilde{s}_B)$ represents an alternative pair with a network-coded symbol $\tilde{c}$, $d_H(\tilde{c}, c)$ is the Hamming distance between c and $\tilde{c}$, $p(\mathbf{r}|s_A, s_B, f(\mathbf{g})) < p(\mathbf{r}|\tilde{s}_A, \tilde{s}_B, f(\mathbf{g}))$ denotes a pairwise error event with $p(\mathbf{r}|I, J, f(\mathbf{g}))$ being the conditional pdf given in either (2.9), (2.12) or (2.21), and the inner sum is over all pairs of $(\tilde{s}_A, \tilde{s}_B)$ whose network-coded symbol $\tilde{c}$ differs from c. The pairwise error events can be classified according to $d_H((s_A, s_B),(\tilde{s}_A, \tilde{s}_B))$, the Hamming distance between the two-tuples (s_A, s_B) and $(\tilde{s}_A, \tilde{s}_B)$, and by whether the transmitted symbols of the two users, and those in the alternative, are identical or different; refer to Fig. 2.1. The classifications shown in the

diagram can be applied to the binary ($M=2$) and quaternary ($M=4$) cases, with types I and III error events specific to the binary cases.
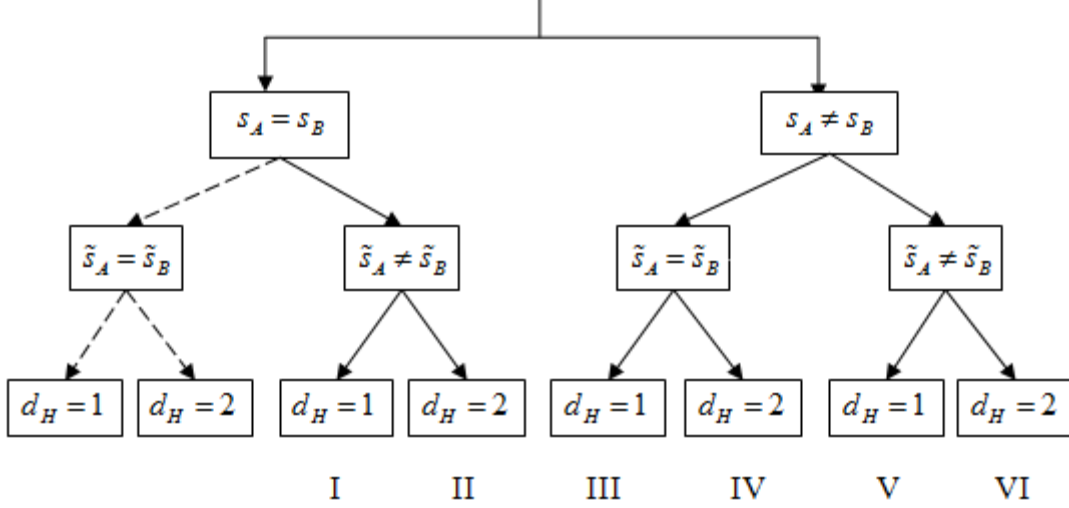
Fig 2.2: Classification of pairwise error events; d_H is the Hamming distance between the two-tuples (s_A, s_B) and $(\tilde{s}_A, \tilde{s}_B)$; the two events at the bottom level of the tree represented by dashed lines are NON error events according to the mappings in Tables 2.1 and 2.2

Since the scenario $s_A=s_B$ and $\tilde{s}_A=\tilde{s}_B$ does not constitute an error event (see Tables 2.1 and 2.2), there are only six types of pairwise error events. Without loss of generality, we set (s_A, s_B) and $(\tilde{s}_A, \tilde{s}_B)$ to some convenient values to reflect the case under consideration. For the $M=2$ and $M=4$ cases, there are a total of six types of pairwise error events of the form:

I. $p(\mathbf{r}\,|\,s_A=0,\ s_B=0,\ f(\mathbf{g}))< p(\mathbf{r}\,|\,\tilde{s}_A=0,\ \tilde{s}_B=1,\ f(\mathbf{g}))$,

II. $p(\mathbf{r}\,|\,s_A=0,\ s_B=0,\ f(\mathbf{g}))< p(\mathbf{r}\,|\,\tilde{s}_A=1,\ \tilde{s}_B=2,\ f(\mathbf{g}))$,

III. $p(\mathbf{r}\,|\,s_A=0,\ s_B=1,\ f(\mathbf{g}))< p(\mathbf{r}\,|\,\tilde{s}_A=0,\ \tilde{s}_B=0,\ f(\mathbf{g}))$,

IV. $p(\mathbf{r}\,|\,s_A=0,\ s_B=1,\ f(\mathbf{g}))< p(\mathbf{r}\,|\,\tilde{s}_A=2,\ \tilde{s}_B=2,\ f(\mathbf{g}))$,

V. $p(\mathbf{r}\,|\,s_A=0,\ s_B=1,\ f(\mathbf{g}))< p(\mathbf{r}\,|\,\tilde{s}_A=0,\ \tilde{s}_B=2,\ f(\mathbf{g}))$,

$$\text{VI.} \quad p\left(\mathbf{r} \mid s_A = 0, \ s_B = 1, \ f(\mathbf{g})\right) < p\left(\mathbf{r} \mid \tilde{s}_A = 2, \ \tilde{s}_B = 0, \ f(\mathbf{g})\right),$$

Type I error events are those cases which both users transmit the same symbol but the alternative $(\tilde{s}_A, \ \tilde{s}_B)$ differ from $(s_A, \ s_B)$ in one position. Type III events are the opposite of the Type I events. These two types of error events are valid for both the $M=2$ and $M=4$ cases. In the binary case, they cover all the possible error events.

Types II to VI error events are the remaining error event types in the $M=4$ case. Type II events, are again, those cases which both users transmit identical symbols. This time though, the alternative $(\tilde{s}_A, \ \tilde{s}_B)$ differs from $(s_A, \ s_B)$ in both positions. Type IV events corresponds to those cases which the two users transmit different data symbols but the symbols $\tilde{s}_A$ and $\tilde{s}_B$ in the alternative pair are identical but different from both s_A and s_B. Finally, Type V and VI events cover those cases which symbols in both the transmitted and alternative pairs are different (i.e. $s_A \neq s_B$ and $\tilde{s}_A \neq \tilde{s}_B$), but one of $(s_A, \ s_B)$ equals one of $(\tilde{s}_A, \ \tilde{s}_B)$. In the case of Type V, $(\tilde{s}_A, \ \tilde{s}_B)$ and $(s_A, \ s_B)$ differs is one position, while in the case of Type VI, they differ in both positions. Note that with the $M = 4$ mapping in Table II, it is not possible to have an error event where $s_A \neq s_B \neq \tilde{s}_A \neq \tilde{s}_B$. This stems from the fact that if the source symbol pair (I_1, I_2) is mapped into the network-coded symbol c, then the pairs $(I_2, I_1), (I_3, I_4)$ and (I_4, I_3) are also mapped into the same network symbol, where I_1 to I_4 are the four different symbols in the set of $\{0,1,2,3\}$.

Let P_i, $i= I, II... VI$, denote the probabilities of the six types of pairwise error events for any of the three detectors. Then based on the mappings in Tables I and II, we can show that the upper bounds on the SER and the BER are given by the following general expressions

$$P_b \leq P_I + P_{III}, \qquad\qquad M=2, \qquad\qquad (2.24)$$

21

and

$$P_s \le \frac{3}{2}(P_I + P_{II} + P_{III} + P_{IV}) + 3(P_V + P_{VI}) \ , \qquad M=4. \qquad (2.25)$$
$$P_b \le (P_I + P_{II} + P_{III} + P_{IV}) + 2(P_V + P_{VI})$$

It is observed that in the $M=4$ case, the upperbound on the BER is 2/3 that of the SER. Furthermore, (2.25) appears to suggest that the BER upperbound for the $M = 4$ case is higher than that of its binary counterpart. This would be true if both were evaluated using the same symbol SNR γ_s. If however, the calculation is based on the same bit SNR γ_b, the upperbound in the $M = 4$ case can actually be lower than that in the $M = 2$ case, as we shall see.

All the pair-wise error event probabilities $P_I, P_{II}, ..., P_{VI}$ in the above list can be expressed in terms of a quadratic form

$$D = \mathbf{X}^\dagger \mathbf{M} \mathbf{X} \qquad (2.26)$$

being less/greater than a non-negative threshold T_0, where $\mathbf{X}$ is a complex Gaussian vector with a covariance matrix of $\mathbf{\Phi_{XX}} = \frac{1}{2} E\left[\mathbf{XX}^\dagger \right]$, and $\mathbf{M}$ and T_0 vary with the detector and error event types. The probability that $D > T_0$ is given by

$$\Pr[D > T_0] = 1 - \int_{\sigma - j\omega}^{\sigma + j\omega} \frac{\Phi_D(s)}{s} e^{sT_0} ds = 1 - \sum_{s=0 \text{ and all } LHP \text{ poles}} res\left[\frac{\Phi_D(s) e^{sT_0}}{s} \right],$$
$$= -\sum_{LHP \text{ poles}} res\left[\frac{\Phi_D(s) e^{sT_0}}{s} \right] \qquad (T_0 > 0) \qquad (2.27)$$

$$\Pr[D < T_0] = \sum_{s=0 \text{ and all } LHP \text{ poles}} res\left[\frac{\Phi_D(s) e^{sT_0}}{s} \right], \qquad (T_0 > 0) \qquad (2.28)$$

where

22

$$\Phi_D(s) = \prod_{k=1}^{\ell} \left(\frac{-p_k}{s - p_k} \right)^{\eta_k} \qquad (2.29)$$

is the two-sided Laplace transform or characteristic function (CF) of the pdf of the quadratic form D, $p_1, p_2, ..., p_\ell$ its poles, and $\eta_1, \eta_2, ..., \eta_\ell$ the corresponding orders. The integral in the first equality in (2.27) above is simply the cumulative density function of D evaluated at the threshold T_0. As shown in the second equality in the same equation, this integral (or inverse Laplace Transform) can be expressed in terms of the sum of residues of $\Phi_D(s)e^{sT_0}/s$ at $s = 0$ and at all its negative poles, where the residue at a pole p of order η is

$$res(\Phi_D(s)e^{st}/s)_{s=p} = \frac{1}{(n-1)!} \frac{d^{n-1}}{ds^{n-1}} \left\{ (s-p)^n \Phi_D(s)e^{st}/s \right\}. \qquad (2.30)$$

Note that when $T_0 \leq 0$, positive poles will be used to calculate the error event probability instead, i.e.

$$\Pr[D < T_0] = -\sum_{RHP\ poles} res \left[\frac{\Phi_D(s)e^{sT_0}}{s} \right], \qquad (T_0 \leq 0) \qquad (2.31)$$

From [25, Appendix B], the poles of $\Phi_D(s)$ are the roots of the determinant

$$\lambda(s) = \|\mathbf{I} + 2s\mathbf{\Phi_{xx}}\mathbf{M}\|, \qquad (2.32)$$

where $\mathbf{I}$ is an identity matrix and $\|\cdot\|$ denotes determinant. Eqns. (2.26)-(2.32) contain all the required information to calculate the pairwise error events probabilities of the three detectors. The poles, the threshold T_0, and the matrices $\mathbf{\Phi_{xx}}$ and $\mathbf{M}$ are provided in Appendix A for each of the three detectors and each of the six error event types.

23

Using the characteristic function technique, we obtain the PEPs $P_I, P_{II}, ..., P_{VI}$ for each of the three detectors. After substituting these PEPs into (2.23)-(2.24), and with large SNR approximation, we finally obtain the following asymptotic BER upperbounds for the different $M=2$ and $M=4$ detectors:

$$P_{NC,M=2} \approx \left(1 - \left(\frac{2}{\gamma_b}\right)^{1/(\gamma_b)}\right) + \frac{1}{\gamma_b} \qquad \text{(non-coherent, M=2)} \qquad (2.33)$$

$$P_{NC,M=4} \approx 2\left(1 - \left(\frac{1}{\gamma_b}\right)^{1/(2\gamma_b)}\right) + \frac{5}{2\gamma_b} + \frac{1}{2\gamma_b^2} \qquad \text{(non-coherent, M=4)} \qquad (2.34)$$

$$P_{FC,M=2} \rightarrow \frac{1}{\gamma_b} \qquad \text{(full-coherent, M=2)} \qquad (2.35)$$

$$P_{FC,M=4} \rightarrow \frac{1}{\gamma_b} + \frac{2}{3\gamma_b^2} \qquad \text{(full-coherent, M=4)} \qquad (2.36)$$

$$P_{b,PC} \approx \frac{1}{2\gamma_b} + 1 - \left(\frac{1}{\gamma_b}\right)^{1/(2\gamma_b)} \qquad \text{(partial-coherent, M=2)} \qquad (2.37)$$

$$P_{PC,M=4} \rightarrow \frac{11}{6\gamma_b} + \left(1 - \left(\frac{1}{2\gamma_b}\right)^{1/(4\gamma_b)}\right) + \left(1 - \frac{3}{2}\left(\frac{1}{2\gamma_b}\right)^{1/(6\gamma_b)} + \frac{1}{2}\left(\frac{1}{2\gamma_b}\right)^{1/(2\gamma_b)}\right)$$

$$\text{(partial-coherent, M=4)} \qquad (2.38)$$

2.4. Analytical and simulation Results

Fig. 2.3 shows the upperbound on the BER of the $M=2$ non-coherent detector (2.33) and the $M=2$ full-coherent detector (2.35). As expected, the full-coherent detector has better performance than the non-coherent detector, because the CSI is perfectly known in

the former. In Fig. 2.4, we further analyze the characteristics of the two detectors by providing conditional BER curves when $c = 0$ ($\mathbf{s}_A = \mathbf{s}_B$) and when $c = 1$ ($\mathbf{s}_A \neq \mathbf{s}_B$). The conditional BERs are given in (2.39)-(2.42) below; the detail calculation can be referred to Appendix A.

$$P_{c=0,FC} = 2P\left((s_A = 0, s_B = 0) \to (\tilde{s}_A = 0, \tilde{s}_B = 1)\right)$$

$$= 2\left(1 - \frac{1 + \sqrt{1 + 2\gamma^{-1}}}{2\sqrt{1 + 2\gamma^{-1}}}\right) \approx \frac{1}{\gamma_s} \ , \quad \gamma_s \to \infty \ , \qquad \text{(c=0, full-coherent)} \quad (2.39)$$

$$P_{c=1,FC} = 2P\left((s_A = 1, s_B = 0) \to (\tilde{s}_A = 0, \tilde{s}_B = 0)\right)$$

$$= \frac{\sqrt{1 + 2\gamma^{-1}} - 1}{2\sqrt{1 + 2\gamma^{-1}}} \approx \frac{1}{\gamma_s} \ , \quad \gamma_s \to \infty \ , \qquad \text{(c=1, full-coherent)} \quad (2.40)$$

$$P_{c=0,NC} = 2P\left((s_A = 0, s_B = 0) \to (\tilde{s}_A = 0, \tilde{s}_B = 1)\right)$$

$$= 2 - \frac{(2\gamma_s + 1)^{(1+\gamma_s^{-1})}}{(\gamma_s + 1)^{(1+2\gamma_s^{-1})}} \approx 2 - 2\times\left(\frac{2}{\gamma_s}\right)^{1/(\gamma_s)} \ , \quad \gamma_s \to \infty \ , \qquad \text{(c=0, non-coherent)} \quad (2.41)$$

$$P_{c=1,NC} = 2P\left((s_A = 0, s_B = 1) \to (\tilde{s}_A = 0, \tilde{s}_B = 0)\right)$$

$$= \frac{(2\gamma_s + 1)^{(1+\gamma_s^{-1})}}{(\gamma_s + 1)^{2(1+\gamma_s^{-1})}} \approx \frac{2}{\gamma_s}, \quad \gamma_s \to \infty \ , \qquad \text{(c=1, non-coherent)} \quad (2.42)$$

According to Fig. 2.4, the BER of the coherent detector in (2.12) conditioned on a sum bit of $c = 0$ is the same as that when conditioned on $c = 1$. However, the same is not true of the non-coherent detector in (2.9). The conditional BER when $c = 1$ is several times higher than that when $c = 0$. This is due to the difference in (2.41) and (2.42).

Fig. 2.5 shows the simulation results of the $M = 2$ non-coherent detector and the $M = 2$ full-coherent detector, along with the bounds. The simulated BER of the non-coherent receiver and the coherent receiver are only 0.5 dB away from their corresponding upper bounds. As such, we conclude that the upperbounds are tight. It is

obvious from the figure that there is a big performance gap between the coherent and the non-coherent detectors. For example, the coherent detector requires only 30 dB of SNR to attain a BER of 10^{-3}. The non-coherent detector, on the other hand, requires 40 dB.

We study next the BER performance of the proposed partial-coherent detector and see if it can indeed narrow the gap between the non-coherent and the full-coherent detector. Fig. 2.6 provides the bounds of the three detectors and the simulation results of the proposed $M = 2$ partial-coherent detector. According to the graph, the simulation results agree with the bound, though there is a 1 dB difference between the two. The important thing is, these results indicate that the partial-coherent detector can provide a very significant improvement over the non-coherent detector at practically no extra cost. For example, at a BER of 10^{-3}, the proposed partial-coherent detector promises a 3 dB improvement in BSNR over the non-coherent detector without resorting to transmit any pilot symbols. Another interesting property of the partial-coherent detector is that, as shown in Fig. 2.7, its BER upper bounds conditioned on $c = 0$ and $c = 1$ coincide with BER upper bound of the coherent detector for $c = 0$ and the upper bound of the non-coherent detector for $c = 1$. In other words, the BER of the partial-coherent detector is the average of the BERs of the coherent and the non-coherent detector.

Fig. 2.8 shows that the BERs of the three types of $M = 4$ detectors for 2P-TWR. It is observed that they have similar performance to their corresponding $M = 2$ counterparts. Finally, Fig. 2.9 provides the simulation results of the proposed $M = 4$ partial-coherent detector, along with the bounds of the three $M = 4$ detectors. It is observed that the bound for the partial-coherent detector is not very tight, as there is a 2dB gap between the simulation BER curve and the bound. Similar to the $M = 2$ case, the proposed $M = 4$ partial-coherent bound provides a 3 dB improvement in BSNR over the non-coherent detector. However, there is still a 7 dB gap between the partial-coherent detector and the full-coherent detector.

Finally, we comment on the performance of the proposed partial-coherent detector against the detector from [21, Eqn. (23)]. According to [22], if the fading amplitudes

α_1 and α_2 stay constant within a block of data and known perfectly to the receiver, then the performance of their detector is given by the blue curve labeled "DNC, known α_1, α_2" in Fig. 3 of [22], which is almost identical to that of the proposed partial-coherent detector. However in actual implementation, the proposed partial-coherent detector has a lower complexity because it is much simpler to estimate the sum fading gain $u = g_A + g_B$ (refer to the next chapter) than to estimate α_1 and α_2 according to [21, Eqn. (35)-(39)]. Note also that the estimator in [22] is only valid for block fading while the one proposed in this thesis is applicable to time-selective fading.
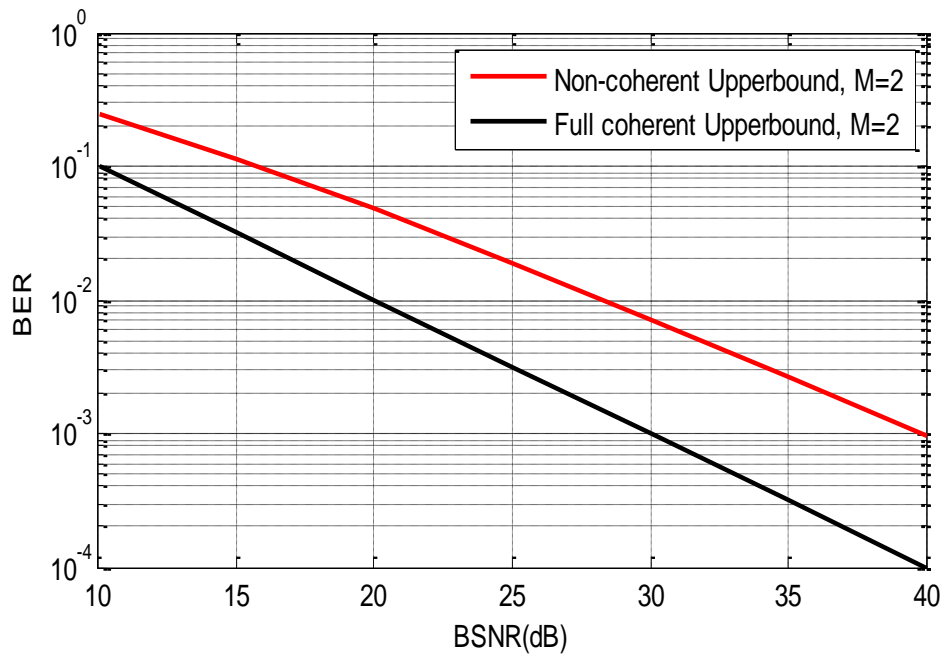
Fig. 2.3: Upperbound on the BER for $M = 2$ non-coherent and full-coherent detectors at the relay
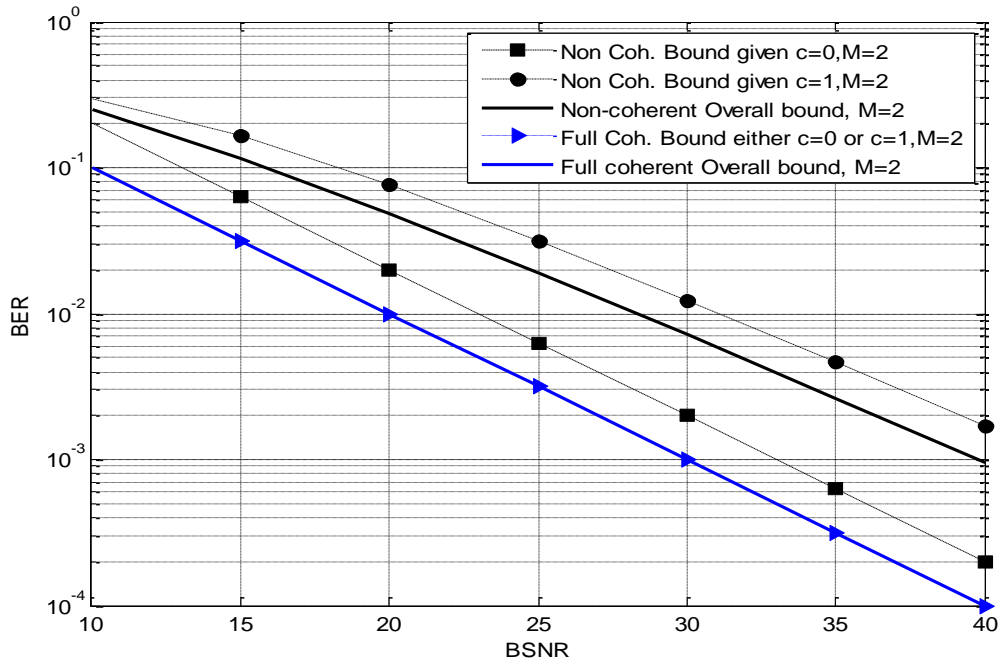
Fig. 2.4: BER of the relay's non-coherent and coherent detectors for different error events.
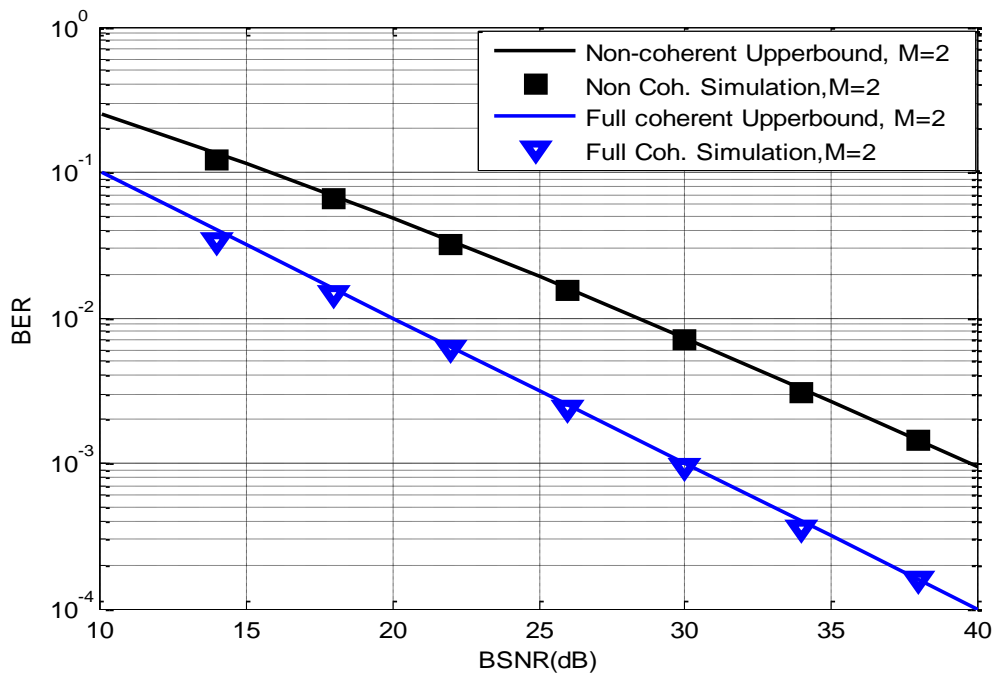
Fig. 2.5: Simulated BER along with bounds of the relay's non-coherent and full-coherent detectors in the $M = 2$ case.
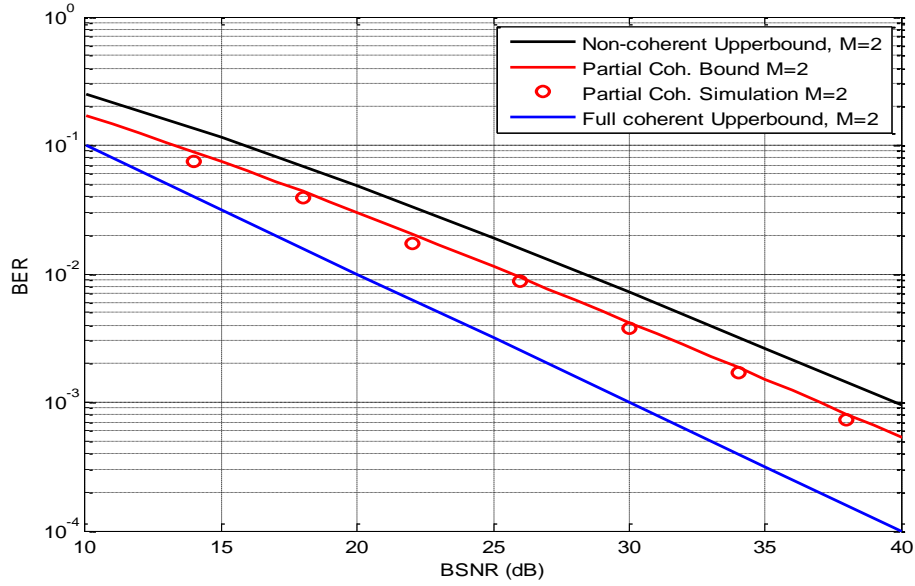
Fig. 2.6: Simulated BER vs. analytical bounds for $M = 2$ partial-coherent detector at the relay.
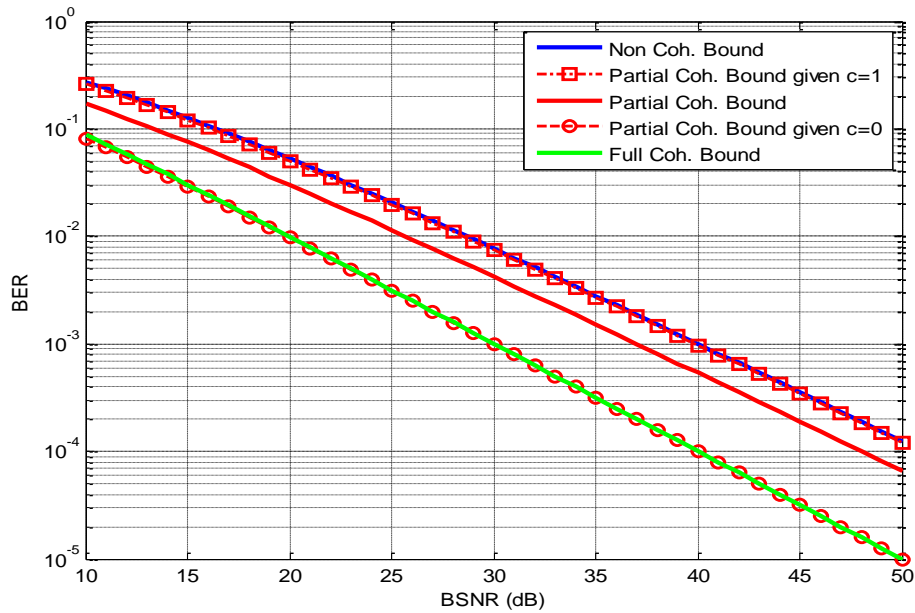
Fig 2.7: Analytical results of the $M = 2$ proposed partial-coherent detector in different error events.
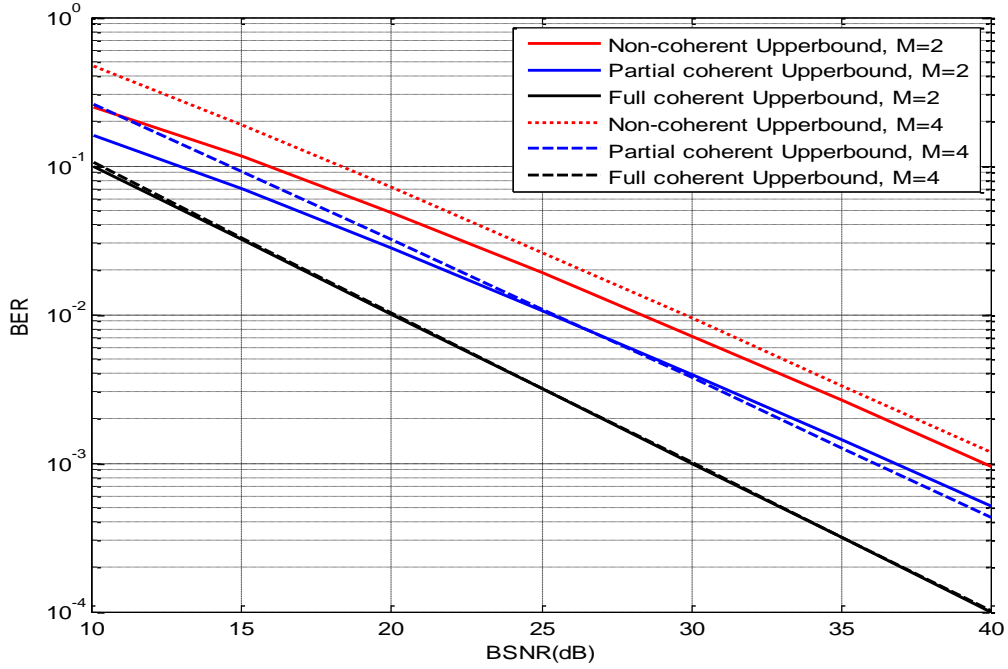
Fig. 2.8: Analytical Bounds on BER for different $M = 2$ and $M = 4$ detectors at the relay.
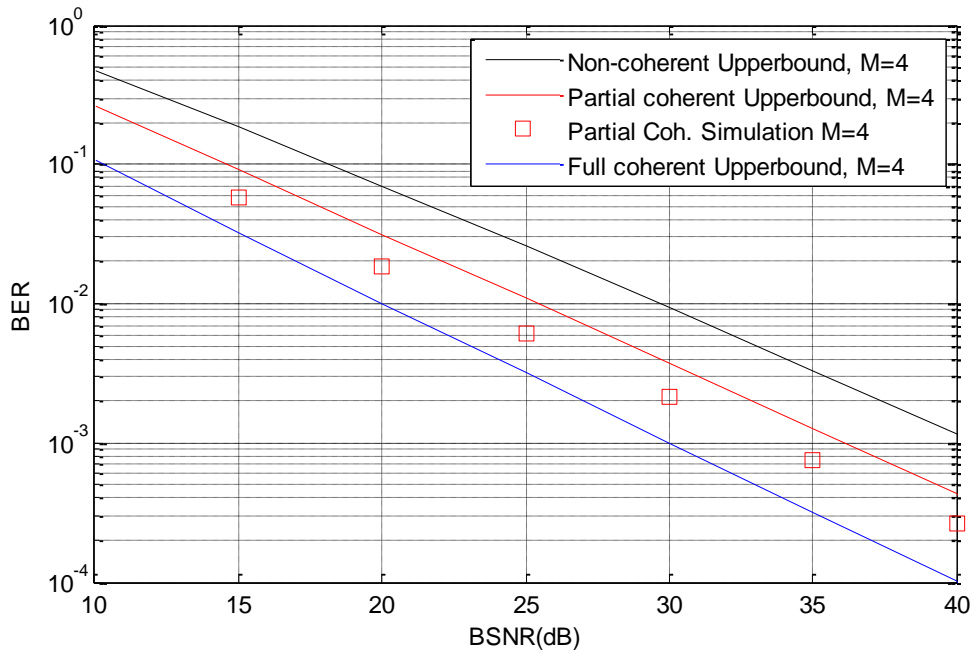
Fig. 2.9: Simulated BER vs. analytical bounds for the $M = 4$ partial-coherent detectors at the relay.

2.5. Conclusion

In this chapter, the topics of non-coherent and full-coherent detection of orthogonal modulations transmitted over a two-phase two-ray relay (2P-TWR) channel were revisited. As is well known, the non-coherent detector, while simple, does not provide very good BER performance. The full-coherent detector, on the other hand, provides very good performance, but it requires either the transmission of pilots or bandwidth expansion, in general, for channel estimation. Our results indicate that there is a 10 dB gap between the two detectors for the 2P-TWR channel, which is much wider than in the case of point-to-point transmission. As a compromise, a pilot-less partial-coherent detector is proposed to bridge the gap of non-coherent and full-coherent detection, without much added complexity. The partial-coherent detector is able to provide a 3 dB improvement in BSNR over the non-coherent detector without resorting to transmit any pilot symbols. However it still suffers a huge BSNR penalty of 7 dB when compared to the full-coherent detector. In the next Chapter, we propose a decision feedback strategy that enables the relay receiver to close this huge performance gap.

Chapter 3.

A Random Channel Sounding Decision Feedback Receiver

In this chapter, a decision feedback (DFB) receiver built upon the partial-coherent detector in Chapter 2 is proposed to improve the error performance of 2P-TWR communication systems that employ PNC and orthogonal modulations. Section 3.1 outlines the structure of this decision feedback receiver, and provides details of the estimator for the sum fading gain that is used in the initial partial-coherent detector to kick start the decision feedback mechanism. The next two sections deals with the topics of identification and estimation of the individual uplink fading gains based on the decisions provided by the partial-coherent detector. Section 3.2 is concerned with static fading while Section 3.3 deals with the more challenging scenario of time-selective fading. Simulation results are presented, with the data block size, the interpolator type (minimum-mean-square versus least square), and the fade rate as parameters. Comparison with full-coherent detection will be made. Finally concluding remarks on the performance of the proposed DFB receiver are provided in Section 3.4.

3.1. A Decision Feedback Receiver built on Partial-coherent Detection

Consider the correlator output in (2.2). If the transmitted symbols from the two users are different, i.e. $s_A[k] = I$ and $s_B[k] = J$, where $I \neq J$, then

$$r_j[k] = \begin{cases} g_A[k] + n_I[k], & j = I, \\ g_B[k] + n_J[k], & j = J, \\ n_j[k], & j \neq I, j \neq J. \end{cases} \qquad (3.1)$$

This suggests that if the relay can identify those intervals which the two users transmit different data symbols, then it can separate the two fading gains from the composite receive signal in those intervals and perform channel estimation for the entire block of data through interpolation. In other words, we can devise a decision feedback receiver that exploits the randomness in the transmitted data to perform channel sounding even though there are no pilot symbols. Once the fading gains in the entire block of data are estimated, then the data symbols can be re-detected using the coherent detector in (2.12), with the actual fading gains replaced by the estimated gains. The procedure of a completed decision feedback loop is summarized as follows:

- Step 1: use the proposed partial-coherent detector in (2.21) to make preliminary decisions on a block of N consecutive network-coded symbols $\{c[1], c[2],\dots c[N]\}$, $N > 2$;

- Step 2: identify the decisions from Step 1 that correspond to $s_A[k] \neq s_B[k]$; sort out which correlator output $r_j[k]$ is associated with $g_A[k]$, and which $r_j[k]$ is associated with $g_B[k]$; estimate the individual fading gains in the entire block of N consecutive symbols via interpolation.

- Step 3: Use the estimated CSI obtained in step 2 instead of the true fading gains $g_A[k]$ and $g_B[k]$ to perform coherent detection in (2.12).

- If it is needed, multiple rounds of decision feedback can be employed by repeating Step 2 and Step 3.

Since the individual fading gains required for coherent detection in the feedback stage are obtained through interpolation of the fading gains extracted from those intervals where the data symbols from the two users are detected to be different by the partial-coherent detector, there should be sufficient number of such intervals. Otherwise, results

33

of the interpolation would not be accurate. As such, in the proposed decision feedback receiver, we set a threshold K_T such that when the number of the preliminary decisions corresponding to $s_A[k] \neq s_B[k]$ is less than K_T, no decision feedback will be performed and the receiver simply accepts the decisions of the partial-coherent detector as the final decisions. In this investigation, K_T is set to a relatively small number, in the neighbourhood of 4. For a sufficiently large block size N, the probability that the number of intervals where $s_A[k] \neq s_B[k]$ falls below K_T will be small. Thus most of the time, DFB will be carried out.

It is also possible to use the non-coherent detector in (2.9), in place of the partial-coherent detector, to provide the preliminary decisions in Step 1. However, starting with the partial-coherent detector in (2.21) ensures faster convergence because of its superior performance.

The flow chart in Fig. 3.1 summarizes the above decision feedback procedure. Details of those blocks used during decision feedback are provided in Sections 3.2 and 3.3. The remainder of this section addresses the issue of estimating the sum fading gain required for initial partial-coherent detection.
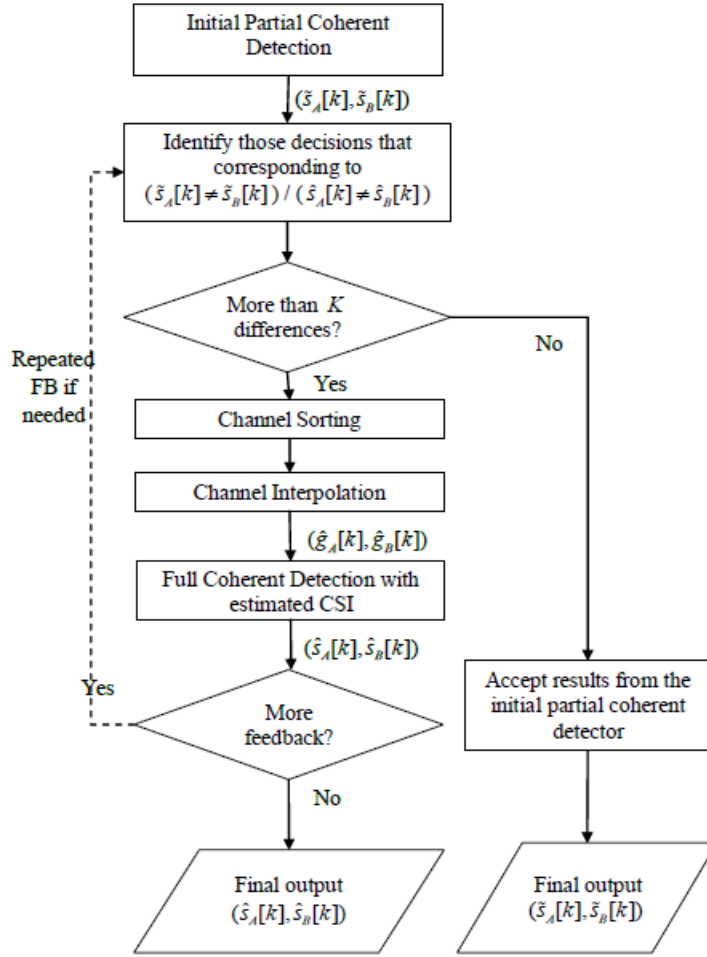
Fig. 3.1: Flow chart for the proposed DFB receiver.

3.1.1. Sum Gain Estimation - Static Fading

In order to perform the initial partial-coherent detection in Fig. 3.1, the relay has to estimate the sum fading gains

$$u[k] = g_A[k] + g_B[k], \qquad k = 1, 2, ..., N \qquad (3.2)$$

and use the estimates, $\hat{u}[k]$, $k = 1, 2, ..., N$, in place of $u[k]$ in (2.4) during partial-coherent detection. These estimates can be obtained by using a MMSE estimator operating on the sum output of the correlators (2.3)

$$\tilde{u}[k] = \sum_{i=0}^{M-1} r_i[k] = u[k] + e[k], \qquad k = 1, 2, ..., N \qquad (3.3)$$

where $e[k]$ is $CN(0, MN_0)$. Define

$$\mathbf{u} = \left[u[1], u[2], ..., u[N] \right]^T, \qquad (3.4a)$$

$$\tilde{\mathbf{u}} = \left[\tilde{u}[1], \tilde{u}[2], ..., \tilde{u}[N] \right]^T, \qquad (3.4b)$$

$$\mathbf{e} = \left[e[1], e[2], ..., e[N] \right]^T. \qquad (3.4c)$$

The MMSE estimate of the sum fading gain in the kth interval, $u[k]$, is

$$\hat{u}[k] = \boldsymbol{\varphi}_{u[k]\tilde{\mathbf{u}}} \boldsymbol{\Phi}_{\tilde{\mathbf{u}}\tilde{\mathbf{u}}}^{-1} \tilde{\mathbf{u}}, \qquad (3.5)$$

where $\boldsymbol{\varphi}_{u[k]\tilde{\mathbf{u}}} = \frac{1}{2} E\left[u[k]\tilde{\mathbf{u}}^\dagger \right]$ is the correlation between $u[k]$ and $\tilde{\mathbf{u}}$, and $\boldsymbol{\Phi}_{\tilde{\mathbf{u}}\tilde{\mathbf{u}}} = \frac{1}{2} E\left(\tilde{\mathbf{u}}\tilde{\mathbf{u}}^\dagger \right)$ is the covariance matrix of $\tilde{\mathbf{u}}$. Since the terms $u[k]$ and $e[k]$ in (3.3) are independent,

$$\boldsymbol{\Phi}_{\tilde{\mathbf{u}}\tilde{\mathbf{u}}} = \frac{1}{2} E\left(\tilde{\mathbf{u}}\tilde{\mathbf{u}}^\dagger \right) = \boldsymbol{\Phi}_{\mathbf{u}\mathbf{u}} + \boldsymbol{\Phi}_{\mathbf{e}\mathbf{e}} = \boldsymbol{\Phi}_{\mathbf{u}\mathbf{u}} + MN_0 \mathbf{I}_N, \qquad (3.6)$$

and

$$\boldsymbol{\varphi}_{u[k]\tilde{\mathbf{u}}} = \frac{1}{2} E\left[u[k]\tilde{\mathbf{u}}^\dagger \right] = \frac{1}{2} E\left[u[k]\mathbf{u}^\dagger \right] = \boldsymbol{\varphi}_k; \qquad (3.7)$$

where $\boldsymbol{\Phi}_{\mathbf{u}\mathbf{u}} = \frac{1}{2} E\left(\mathbf{u}\mathbf{u}^\dagger \right)$ is the covariance matrix of $\mathbf{u}$, $\boldsymbol{\Phi}_{\mathbf{e}\mathbf{e}} = MN_0 \mathbf{I}_N$ is the covariance matrix of $\mathbf{e}$, and $\boldsymbol{\varphi}_k$ is just the kth row of $\boldsymbol{\Phi}_{\mathbf{u}\mathbf{u}}$. Assuming a Jake's fading model, then the $(n,m)^{\text{th}}$ element of $\boldsymbol{\Phi}_{\mathbf{u}\mathbf{u}}$ is

$$\phi_{uu}(n,m) = 2\sigma_g^2 J_0(2\pi(n-m)f_d T), \qquad (3.8)$$

where f_d is the Doppler frequency and T is the symbol interval. Substituting (3.6) and (3.7) into (3.5), the channel estimate becomes

$$\hat{u}[k] = \boldsymbol{\varphi}_k (\boldsymbol{\Phi}_{\mathbf{uu}} + MN_0 \mathbf{I}_M)^{-1} \tilde{\mathbf{u}} . \tag{3.9}$$

and the corresponding MSE is

$$\varepsilon_0^2[k] = \tfrac{1}{2} E\left[|u[k] - \tilde{u}[k]|^2 \right] = 2\sigma_g^2 - \boldsymbol{\varphi}_k (\boldsymbol{\Phi}_{\mathbf{uu}} + MN_0 \mathbf{I}_M)^{-1} \boldsymbol{\varphi}_k^\dagger . \tag{3.10}$$

The average normalized MSE (NMSE) across a block of N symbols is simply

$$\begin{aligned}
\varepsilon_N^2 &= \frac{1}{2\sigma_g^2} \times \frac{1}{N} \sum_{k=1}^{N} \varepsilon_0^2[k] = 1 - \frac{1}{2\sigma_g^2 N} \sum_{k=1}^{N} \boldsymbol{\varphi}_k (\boldsymbol{\Phi}_{\mathbf{uu}} + MN_0 \mathbf{I}_M)^{-1} \boldsymbol{\varphi}_k^\dagger \\
&= 1 - \frac{1}{2\sigma_g^2 N} \operatorname{trace}\left\{ \boldsymbol{\Phi}_{\mathbf{uu}} (\boldsymbol{\Phi}_{\mathbf{uu}} + MN_0 \mathbf{I}_M)^{-1} \boldsymbol{\Phi}_{\mathbf{uu}}^\dagger \right\}
\end{aligned} \tag{3.11}$$

In the special case of static fading, i.e. $f_d = 0$, then $\boldsymbol{\Phi}_{\mathbf{uu}} = 2\sigma_g^2 \mathbf{U}_N$ and $\boldsymbol{\varphi}_k = 2\sigma_g^2 \mathbf{1}_N$, where $\mathbf{1}_N$ and $\mathbf{U}_N$ are all-one vector and matrix of size N respectively. In this case,

$$(\boldsymbol{\Phi}_{\mathbf{uu}} + MN_0 \mathbf{I}_N)^{-1} = \frac{1}{MN_0} \left(\mathbf{I}_N - \frac{2\sigma_g^2}{2\sigma_g^2 N + MN_0} \mathbf{U}_N \right) \quad \text{(static fading)} \tag{3.12}$$

As a result, the estimate $\hat{u}[k]$ in (3.9) becomes

$$\begin{aligned}
\hat{u}[k] &= \frac{2\sigma_g^2}{MN_0} \mathbf{1}_N \left(\mathbf{I}_N - \frac{2\sigma_g^2}{2\sigma_g^2 N + MN_0} \mathbf{U}_N \right) \tilde{\mathbf{u}} = \frac{2\sigma_g^2}{2\sigma_g^2 N + MN_0} \sum_{k=0}^{N-1} \tilde{u}[k] \\
&\approx \frac{1}{N} \sum_{k=0}^{N-1} \tilde{u}[k] \quad \text{at large SNR}
\end{aligned} \tag{3.13}$$

which, as expected, is approximately the time average of the sum correlator output. The corresponding NMSE across a frame is

$$\varepsilon_N^2 = \frac{MN_0}{2\sigma_g^2 N + MN_0} \to \frac{MN_0}{2\sigma_g^2 N} \text{ at large SNR .} \qquad (3.14)$$

As observed from (3.14), the NMSE is inversely proportional to the block size N and the symbol SNR $\gamma_s = \sigma_g^2 / N_0$ when $f_d = 0$.

On the implementation complexity of the decision feedback channel estimator, since the estimation filter $\boldsymbol{\varphi}_k (\boldsymbol{\Phi}_{\mathbf{uu}} + MN_0 \mathbf{I}_M)^{-1}$ in (3.9) needed only to be updated once over many blocks, the computational complexity in estimating the sum fading gain is simply the number of multiply-and-adds (MAD) required. This translates into N MADs per symbol, or N^2 per block of N symbols.

Figs. 3.2 and 3.3 show the NMSE, ε_N^2, for the $M = 2$ partial-coherent detector at fade rates of $f_d T = 0$ and $f_d T = 0.005$, respectively. Both analytical results (3.10) and simulated results are presented for different block sizes N. According to the figures, the analytical and simulation results for the MMSE estimator show excellent agreement in both static fading and time-selective fading environment. Also observed from the figures is that the NMSE is inversely proportional to the SNR, i.e. each NMSE curve decreases at a rate of 1 decade per 10 dB increase in SNR and there is no irreducible error floor. As expected, a larger block size N leads to a lower NMSE. It can thus be concluded that the MMSE estimator indeed provides accurate estimation of the sum fading gain in both static fading and time-selective fading environments. As expected, time-selective fading leads to a larger NMSE than static fading.

Once $\hat{\mathbf{u}} = \left[\hat{u}[1], \hat{u}[2], ..., \hat{u}[N]\right]^T$ is obtained, the relay receiver can then use the estimated sum fading $\hat{u}[k]$ in place of the actual one, u, in (2.21) to perform initial partial-coherent detection. In the following sections, we switch our focus to the estimation of the uplink channels through the decisions fed back by the initial partial-coherent detector. We consider two scenarios: static and time-selective fading and they are treated separately in Sections 3.2 and 3.3 respectively.
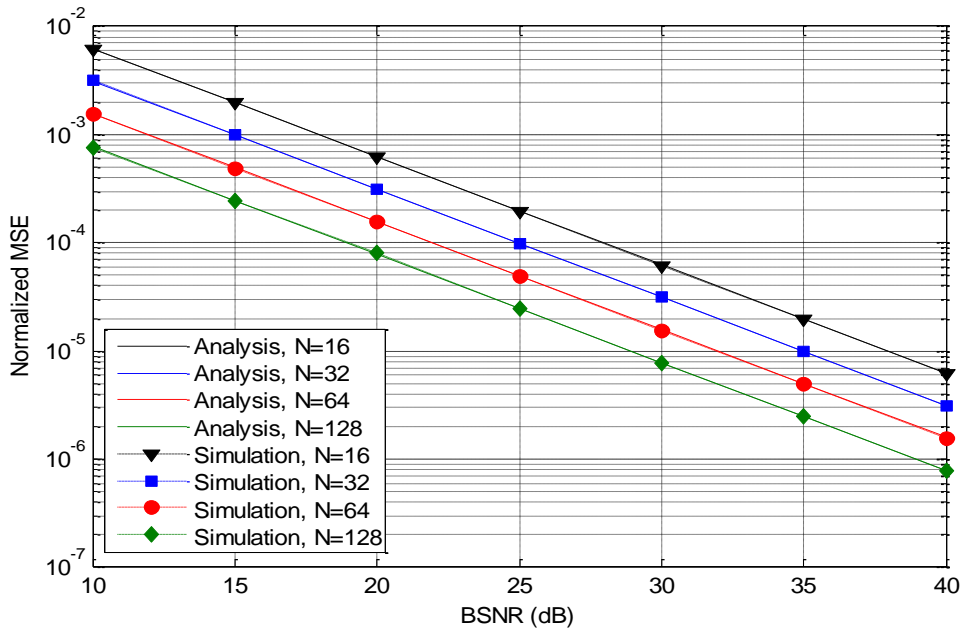
Fig. 3.2: Analytical and simulated NMSE for estimating the sum fading gain with different block sizes in a $M = 2$ system; Doppler frequency: $f_d T = 0$.
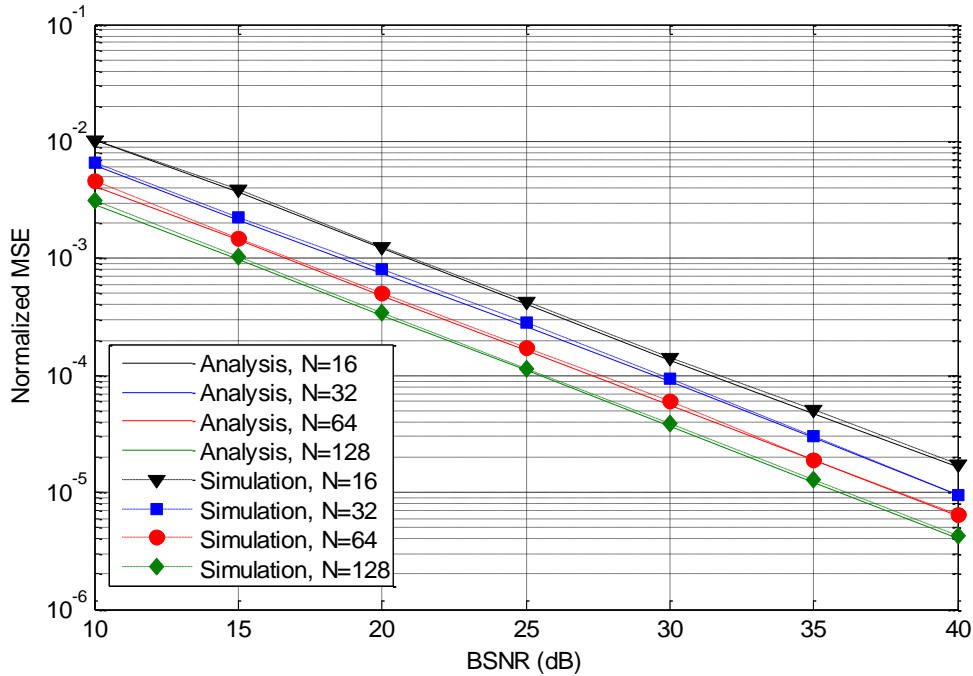
Fig. 3.3: Analytical and simulated NMSE for estimating the sum fading gain with different block sizes in a $M = 2$ system; Doppler frequency: $f_d T = 0.005$.

3.2. Decision Feedback Uplink Channel Estimation - Static Fading

3.2.1. Gain Sorting and MMSE Channel Estimation

Once initial partial-coherent detection is completed, the preliminary decisions are divided into two groups. One group is for same detected data symbol pairs from the two users ($\tilde{s}_A = \tilde{s}_B$) and the other is for different detected symbol pairs ($\tilde{s}_A \neq \tilde{s}_B$). The decision feedback receiver is only interested in the second group as only these preliminary decisions can provide information about the individual fading gains in the uplinks. Let $k_0, k_1, ..., k_{L-1}$ be the intervals where $\tilde{s}_A \neq \tilde{s}_B$. If these decisions are corrected, then the correlator outputs in these intervals follow (3.1). In other words, two of the M correlator outputs in each of these intervals contain signals, while the others contain only noise. Because of the randomness in the uplink data, the two correlators which contain signals varies with k_ℓ, $\ell = 0, 1, ..., L-1$. This means the first step towards uplink channel estimation is to sort out which correlator output contains $g_A[k_\ell]$ and which contains $g_B[k_\ell]$. For a static fading channel, we propose the following sorting procedure.

For every symbol interval k_ℓ where $\tilde{s}_A[k_\ell] \neq \tilde{s}_B[k_\ell]$, the correlators in (3.1) are sorted according to their magnitudes into the vector

$$\left| r_{i_0}[k_\ell] \right| > \left| r_{i_1}[k_\ell] \right| > ... > \left| r_{i_{M-1}}[k_\ell] \right| , \tag{3.15}$$

where it is understood that $i_0 \neq i_1 \neq ... \neq i_{M-1}$. For a static fading channel, each uplink gain can be treated as a constant over the duration of a block of N symbols. With a reasonably large SNR, the two largest correlator outputs in each of the intervals $k_0, k_1, ..., k_{L-1}$ must correspond to the fading processes, and the probability of a change of associations of the

40

pair of the two largest correlator outputs with the two uplink gains at time k_ℓ and that at time $k_{\ell+1}$ is very small. The fading estimates are thus set to be

$$\tilde{g}_A[k_\ell] = r_{i_0}[k_\ell]$$
$$\tilde{g}_B[k_\ell] = r_{i_1}[k_\ell] \qquad \text{(static fading)}, \qquad (3.16)$$

and the final MMSE estimates are given by

$$\hat{g}_i = \frac{1}{L + \gamma_s^{-1}} \sum_{\ell=1}^{L} \tilde{g}_i[k_\ell], \quad i = A, B \ . \qquad (3.17)$$

where γ_s is the average symbol SNR within the duration of a block of N symbols. The time index k_ℓ is ignored in the final estimate $\hat{g}_i$ because of the assumption of static fading in this subsection.

The above sorting rule introduces an ambiguity, i.e. g_A is confused with g_B and vice versa. The ambiguity has no effort on the performance of the final coherent detector with PNC though. This can be explained from the network coding rules in Table 2.1 and 2.2 which show that the pair (*I, J*) and (*J, I*), $I \neq J$, are always coded into the same network symbol. Once the uplink channels are estimated, the full-coherent detector in (2.12), with g_A and g_B replaced by their estimates in (3.17), can be used to make the final decision $\hat{c}[k]$ in (2.8).

3.2.2. Numerical Results

The BER performance of the proposed DFB receiver in a static fading environment is evaluated via simulation. We first show in Fig. 3.4 and Fig. 3.5 how the processing block size *N* affects the BER performance of the proposed DFB detector for binary ($M = 2$) and quaternary ($M = 4$) modulations, respectively. Results for $N = 16$, 32, 64, 128 are

41

shown. Simulated BER curves of the initial partial-coherent detector (with estimated sum fading gain), as well as the partial-coherent and the full-coherent BER bounds (with perfect CSI), are also included in these figures. As predicted, in a static fading channel, the performance of the initial partial-coherent detector and the DBF receiver improves with the block size, though with diminishing returns.

In the $M = 2$ case, simulation results of the $N = 16$ and $N = 32$ partial-coherent detectors agree with the partial-coherent bound. In using a block size of $N = 64$ or longer the partial-coherent detector can provide a 5 dB improvement in SNR over the partial-coherent detector at a BER of 10^{-3}. This is only 2 dB away from the coherent bound.

In the $M = 4$ case, It is observed that the bounds of the partial-coherent detector and the full-coherent detector are not very tight, as there exist noticeable gaps between the bounds and the simulation results. The simulation results indicate that the proposed DFB receiver can actually attain the performance of the coherent receiver. Although not shown in Fig 3.5, the simulated BER curve of the $N = 128$ DFB receiver is almost indistinguishable from that of the $N = 64$ detector.

Fig. 3.6 and Fig. 3.7 illustrate the effect of adding another round of feedback to the proposed DFB receiver in the $M = 2$ and $M = 4$ systems. A processing block size of $N = 32$ is chosen in these figures to ensure there are sufficient samples for estimating the uplink gains. According to Fig. 3.6, the $M = 2$ partial-coherent detector (using estimated sum fading gain, not the bound) requires 37 dB to attain a BER of 10^{-3}. The SNR requirement is cut to 32.5 dB with one round of feedback (red curve) and further reduces to 31.5 dB with an extra round of feedback (blue curve). Similarly in the $M=4$ case, it is observed that the proposed DFB detector, with one round of feedback, already provides an impressive 5 dB improvement in SNR over the partial-coherent detector at a BER at 10^{-3}. The gap between the full-coherent detection and the proposed decision feedback receiver is now reduced to only 2dB. Another 1dB gain in SNR can be achieved through a second round of feedback.
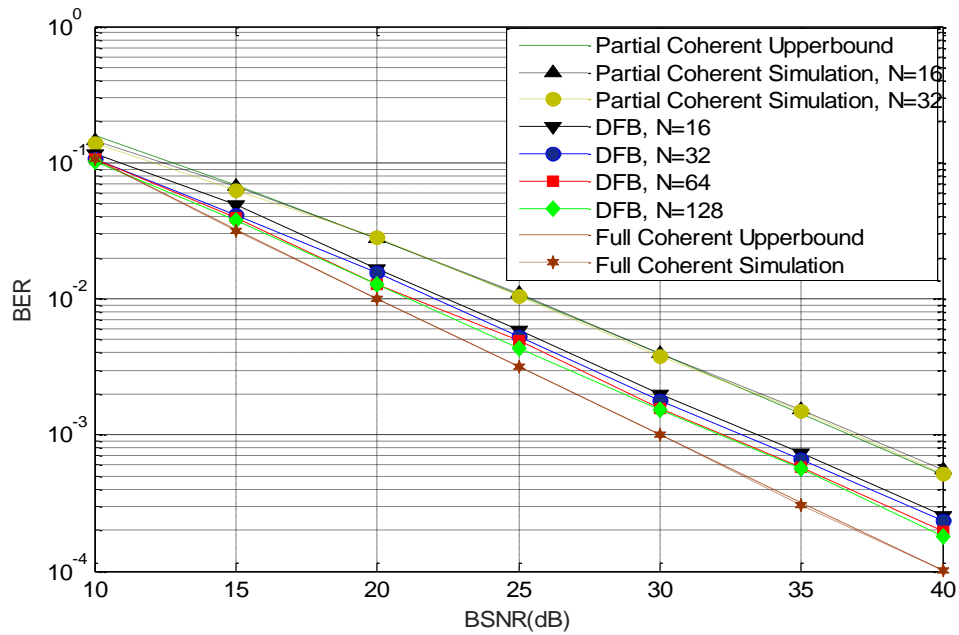
Fig. 3.4: Simulated BER of the $M = 2$ proposed DFB receiver at $f_d T = 0$ with varying processing block size.
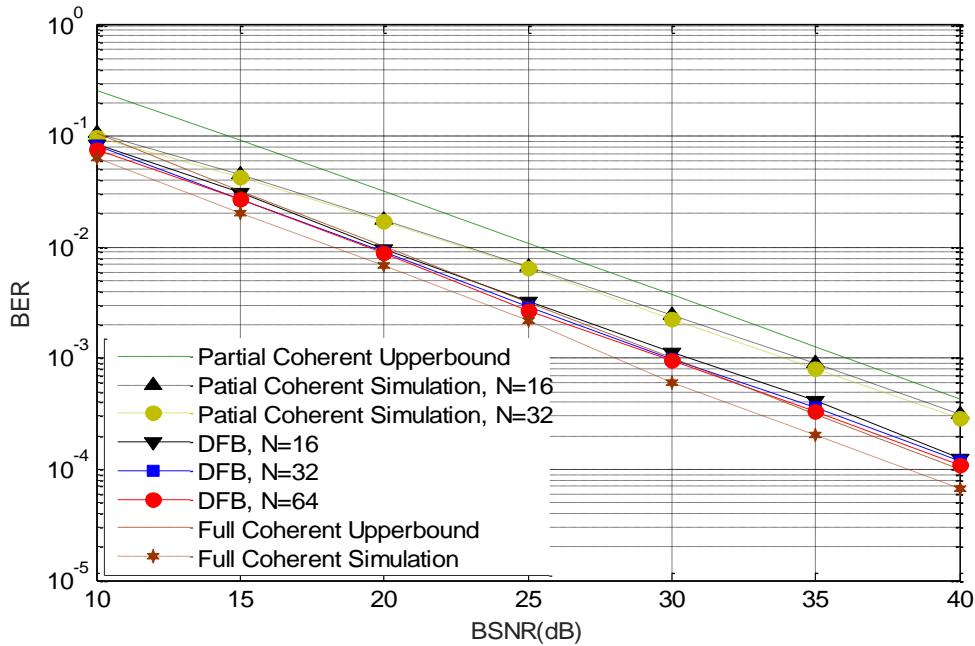
Fig. 3.5: Simulated BER of the $M = 4$ proposed DFB receiver at $f_d T = 0$ with varying processing block size.
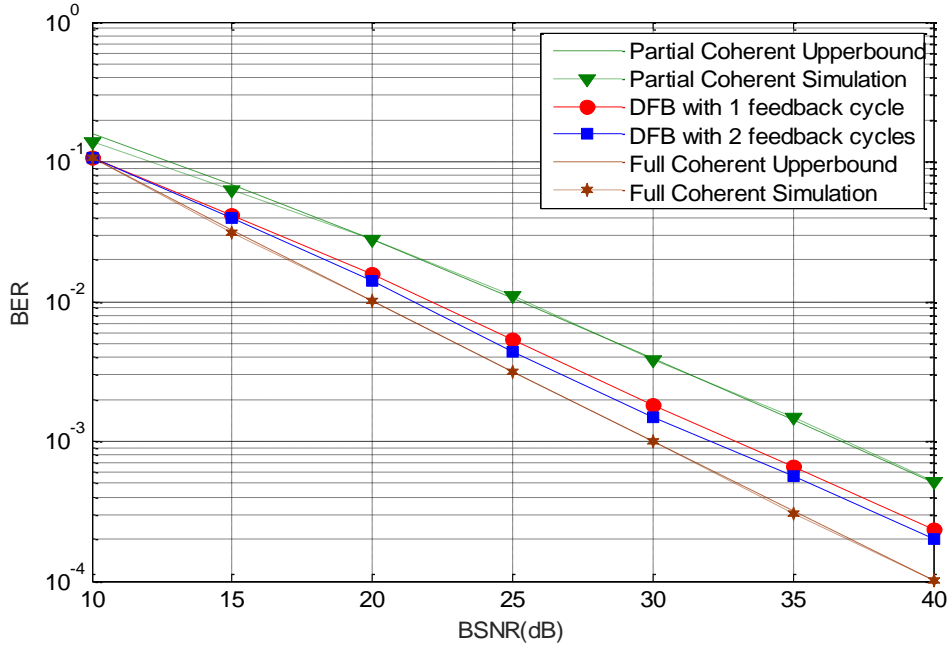
Fig. 3.6: Simulated BER of the proposed $M=2$ DFB receiver at $f_d T=0$. The processing block size is N=32.
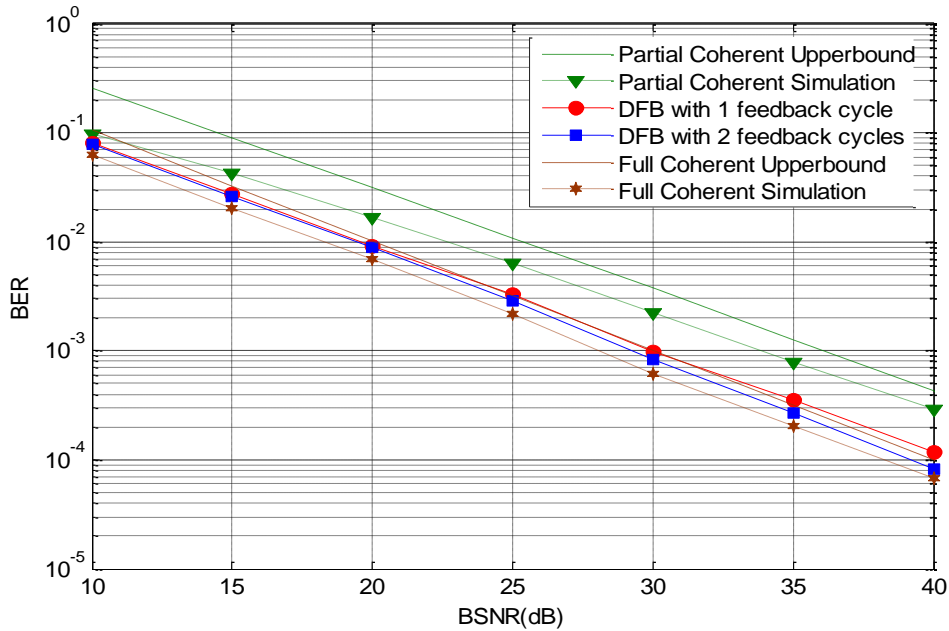
Fig. 3.7: Simulated BER of the proposed $M=4$ DFB receiver at $f_d T=0$. The processing block size is N=32.

3.3. Decision   Feedback   Uplink   Channel Estimation - Time Selective Fading

The decision-feedback based channel sorting and estimation strategies in (3.16) and (3.17) have the attribute of being simple. However, they are restricted to a static fading channel. In this section, more sophisticated techniques are introduced to handle time selective fading. As in the last section, the outputs of the correlators with the largest and the second largest magnitudes are denoted as $r_{i_0}[k_\ell]$ and $r_{i_1}[k_\ell]$, where $k_0 < k_1 < ... < k_{L-1}$ are the intervals where the uplink symbols from the users are detected to be different by the initial partial-coherent detector.

3.3.1.   Gain Sorting Algorithm

For time-selective fading channels, it is possible that the fading pattern $g_A[k]$ and $g_B[k]$ cross each other in the complex plane within a window of N consequent symbols. When this occurs, there should be a change of association of $\left(r_{i_0}[k_\ell], r_{i_1}[k_\ell]\right)$ with $\left(g_A[k_\ell], g_B[k_\ell]\right)$ and $\left(r_{i_0}[k_{\ell+1}], r_{i_1}[k_{\ell+1}]\right)$ with $\left(g_A[k_{\ell+1}], g_B[k_{\ell+1}]\right)$. To track the associations, a differential approach is proposed as follows.

First, the event of no change in associations is modeled by declaring $r_{i_0}[k_\ell]$ and $r_{i_0}[k_{\ell+1}]$ belong to one of the two uplink fading patterns, and $r_{i_1}[k_\ell]$ and $r_{i_1}[k_{\ell+1}]$ belong to the other one. The likelihood of this event is described in terms of the joint pdf of $\mathbf{a}_0 = \left(r_{i_0}[k_\ell], r_{i_0}[k_{\ell+1}]\right)^T$ and $\mathbf{b}_0 = \left(r_{i_1}[k_\ell], r_{i_1}[k_{\ell+1}]\right)^T$. With a Jakes fading model, this pdf is given by

$$p(\mathbf{a}_0, \mathbf{b}_0) = \frac{1}{(2\pi)^2 |\mathbf{\Psi}|} \exp\left\{ -\frac{\mathbf{a}_0^\dagger \mathbf{\Psi}^{-1} \mathbf{a}_0 + \mathbf{b}_0^\dagger \mathbf{\Psi}^{-1} \mathbf{b}_0}{2} \right\} \tag{3.18}$$

45

where

$$\mathbf{\Psi} = \sigma_g^2 \begin{bmatrix} 1 & J_0\left(2\pi(k_\ell - k_{\ell+1})f_d T\right) \\ J_0\left(2\pi(k_\ell - k_{\ell+1})f_d T\right) & 1 \end{bmatrix} + N_0 \begin{bmatrix} 1 & 0 \\ 0 & 1 \end{bmatrix} \tag{3.19}$$

is the covariance matrix of the two fading-plus-noise patterns in intervals k_ℓ and $k_{\ell+1}$. As for the event of a change in associations, it is modeled by declaring $r_{i_0}[k_\ell]$ and $r_{i_1}[k_{\ell+1}]$ belongs to one of the two uplink fading patterns, and $r_{i_1}[k_\ell]$ and $r_{i_0}[k_{\ell+1}]$ belongs to the other one. The likelihood of this event is measured through the joint pdf of $\mathbf{a}_1 = \left(r_{i_0}[k_\ell], r_{i_1}[k_{\ell+1}]\right)^T$ and $\mathbf{b}_1 = \left(r_{i_1}[k_\ell], r_{i_0}[k_{\ell+1}]\right)^T$, which is

$$p(\mathbf{a}_1, \mathbf{b}_1) = \frac{1}{(2\pi)^2 |\mathbf{\Psi}|} \exp\left\{ -\frac{\mathbf{a}_1^\dagger \mathbf{\Psi}^{-1} \mathbf{a}_1 + \mathbf{b}_1^\dagger \mathbf{\Psi}^{-1} \mathbf{b}_1}{2} \right\}. \tag{3.20}$$

Finally, the sorting algorithm declares that there is no change of associations if $p(\mathbf{a}_0, \mathbf{b}_0) > p(\mathbf{a}_1, \mathbf{b}_1)$; else there is a change. After taking natural log of the two pdfs and eliminating common terms, the decision on whether there is a change in associations or not reduces to computing

$$\begin{aligned} H_0 &= \mathrm{Re}\left\{ r_{i_0}[k_{\ell+1}]r_{i_0}^*[k_\ell] + r_{i_1}[k_{\ell+1}]r_{i_1}^*[k_\ell] \right\}, \\ H_1 &= \mathrm{Re}\left\{ r_{i_0}[k_{\ell+1}]r_{i_1}^*[k_\ell] + r_{i_1}[k_{\ell+1}]r_{i_0}^*[k_\ell] \right\}, \end{aligned} \tag{3.21}$$

and setting the change indicator bit according to

$$d[\ell+1] = \begin{cases} 0, & H_0 > H_1, \\ 1, & H_0 < H_1. \end{cases} \tag{3.22}$$

Assuming that in interval k_ℓ, the sorter declares that the decision feedback-based channel estimates are $\tilde{g}_A[k_\ell] = r_{i_0}[k_\ell]$ and $\tilde{g}_B[k_\ell] = r_{i_1}[k_\ell]$. If the indicator bit is a "1", a change in

associations is needed and the sorter updates the fading estimates in interval $k_{\ell+1}$ as $\tilde{g}_A[k_{\ell+1}] = r_{i_1}[k_{\ell+1}]$ and $\tilde{g}_B[k_{\ell+1}] = r_{i_0}[k_{\ell+1}]$. On the other hand when the indicator bit is a "0", there is no change in associations and the sorter sets $\tilde{g}_A[k_{\ell+1}] = r_{i_0}[k_{\ell+1}]$ and $\tilde{g}_B[k_{\ell+1}] = r_{i_1}[k_{\ell+1}]$. Note that by definition, we set the decision feedback based channel estimates in interval k_0 to be $\tilde{g}_A[k_0] = r_{i_0}[k_0]$ and $\tilde{g}_B[k_0] = r_{i_1}[k_0]$. Fig. 3.8 further illustrates the role plays by the indicator bits $d[\ell]$ in the sorting algorithm.
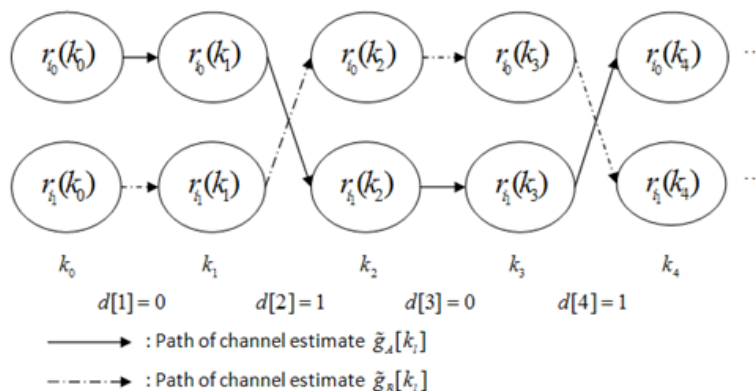
Fig. 3.8: Example of channel sorting with indicator bits $d[\ell]$.

According to Fig 3.8, the indicated bits $d[k_\ell]$ are found to be 1 in intervals k_2 and k_4. Hence, there are changes in association in those intervals, as illustrated by the crossing of the solid and dashed paths when progressing from interval k_1 to k_2, and from k_3 to k_4.

As observed from (3.21), the computation of the decision statistics H_0 and H_1 requires 4 MADs each time the symbols from the users are detected to different. Given that this occurs on average, at a fraction of

$$Q = (M-1)/M \quad , \tag{3.23}$$

the mean complexity is $4\bar{L}$ MADs per block of N symbols, where

47

$$\overline{L} = QN = (M-1)N/M \qquad (3.24)$$

is the average number of intervals (per block of N symbols) that the two users transmit different symbols.

Once the channel estimates in all the intervals where the users' symbols are detected to be different are obtained, they are organized in to column vectors

$$\tilde{\mathbf{g}}_l = \left[\tilde{g}_l[k_0], \tilde{g}_l[k_1], ..., \tilde{g}_l[k_{L-1}]\right]^T, \quad l = A, B \ . \qquad (3.25)$$

The final channel estimates will be generated by forwarding $\tilde{\mathbf{g}}_l$ and the indices $k_0, k_1, ..., k_{L-1}$ to an interpolation filter. Two types of interpolators are discussed in the following subsections: MMSE interpolators, and polynomial interpolators based on least square (LS) curve fit.

3.3.2. MMSE Interpolation

In order to obtain the final channel estimates

$$\hat{\mathbf{g}}_l = \left[\hat{g}_l[1], \hat{g}_l[2], ..., \hat{g}_l[N]\right]^T, \quad l = A, B \qquad (3.26)$$

from the initial estimates $\tilde{\mathbf{g}}_l$ in (3.25), we can use an optimal interpolation filter in the MMSE sense. The optimal interpolation filter in this case is

$$\mathbf{H} = \mathbf{\Phi}_{\mathbf{g}\tilde{\mathbf{g}}} \mathbf{\Phi}_{\tilde{\mathbf{g}}\tilde{\mathbf{g}}}^{-1}, \qquad (3.27)$$

where $\mathbf{\Phi}_{\mathbf{g}\tilde{\mathbf{g}}} = \frac{1}{2} E\left(\mathbf{g}_l \tilde{\mathbf{g}}_l^\dagger\right)$ is the correlation matrix between the actual gain pattern $\mathbf{g}_l = \left[g_l[1], g_l[2], ... g_l[N]\right]^T$ and the initial estimate $\tilde{\mathbf{g}}_l$, $l = A, B$, in (3.25), and $\mathbf{\Phi}_{\tilde{\mathbf{g}}\tilde{\mathbf{g}}} = \frac{1}{2} E\left(\tilde{\mathbf{g}}_l \tilde{\mathbf{g}}_l^\dagger\right)$ is the covariance matrix of the $\tilde{\mathbf{g}}_l$'s. Assuming that both the preliminary

decisions made by the relay receiver and the channel sorter are correct, then $\tilde{g}_l[k_m] = g_l[k_m] + e_\ell[k_m]$, $l = A, B$, where $e_\ell[k_m] = CN(0, N_0)$ represents the noise component at the output of the correlator associated with the transmitted symbol of the ℓth user in the $k_m^{\ th}$ interval. As a result, the $(n,m)^{th}$ element of $\Phi_{g\tilde{g}}$ is thus

$$
\begin{aligned}
\phi_{g\tilde{g}}(n,m) &= \tfrac{1}{2} E\left[g_l[n]\tilde{g}_l^*[k_m] \right] \\
&= \tfrac{1}{2} E\left[g_l[n]\left(g_l^*[k_m] + e_\ell^*[k_m] \right) \right] \\
&= \sigma_g^2 J_0\left(2\pi(n - k_m) f_d T \right), \qquad n = 1, 2, ... N, \ m = 0, 1, ... L - 1
\end{aligned}
\qquad (3.28)
$$

and the $(p,q)^{th}$ element of $\Phi_{\tilde{g}\tilde{g}}$ is

$$
\begin{aligned}
\phi_{\tilde{g}\tilde{g}}(p,q) &= \frac{1}{2} E\left[\tilde{g}_l[k_p]\tilde{g}_l^*[k_q] \right] \\
&= \frac{1}{2} E\left[\left(g_l[k_p] + e[k_p] \right)\left(g_l^*[k_q] + e^*[k_q] \right) \right] \\
&= \sigma_g^2 J_0\left(2\pi(k_p - k_q) f_d T \right) + N_0 \delta_{p,q}, \qquad p, q \in \{0, 1, ..., L - 1\} \ .
\end{aligned}
\qquad (3.29)
$$

Due to the randomness in the indices $\{k_0, k_1, ..., k_{L-1}\}$, the matrices $\Phi_{g\tilde{g}}$ and $\Phi_{\tilde{g}\tilde{g}}$ used in computing the optimal interpolation filter changes from a block of data to the next. While these matrices can be obtained through proper pruning of the rows and columns of $\Phi_{gg} = \tfrac{1}{2} E\left(g_l g_l^\dagger \right)$ and $\Phi_{rr} = \Phi_{gg} + N_o I_N$ (which can be pre-computed), the complication arises during the inversion of $\Phi_{\tilde{g}\tilde{g}}$. Due to the randomness of $\{k_0, k_1, ..., k_{L-1}\}$, the matrix $\Phi_{\tilde{g}\tilde{g}}$ is not necessarily Toeplitz and the efficient Levinson-Durbin algorithm cannot be used to compute its inverse to obtain the optimal interpolator in (3.27). Using a brute-force method, the inversion of $\Phi_{\tilde{g}\tilde{g}}$ has a complexity in the order of $O(L^3)$. Given the event that the two users send different data symbols follows a binomial distribution, over a block of N symbols, the expected value of L^3 is

$$
E\left[L^3 \right] = NQ\left(1 - 3Q + 3NQ + 2Q^2 - 3NQ^2 + N^2 Q^2 \right) \approx N^3 Q^3 = \bar{L}^3,
\qquad (3.30)
$$

and the mean complexity for inverting $\boldsymbol{\Phi}_{\tilde{g}\tilde{g}}$ is thus $O(\bar{L}^3)$, where $\bar{L}$ is given by (3.24). Also, because the computational complexities of $\boldsymbol{\Phi}_{\tilde{g}\tilde{g}}^{-1}$ multiplied by $\boldsymbol{\Phi}_{g\tilde{g}}$ and $\boldsymbol{\Phi}_{g\tilde{g}}\boldsymbol{\Phi}_{\tilde{g}\tilde{g}}^{-1}$ multiplied by $\tilde{\mathbf{g}}_l$ are much smaller than the complexity required for inverting $\boldsymbol{\Phi}_{\tilde{g}\tilde{g}}$, $O(\bar{L}^3)$ is simply used as the complexity of the MMSE interpolator. As an example, for binary modulations and a window size of $N = 64$, $\bar{L}^3 = 32^3$ and the complexity per symbol required for matrix inversion is thus in the order of $\bar{L}^3 / N = 512$ MADs. Reducing the window size to $N = 32$ (with $\bar{L}^3 = 16^3$) will cut the complexity per symbol down to $\bar{L}^3 / N = 128$, a more manageable figure. This polynomial complexity prevents the use of large block sizes.

The final channel estimates after MMSE interpolation are

$$\hat{\mathbf{g}}_l = \mathbf{H}\tilde{\mathbf{g}}_l, \qquad\qquad l = A, B, \qquad\qquad (3.31)$$

and the corresponding MSE at the kth symbol position is given by

$$\mu_0^2[k] = \sigma_g^2 - \tilde{\boldsymbol{\psi}}_k \boldsymbol{\Phi}_{\tilde{g}\tilde{g}}^{-1} \tilde{\boldsymbol{\psi}}_k^{\dagger}, \qquad\qquad (3.32)$$

where $\tilde{\boldsymbol{\psi}}_k$ is just the kth row in $\boldsymbol{\Phi}_{g\tilde{g}}$. The normalized MSE across the entire block of N symbols is

$$\mu_N^2 = \frac{1}{\sigma_g^2 N} \sum_{k=0}^{N-1} \mu_0^2[k] = 1 - \frac{1}{\sigma_g^2 N} \text{trace}\left\{ \boldsymbol{\Phi}_{g\tilde{g}} \boldsymbol{\Phi}_{\tilde{g}\tilde{g}}^{-1} \boldsymbol{\Phi}_{g\tilde{g}}^{\dagger} \right\}. \qquad (3.33)$$

It should be emphasized that the NMSE in the above equation is dependent on the locations of those intervals where $s_A[k] \neq s_B[k]$, in other words, dependent on the indices $\{k_0, k_1, ..., k_{L-1}\}$. The true average NMSE can only be obtained by the taking the average of (3.33) over all random data patterns, which is computational intensive, especially for large block size N. For this reason, no attempt was made to compute numerically the average of (3.33).

As mentioned earlier, a problem with the MMSE interpolator is its $O(\bar{L}^3)$ complexity in the inversion of $\mathbf{\Phi}_{\tilde{g}\tilde{g}}$. An alternative is to use a polynomial interpolator with least square curve fit.

3.3.3. Polynomial Interpolation - Least Square Curve Fit

The principle behind polynomial interpolation is to represent the actual fading patterns $\mathbf{g}_l = [g_l[1], g_l[2], ... g_l[N]]^T$ and the initial estimate $\tilde{\mathbf{g}}_l$, $l = A, B$, using P^{th} order polynomials $h_l[t] = h_{l,0} + h_{l,1}t + ... + h_{l,P}t^P$, where $t \in \{1, 2, ..., N\}$ is the symbol index and $h_l[t]$ is the estimate of $g_l[t]$ at symbol interval t. The coefficients in the two polynomials are chosen to minimize the square errors when used to represent the two $\tilde{\mathbf{g}}_l$. Detail derivations of these polynomials are provided below.

Using polynomial interpolation, the initial estimate $\tilde{g}_l[k_\ell]$ provided by the channel sorter is replaced by

$$h_l[k_\ell] = h_{l,0} + h_{l,1}k_\ell + ... + h_{l,P}k_\ell^P, \qquad \ell = 0, 1, ..., L-1. \tag{3.34}$$

The total square error is thus

$$
\begin{aligned}
R_l^2 &= \sum_{j=0}^{L-1} \left| \tilde{g}_l[k_j] - \left(h_{l,0} + h_{l,1}k_j + ... + h_{l,P}k_j^P \right) \right|^2 \\
&= \sum_{j=0}^{L-1} \left| \text{Re}\left(\tilde{g}_l[k_j] \right) - \left(x_{l,0} + x_{l,1}k_j + ... + x_{l,P}k_j^P \right) \right|^2 \\
&\quad + \sum_{j=0}^{L-1} \left| \text{Im}\left(\tilde{g}_l[k_j] \right) - \left(y_{l,0} + y_{l,1}k_j + ... + y_{l,P}k_j^P \right) \right|^2,
\end{aligned}
\tag{3.35}
$$

where $x_{l,P}$ and $y_{l,P}$ are respectively the real and imaginary parts of $h_{l,P}$, $p = 0,1,...,P$.
To minimize R_l^2, the coefficients $h_{l,p}$, $p = 0,1,...,P$, should be chosen such that the partial derivatives with respect to these coefficients are all zero, i.e.

$$\frac{\partial\left(R_l^2\right)}{\partial x_{l,p}} = -2\sum_{j=0}^{L-1}\left[\mathrm{Re}\left(\tilde{g}_l[k_j]\right) - \left(x_{l,0} + x_{l,1}k_j + ... + x_{l,P}k_j^{\,P}\right)\right]k_j^{\,P} = 0, \qquad p = 0,1,...,P;$$

$$\frac{\partial\left(R_l^2\right)}{\partial y_{l,p}} = -2\sum_{j=0}^{L-1}\left[\mathrm{Im}\left(\tilde{g}_l[k_j]\right) - \left(y_{l,0} + y_{l,1}k_j + ... + y_{l,P}k_j^{\,P}\right)\right]k_j^{\,P} = 0, \qquad p = 0,1,...,P.$$

$$(3.36)$$

Re-introducing complex notation, these equations can be expressed in matrix form as

$$\begin{bmatrix} L & \sum_0^{L-1}k_j & \cdots & \sum_0^{L-1}k_j^P \\ \sum_0^{L-1}k_j & \sum_0^{L-1}k_j^2 & \cdots & \sum_0^{L-1}k_j^{P+1} \\ \vdots & \vdots & \ddots & \vdots \\ \sum_0^{L-1}k_j^P & \sum_0^{L-1}k_j^{P+1} & \cdots & \sum_0^{L-1}k_j^{2P} \end{bmatrix}\begin{bmatrix} h_{l,0} \\ h_{l,1} \\ \vdots \\ h_{l,P} \end{bmatrix} = \begin{bmatrix} \sum_0^{L-1}\tilde{g}_l[k_j] \\ \sum_0^{L-1}k_j\tilde{g}_l[k_j] \\ \vdots \\ \sum_0^{L-1}k_j^P\tilde{g}_l[k_j] \end{bmatrix}, \qquad (3.37)$$

or more explicitly as

$$\begin{bmatrix} 1 & 1 & \cdots & 1 \\ k_0 & k_1 & \cdots & k_{L-1} \\ \vdots & \vdots & \ddots & \vdots \\ k_0^P & k_1^P & \cdots & k_{L-1}^P \end{bmatrix}\begin{bmatrix} 1 & k_0 & \cdots & k_0^P \\ 1 & k_1 & \cdots & k_1^P \\ \vdots & \vdots & \ddots & \vdots \\ 1 & k_{L-1} & \cdots & k_{L-1}^P \end{bmatrix}\begin{bmatrix} h_{l,0} \\ h_{l,1} \\ \vdots \\ h_{l,P} \end{bmatrix} = \begin{bmatrix} 1 & 1 & \cdots & 1 \\ k_0 & k_1 & \cdots & k_{L-1} \\ \vdots & \vdots & \ddots & \vdots \\ k_0^P & k_1^P & \cdots & k_{L-1}^P \end{bmatrix}\begin{bmatrix} \tilde{g}_l[k_0] \\ \tilde{g}_l[k_1] \\ \vdots \\ \tilde{g}_l[k_{L-1}] \end{bmatrix}. \qquad (3.38)$$

Let

$$\mathbf{X} = \begin{bmatrix} 1 & k_0 & \cdots & k_0^P \\ 1 & k_1 & \cdots & k_1^P \\ \vdots & \vdots & \ddots & \vdots \\ 1 & k_{L-1} & \cdots & k_{L-1}^P \end{bmatrix}, \qquad (3.39)$$

52

be the matrix containing the sampling times raised to different integer powers and

$$
\mathbf{h}_l = \begin{bmatrix} h_l[k_0] \\ h_l[k_1] \\ \vdots \\ h_l[k_{L-1}] \end{bmatrix},
\tag{3.40}
$$

the vector containing the coefficients of the interpolation polynomial $h_l[t]$. Then Eqn. (3.38) can be rewritten as as $(\mathbf{X}^T\mathbf{X})\mathbf{h}_l = \mathbf{X}^T\tilde{\mathbf{g}}_l$, $l = A, B$. As a result, the LS curve fitting polynomials are given by

$$
\mathbf{h}_l = (\mathbf{X}^T\mathbf{X})^{-1}\mathbf{X}^T\tilde{\mathbf{g}}_l, \qquad l = A, B,
\tag{3.41}
$$

and the final channel estimates $h_l[t] = h_{l,0} + h_{l,1}t + \dots + h_{l,P}t^P = \hat{g}_l[t]$, at $t = 1, 2, \dots, N$, are given by

$$
\begin{aligned}
\hat{\mathbf{g}}_l &= \mathbf{Y}\mathbf{h}_l = \left(\mathbf{Y}(\mathbf{X}^T\mathbf{X})^{-1}\mathbf{X}^T \right)\tilde{\mathbf{g}}_l \\
&= \mathbf{F}\tilde{\mathbf{g}}_l
\end{aligned}
\qquad l = A, B
\tag{3.42}
$$

where

$$
\mathbf{Y} = \begin{bmatrix}
1 & 1 & 1 & \cdots & 1 \\
1 & 2 & 2^2 & \cdots & 2^P \\
1 & 3 & 3^2 & \cdots & 3^P \\
\vdots & \vdots & \vdots & \ddots & \vdots \\
1 & N & N^2 & \cdots & N^P
\end{bmatrix}
\tag{3.43}
$$

is a matrix containing all the symbol times raised to various powers, and

$$
\mathbf{F} = \mathbf{Y}(\mathbf{X}^T\mathbf{X})^{-1}\mathbf{X}^T.
\tag{3.44}
$$

is the effective interpolation filter. Finally, it can be shown that the NMSE of the polynomial interpolator is given by

$$\beta_N^2 = 1 - \frac{1}{\sigma_g^2 N} \text{trace}\left\{ \mathbf{\Phi}_{g\tilde{g}} \mathbf{F}^\dagger + \mathbf{F}\mathbf{\Phi}_{g\tilde{g}}{}^\dagger - \mathbf{F}\mathbf{\Phi}_{\tilde{g}\tilde{g}} \mathbf{F}^\dagger \right\} \ . \tag{3.45}$$

As in the case of MMSE interpolation, the above NMSE is dependent on the locations of those intervals where $s_A[k] \neq s_B[k]$, i.e., the indices $\{k_0, k_1, ..., k_{L-1}\}$. As explained earlier, there are prohibitively larger numbers of such combinations. As such, no attempt was made to compute numerically the average of (3.45).

Regarding the computational complexity of the polynomial interpolator, the formation of the matrix $\mathbf{X}$ in (3.39) requires $L(P\text{-}1)$ multiplications, while $\mathbf{X}^\mathbf{T}\mathbf{X}$ in (3.42) is a $(P+1)\times(P+1)$ matrix and it requires another $L(P+1)^2$ arithmetic operations to compute. The computation of the inverse of $\mathbf{X}^\mathbf{T}\mathbf{X}$ has a complexity of $O\left((P+1)^3\right)$, and the multiplication of $\left(\mathbf{X}^T\mathbf{X}\right)^{-1}$ by $\mathbf{X}^T$, $\left(\mathbf{X}^T\mathbf{X}\right)^{-1}\mathbf{X}^T$ by $\tilde{\mathbf{g}}_l$, $l = A, B$, and $\left(\mathbf{X}^T\mathbf{X}\right)^{-1}\mathbf{X}^T\tilde{\mathbf{g}}_l$ by $\mathbf{Y}$, require $L(P+1)^2$, $2L(P-1)$, and $2N(P+1)$ MADs respectively. As shown in the result section, P is typically a small value, $P=2$ or 3. After taking the expected value of the sum of these individual complexities, the mean complexity of the proposed LS estimator is

$$\text{O}_{LS} = (P+1)^3 + NQ(P-1) + 2N(P+1)(1+Q) + 2NQ(P+1)^2, \tag{4.46}$$

where Q is given by (4.23). As such, the polynomial interpolator has a much lower complexity than the MMSE interpolator. Another advantage of the polynomial interpolator over the MMSE interpolator is that it does not require knowledge of the signal and noise statistics.

Table 3.1 summarizes the complexity of the different components of the proposed decision feedback receiver, measured in number of MAD operations per symbol, for

different values of modulation size M, processing block size N, and polynomial order P.

M	N	Initial Partial-coherent Detector	Sorting Algorithm	MMSE Interpolator	Polynomial Interpolator	
					$P=2$	$P=3$
2	16	16	2	32	20	33
2	32	32	2	128	19	31
2	64	64	2	512	19	30
4	16	16	4	108	27	44
4	32	32	4	432	26	42
4	64	64	4	1728	25	41

Table 3.1: Per-symbol of component of the decision feedback receiver as functions of the modulation size M, block size N and LS interpolator order P (a) initial partial coherent detector, N ; (b) sorting algorithm, complexity, M ; (c) MMSE interpolator, $\overline{L}^3$;(d) polynomial interpolator, $(P+1)^3 / N + Q(P-1) + 2(P+1)(1+Q) + 2Q(P+1)^2$.

In the next subsection, the performance of the MMSE estimator and the LS estimator will be compared.

3.3.4. Numerical Results

In this section, simulation results on the mean-square channel estimation error and the BER are provided for the proposed DFB receiver operating in a time-selective fading environment with a fade rate of $f_d T = 0.005$. This fade rate is found to be the highest that the proposed DFB receiver can support while maintaining a performance close to ideal coherent detection. Although it cannot be considered as fast fading in the context of older generations narrowband systems (data rate in the order of tens of kbps), an $f_d T = 0.005$ is more than sufficient to handle all realistic mobility conditions for 3G/4G-type transmission rates (at 1 Mbps or above) and frequencies (in the 1-2 GHz range). For each block of data symbols simulated, we first calculated the normalized square error (NSE) in the kth symbol interval as

$$\chi^2[k] = \frac{1}{2\sigma_g}\left(|g_A[k] - \hat{g}_A[k]|^2 + |g_B[k] - \hat{g}_B[k]|^2\right),\qquad(3.47)$$

and then took the average across the block to obtain the per-symbol NSE (PS-NSE)

$$\chi_N^2 = \frac{1}{N}\sum_{k=1}^{N}\chi^2[k].\qquad(3.48)$$

These errors include not only standard interpolation errors, but also the effect of erroneous decision feedback. Many independent data blocks are simulated and the averages of these errors are logged and presented in the figures in this section. Note that when the channel SNR is large, most of the initial decisions are correct and the simulation results on the PS-NSE presented in this section will approach the averages of position-dependent NMSE in (3.33) and (3.45).

We first present in Figs 3.9 and 3.10 the simulated NSE of the MMSE interpolator at different symbol positions within the block, for block sizes of $N = 16$ and 32 respectively. According to (3.32), the vector $\tilde{\psi}_k$ is affected by the symbol interval index k. Therefore, the NSE $\chi^2[k]$ at different symbol intervals are different. It is observed from the figures that the NSEs in the middle of the block are smaller than those at the two ends. The discrepancy is larger for larger SNRs. It is deduced that the PS-NSE-N in (3.48) will be dominated by those NSEs at the edges.

Fig. 3.11 shows the PS-NSE-N (3.48) of the MMSE interpolator in a $M = 2$ system with different processing block sizes. The simulated results reveal that while the PS-NSE-N decreases with an increase in SNR, the curves for block sizes of $N = 64$ and $N = 128$ exhibit noticeable irreducible error behavior. On the other hand, the curve for a block size of $N = 32$ provides the lowest value of χ_N^2 (3.48) over a wide range of SNRs. It can thus be considered as the "optimal" processing block size. Note that the reason why a larger block size may lead to a larger value of χ_N^2 is because there are now more chances that the two fading patterns cross each other in the complex plane, creating a

potential confusion in the channel tracking algorithm in (3.21)-(3.22). This is especially true at large SNR where the effect of noise diminishes and the accuracy of channel estimation is predominantly determined by the correctness of the channel sorter.

Fig. 3.12 shows the PS-NSE-N of LS interpolators of different orders in a $M = 2$ system with a block size of $N = 32$. As observed, the $P = 3$ (cubic) interpolator has very large errors compared to the other two. Of the remaining two interpolators, the $P=1$ (linear) interpolator is better at SNR below 30 dB while the $P = 2$ (quadratic) interpolator is better at higher SNR. To avoid the potential of a slower-than-inverse SNR (or even irreducible error floor) behavior in the BER curve, we will thus fix P to 2 for polynomial interpolators from hereon.

Fig. 3.13 shows the PS-NSE-N of the 2nd order LS interpolator with different block sizes. As in the case of the MMSE interpolator in Fig. 3.11, a block size of $N = 32$ provides the best performance over a while range of SNRs.

Fig 3.14 and Fig. 3.15 show the BER of the proposed $M = 2$ DFB receiver with MMSE and second order polynomial interpolation, respectively. Processing block sizes of N =16, 32, 64 and 128 are considered in both cases. To put the performance of the proposed receiver in proper perspective, we include in the figures the BER curves (both bounds and simulations) of both the partial-coherent and full-coherent detectors. Note that the bound for the partial-coherent detector is based on perfect sum-gain estimation while the simulation results were obtained under actual (imperfect) estimation (3.31) (3.42). Several observations are made. First, the partial-coherent detector indeed performs as its bound promises, as the simulation results using actual channel sum-gain estimates almost coincide with the bound obtained under the assumption of perfect sum-gain estimation. The SNR requirement of the partial-coherent detector to attain a BER of 10^{-3} is 37dB. Secondly, for both the MMSE and polynomial interpolators, the "optimal" block size is $N = 32$. With this "optimal" block size, the SNR requirements for the proposed DFB receiver, with MMSE and second order polynomial interpolation, to attain a BER of a10^{-3} are cut to 31 dB and 31.5 dB respectively. These figures correspond to

improvements in power efficiency over the partial-coherent detector of 6 and 5.5 dB respectively. Thirdly, the proposed DFB receiver with MMSE and second order polynomial interpolation is within 1 dB and 1.5 dB of full-coherent detection at a BER of 10^{-3}, respectively. These are impressive performance.

We compare explicitly in Fig. 3.16 the BER performance of the two interpolation methods in the proposed $M = 2$ DFB receiver. According to the figure, the MMSE interpolator is less sensitive to the change in block size. Moreover, at large SNR, the $N = 32$ MMSE interpolator provides a 0.5 (to 1) dB improvement in SNR over its LS counterpart. Thus from the performance perspective, we conclude that the MMSE interpolator is preferred over the LS interpolator. However, it should be emphasized that the latter has a lower implementation complexity and does not require knowledge of channel statistics.

Finally, we consider the $M = 4$ case. Fig. 3.17 shows the simulation results of the initial partial-coherent detector with estimated sum fading gain, the proposed DFB detector with one and two rounds of feedback, simulation results of the full-coherent detector, and the bounds of the partial-coherent detector and the full-coherent detector, all at a Doppler frequency of $f_d T = 0.005$ and a block size of $N = 32$. It is observed that the proposed DFB detector, with one round of feedback, already provides an impressive 5.5 dB improvement in SNR over the partial-coherent detector at a BER at 10^{-3}. There is no significant change in SNR through imposing another round of feedback. As mentioned before in Fig 3.7, for the $M = 4$ case, the bound of the full-coherent detector is not tight, and there exists a 2dB gap between the full-coherent simulation and the bound.
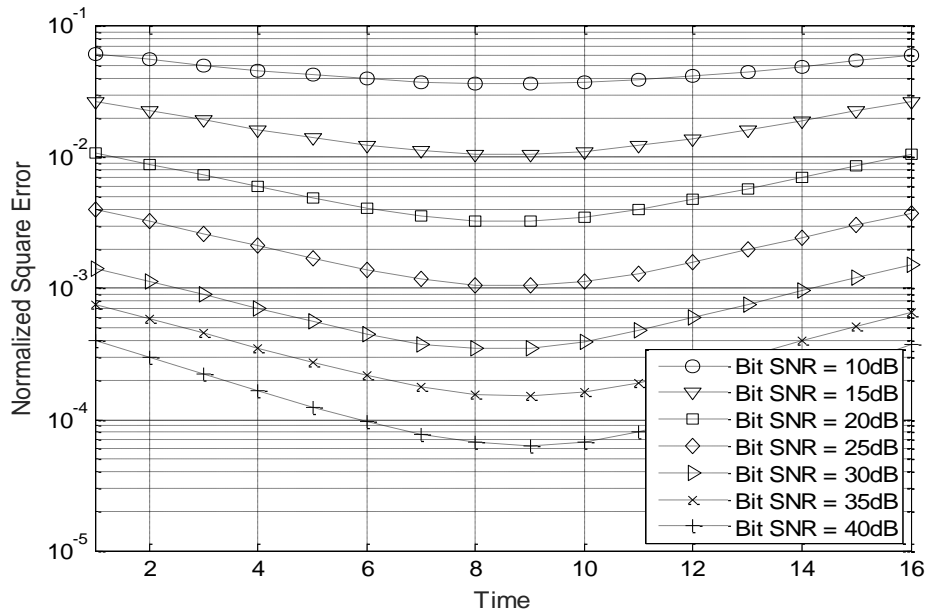
Fig.3.9: Simulated NSE of the $M = 2$ MMSE interpolator at different symbol intervals and at different SNRs. The processing block size is $N = 16$.
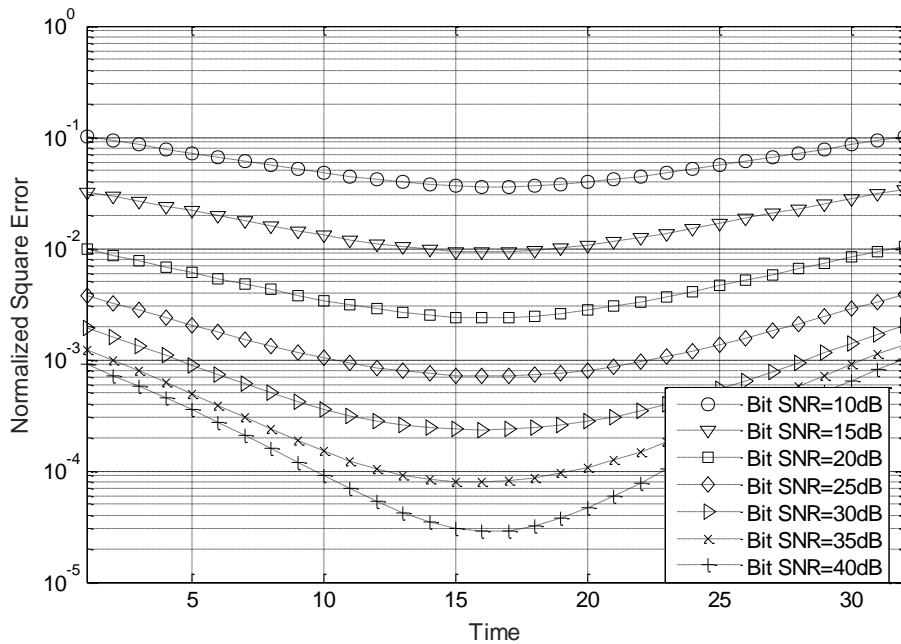
Fig. 3.10: Simulated NSE of the $M = 2$ MMSE interpolator at different symbol intervals and at different SNRs. The processing block size is $N = 32$.
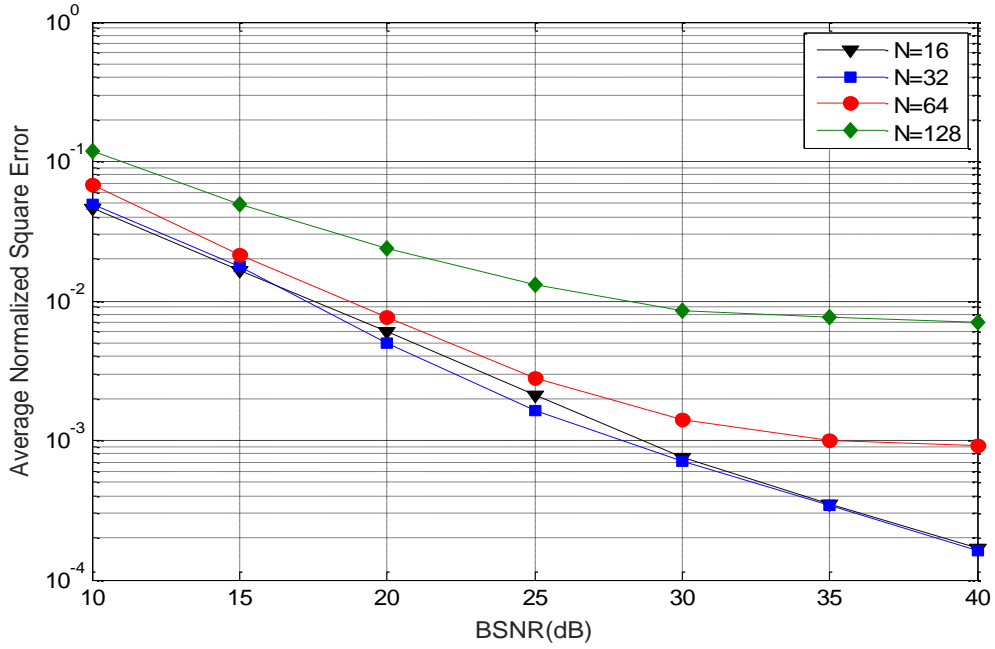
Fig. 3.11: Simulated PS-NSE-N of the $M = 2$ MMSE interpolator at $f_d T = 0.005$ and different processing block sizes
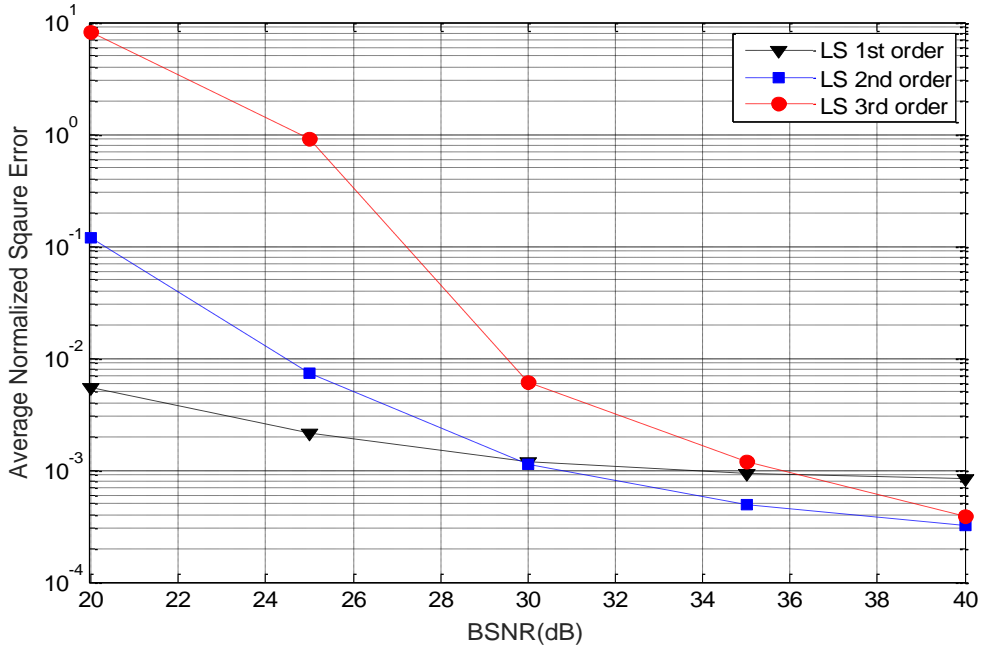
Fig. 3.12: Simulated PS-NSE-N of the LS curve fitting interpolator at $f_d T = 0.005$ with different polynomial orders. The processing block size is $N = 32$.
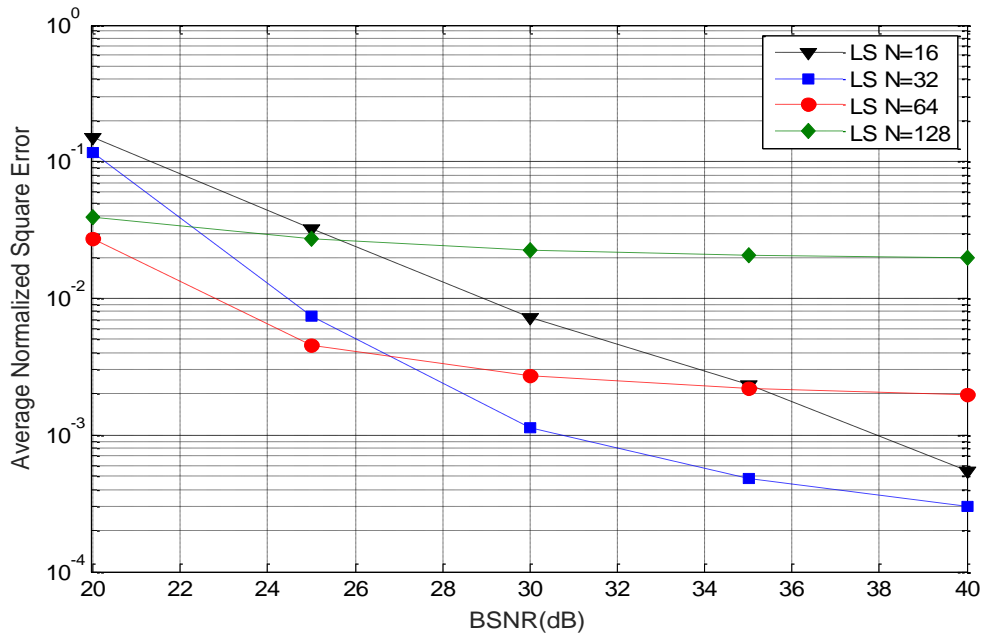
Fig. 3.13: Simulated PS-NSE-*N* of the 2nd order LS curve fitting interpolator at $f_d T = 0.005$ and different block sizes.
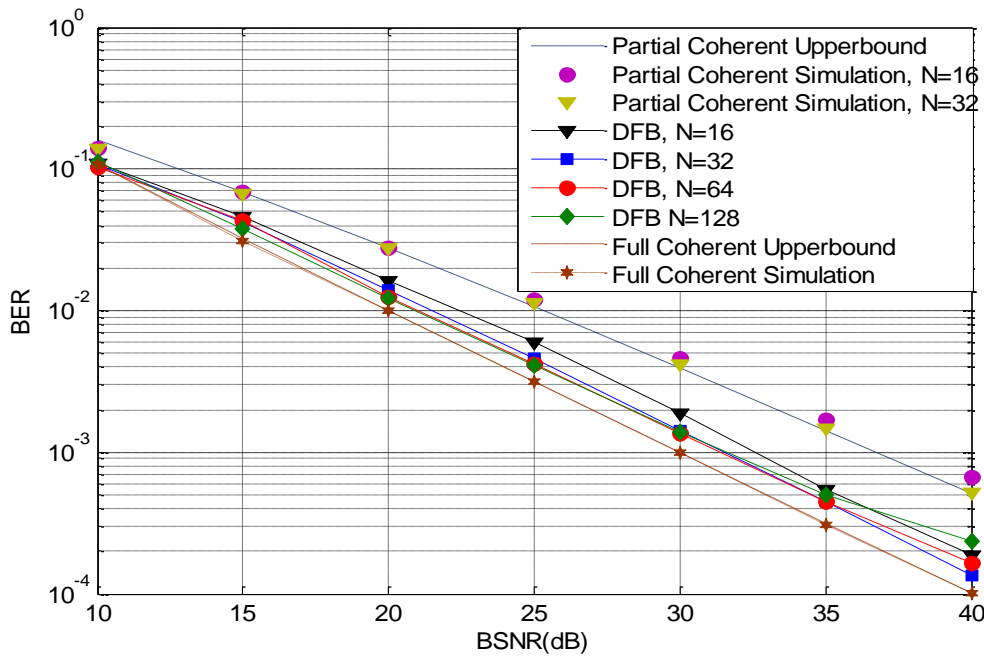
Fig. 3.14: Simulated BER of the proposed $M = 2$ DFB receiver at $f_d T = 0.005$ with MMSE channel interpolation and different processing block sizes.
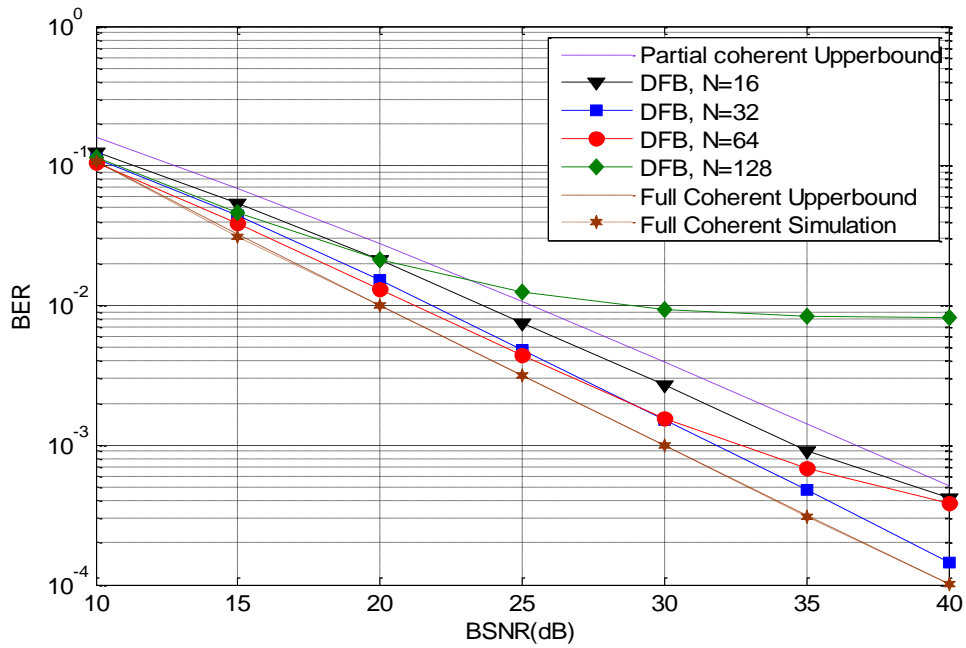
Fig. 3.15: Simulated BER of the proposed $M = 2$ DFB receiver at $f_dT = 0.005$ with 2nd order LS interpolation and different processing block sizes.
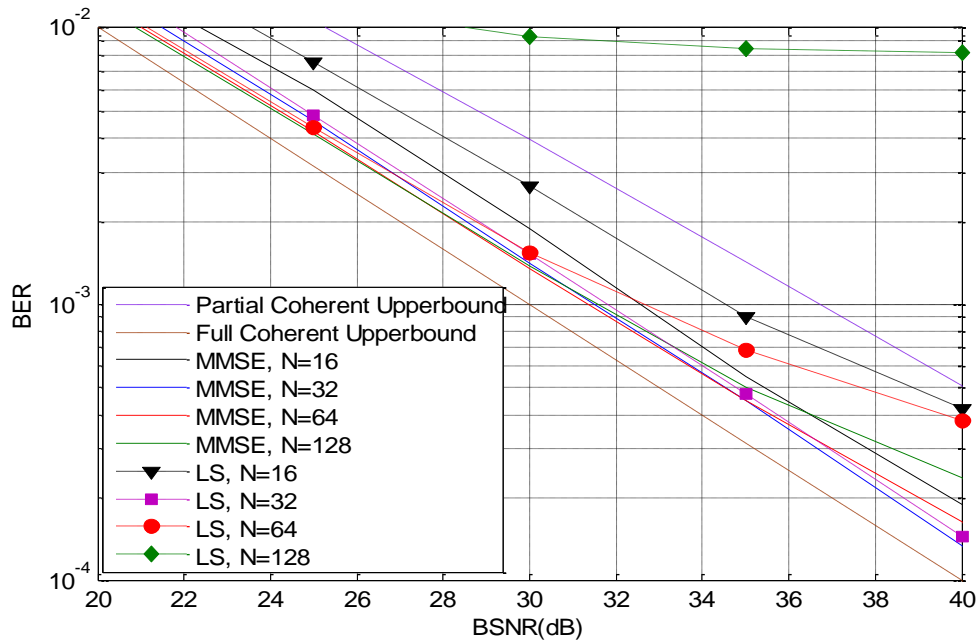
Fig. 3.16: Simulated BER of the proposed $M = 2$ DFB receiver at $f_dT = 0.005$ with different channel interpolators and different processing block sizes.
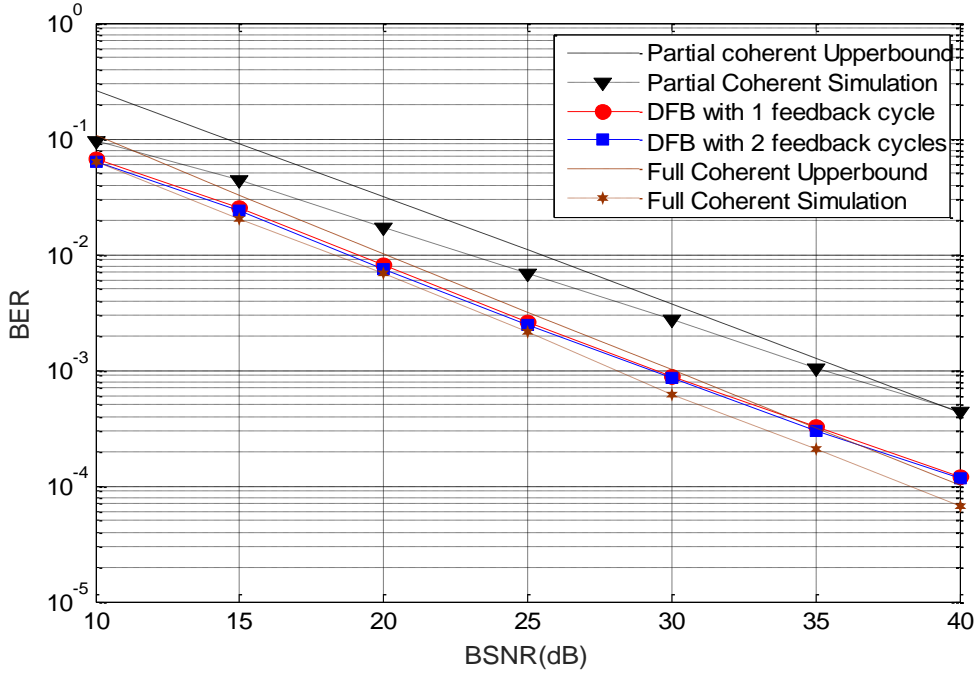
Fig. 3.17: Simulated BER of the proposed $M = 4$ DFB receiver at $f_d T = 0.005$ and MMSE channel interpolation. The processing block size is $N = 32$.

3.4. Conclusion

Built on the promises of the (idealized) partial-coherent in Chapter 2, we propose in this chapter a novel decision feedback receiver for two-phase two-way relay with physical network coding and orthogonal signaling. The design begins with a practical MMSE estimator of the sum-gain in the partial-coherent detector that delivers a performance close to perfect estimation. Then in realizing that when the initial decisions from the partial-coherent detector indicate the symbols transmitted by the two users are different, the individual fading gains in those intervals can be separated, we propose a simple channel identification and two channel interpolation strategies. Of the two interpolators, the MMSE interpolator is more accurate while the polynomial interpolator has a lower complexity. The performance of the entire DFB receiver is evaluated via simulation using different combinations of block size *N*, different fade rates (static fading

and at $f_dT = 0.005$) and different interpolator types. It was found that with proper choices of block size and interpolator type, the performance of the proposed DFB receiver can be brought within 1 dB of full-coherent detection, and this is achieved without the need to transmit any pilot symbols. Compared to non-coherent detection (Chapter 2), this is a 9 dB gain in power efficiency. When compared to the partial-coherent detector, the gain is 6 dB! It is thus concluded that the proposed DFB receiver is novel, its performance impressive, and the overall decision feedback methodology has strong potentials for applications in other similar systems.

Chapter 4.

Performance Comparison with DPSK

To put the performance of the proposed DFB receiver for orthogonal modulations into proper perspective, a reference DFB multiple symbol differential detector (MSDD) for DPSK modulation is introduced for comparison. Section 4.1 describes how the DFB-MSDD operates in a 2P-TWR communication system. The BER performance of the DFB-MSDD at different fade rates are provided in Section 4.2 and compared with those of the proposed DFB receiver for pilot-less orthogonal modulations. Finally, Section 4.3 concludes this chapter.

4.1. DFB-MSDD

DFB-MSDD of M-ary DPSK was first introduced in [27] for conventional point-to-point Rayleigh flat fading channels. Its application in 2P-TWR communication was first considered in [16]. In the 2P-TWR setting, the DFB-MSDD receiver works as follow.

Let $s_A[k]$ and $s_B[k]$ be users A's and B' equivalent discrete-time data symbols in the kth symbol interval, where each symbol is randomly taken from the set $S \equiv \{0,1,...,M-1\}$ with equal probability. The PSK symbols corresponding to $s_A[k]$ and $s_B[k]$ are

$$
\begin{aligned}
v_A[k] &= \exp\left(\frac{j2\pi s_A[k]}{M}\right) \\
v_B[k] &= \exp\left(\frac{j2\pi s_B[k]}{M} + j\Delta\right)
\end{aligned} \quad ; \tag{4.1}
$$

where Δ is the phase offset between user A's and user B's PSK constellations. Let the differentially encoded symbols transmitted by Source l at time slot k be $x_l[k]$, $l = A, B$. They are related to the complex data symbols in (4.1) according to

$$x_l[k] = \begin{cases} x_l[k-1]v_l[k], & k > 0 \\ 1, & k = 0 \end{cases}. \tag{4.2}$$

Adopting the same Rayleigh flat fading model as in previous chapters, the received symbol at the relay at time k is

$$r[k] = g_A[k]x_A[k] + g_B[k]x_B[k] + n[k]. \tag{4.3}$$

Different from the network coding scheme in Tables 2.1 and 2.2, the network-coded symbol $c[k]$ in this case is the remainder of the signals' sum $(s_A[k] + s_B[k])$ after division by M. This mapping scheme is also known as physical-layer differential network coding in [16]. Tables 4.1 and 4.2 provide full details of the mappings in the M=2 and M=4 systems, respectively.

Symbol s_A (decimal format)	Symbol s_A as a Binary pattern	Symbol s_B (decimal format)	Symbol s_B as a Binary pattern	Symbol c as a Binary pattern	Symbol c (decimal format)
0	0	0	0	0	0
1	1	1	1		
0	0	1	1	1	1
1	1	0	0		

Table 4.1: Mapping of the source symbol pair (s_A, s_B) into the network-coded symbol c for *DBPSK*

Symbol s_A (decimal format)	Symbol s_A as a Binary pattern	Symbol s_B (decimal format)	Symbol s_B as a Binary pattern	Symbol c as a Binary pattern	Symbol c (decimal format)
0	(0,0)	0	(0,0)		
1	(0,1)	3	(1,1)	(0,0)	0
2	(1,0)	2	(1,0)		
3	(1,1)	1	(0,1)		
0	(0,0)	1	(0,1)		
1	(0,1)	0	(0,0)	(0,1)	1
2	(1,0)	3	(1,1)		
3	(1,1)	2	(1,0)		
0	(0,0)	2	(1,0)		
1	(0,1)	1	(0,1)	(1,0)	2
2	(1,0)	0	(0,0)		
3	(1,1)	3	(1,1)		
0	(0,0)	3	(1,1)		
1	(0,1)	2	(1,0)	(1,1)	3
2	(1,0)	1	(0,1)		
3	(1,1)	0	(0,0)		

Table 4.2: Mapping of the source symbol pair (s_A, s_B) into the network-coded symbol c for *DQPSK*.

A MSDD is based on block processing and it makes optimal block decisions using the the maximum likelihood principle. Let $\mathbf{r} = [r[n-K+1], r[n-K+2],...r[n]]^T$ be K consecutive received samples at the relay. By exploiting the correlation amongst the fading gains in different symbol intervals, the MSDD makes joint decisions on $s_A[n-K+2], s_A[n-K+3],..., s_A[n]$ and $s_B[n-K+2], s_B[n-K+3],..., s_B[n]$, and consequently make joint decisions on the network-coded symbols $c[n-K+2], c[n-K+3],..., c[n]$ according to Tables 4.1 and 4.2. While such a detector has a better error performance than the conventional two-symbol ($K=2$) detector, its computation complexity is prohibitively large. On the other hand, if previous decisions on $s_A[n-K+2], s_A[n-K+3],...s_A[n-1]$ and $s_B[n-K+2], s_B[n-K+3],...s_B[n-1]$ are correct, then they can be used to dramatically reduce the search space of the most-likely sequences. This decision feedback strategy provides a good compromise between

complexity and performance. It also leads to a sliding-window approach, as opposed to the original block-wise structure. Below are the details of the DFB-MSDD.

Let $\mathbf{x}_l = diag\left(\hat{x}_l[n - K + 2],...x_l[n-1], x_l[n]\right)$, $l = A, B$, where $\hat{x}_l[k]$ is the decision on $x_l[k]$. Given these past decisions, there are only M^2 choices for $\mathbf{x}_A$ and $\mathbf{x}_B$. The fading gains affecting the transmitted symbols in these intervals are collected into the vectors $\mathbf{g}_l = \left[g_l[n - K + 1], g_l[n - K + 2],...g_l[n]\right]^T$, $l = A, B$. The covariance matrix of these complex gains is $\mathbf{\Phi}_{gg} = \frac{1}{2}E\left(\mathbf{g}_l\mathbf{g}_l^\dagger\right)$. Assuming a Jake's fading model, then the $(p, q)^{th}$ element of $\mathbf{\Phi}_{gg}$ is

$$\phi_{gg}(p,q) = \sigma_g^2 J_0(2\pi(p-q)f_dT). \tag{4.4}$$

With these definitions, the DFB-MSDD can be described as follows:

1. For each possible pair of $\left(x_A[n], x_B[n]\right)$, or equivalently, each possible pair of $\mathbf{x}_A$ and $\mathbf{x}_B$, the received vector $\mathbf{r} = \left[r[n - K + 1], r[n - K + 2],...r[n]\right]$ is complex Gaussian with a conditional pdf

$$p(\mathbf{r} \mid \mathbf{x}_A, \mathbf{x}_B) = \frac{1}{(2\pi)^K \left\| \mathbf{x}_A \mathbf{\Phi}_{gg} \mathbf{x}_A^\dagger + \mathbf{x}_B \mathbf{\Phi}_{gg} \mathbf{x}_B^\dagger + N_0 \mathbf{I}_K \right\|} \exp\left\{ -\frac{\mathbf{r}^\dagger \left(\mathbf{x}_A \mathbf{\Phi}_{gg} \mathbf{x}_A^\dagger + \mathbf{x}_B \mathbf{\Phi}_{gg} \mathbf{x}_B^\dagger + N_0 \mathbf{I}_K \right)^{-1} \mathbf{r}}{2} \right\}$$
$$\tag{4.5}$$

2. Find out which pair of transmitted symbols maximizes the conditional pdf in (4.5). This is the decisions on $\left(x_A[n], x_B[n]\right)$, and they are denoted by $\left(\hat{x}_A[n], \hat{x}_B[n]\right)$.

3. Through differential decoding, the detected data symbols can be determined and they are given by

$$\hat{s}_A[n] = -j\frac{M}{2\pi}\cdot\arg\left\{\hat{x}_A^*[n-1]\hat{x}_A[n]\right\},$$

$$\hat{s}_B[n] = -j\frac{M}{2\pi}\cdot\arg\left\{\hat{x}_B^*[n-1]\hat{x}_B[n]\right\},$$

(4.6)

and the detected network-coded symbol $\hat{c}[n]$ is determined by mappings in Table 4.1 (for the $M = 2$ case) and Table 4.2 (in the $M = 4$ case.)

It should be noted that the above method is suboptimal. The optimal model should be the one that maximizes the sum of the pdfs of all those symbol pairs of $\left(x_A[n], x_B[n]\right)$ that are mapped into the same network-coded symbol. The advantage of this suboptimal method is that it is able to provide maximization in the log domain, which is simpler to implement than the optimal one.

4.2. Simulation and Discussion

This section details the results obtained from the simulation of the DFB-MSDD for M = 2 and M = 4 DPSK systems. Qualitative comparison between the DFB-MSDD for DPSK and the DFB receiver for orthogonal modulations is made as well.

Results of the comparison for binary modulations at fade rates of $f_dT = 0$ and $f_dT = 0.005$ are shown in Figs 4.1 and 4.2. In the DBPSK case, sliding window sizes of $K = 2$ (conventional), 4, and 8 are investigated. In addition to simulating actual feedback, we also include results for ideal feedback for the $K = 4$ and $K = 8$ cases. As their names suggest, by actual feedback, the receiver uses the detection results of the previous $K - 1$ symbol pairs to detect the current symbol pair as per (4.5) and (4.6), whereas ideal feedback assumes that the previous $K - 1$ symbol pairs are all detected correctly. It is observed that the BER curves of the $K = 4$ and $K = 8$ DFB-MSDD receivers are better than that of the conventional 2 symbol detector. For example, in the static fading channel and at a BER of 10^{-3}, increasing the length of observation interval from 2 to 8 provides a

3 dB improvement in power efficiency. While the results in the figures indicate that orthogonal modulation is worse than BPSK when full CSI is available to the relay detector, the opposite is true when CSI based on decision feedback is employed. At a BER of 10^{-3}, the $K = 8$ DFB-MSDD with actual feedback is 1 dB worse than the proposed DFB receiver for orthogonal modulation in the static fading environment; when the fade rate increases to $f_d T = 0.005$, the proposed DFB scheme for orthogonal modulation has an advantage over the DFB-MSDD by 4 dB. Even with ideal feedback, the performance of the MSDD is worse than that of the proposed DFB receiver at high SNR.

The DPSK results in the previous figures were obtained under a phase offset of $\Delta = 0$ between the two users' BPSK constellations. Other values of Δ had been tested but the results obtained were similar. In the $M = 4$ case though, the BER of the DFB-MSDD depends strongly on the value of Δ, as Figs 4.3 and 4.4 indicate. According to these figures, there are irreducible error floors, even when fading is static. The level of the error floor varies with the phase offset Δ. Through trial and error, a $\Delta = \dfrac{\pi}{3}$ is found to be the best as it yields the lowest BERs. The results in Figs 4.3 and 4.4 also indicate that conventional differential detection (K=2) does not appear to work at all for M=4 DPSK in a TWR setting.

Finally, Figs 4.5 and 4.6 show the comparison between the proposed DFB receiver for 4-ary orthogonal modulations and the DFB-MSDD for DQPSK with static fading ($f_d T = 0$) and time-selective fading ($f_d T = 0.005$). In the DQPSK case, the phase offset between two user's QPSK constellations is set to $\Delta = \dfrac{\pi}{3}$, and DFB-MSDD of sizes $K = 3$ and $K = 4$ with both ideal and actual feedback are considered. Compared to the corresponding *M=2* results in Figs 4.1 and 4.2, the performance of the proposed DFB receiver for orthogonal modulations improves when *M* increases from 2 to 4. As a matter of fact, the performance of the DFB receiver almost coincides with that of coherent QPSK. In contrast, DFB-MSDD of DPSK experiences performance degradation

as M increases. Note that when the fade rate increase from 0 to 0.005, the performance of the DFB-MSDD for DQPSK deteriorates dramatically while the proposed orthogonal modulation scheme is able to maintain its performance. To elaborate, in the static fading case and at a BER of 10^{-3}, there is a huge 8 dB gap between DQPSK and the proposed 4-ary orthogonal modulation system. Even with ideal feedback, $K = 4$ DFB-MSDD is 3 dB worse than the proposed orthogonal modulation system. When the fade rate increases to $f_d T = 0.005$, the BER curves of DFB-MSDD depict clear irreducible error floors and the performance gap between orthogonal modulation and DPSK increases further from the static fading case. The proposed $M = 4$ orthogonal modulation system, on the other hand, is able to maintain its performance when the fade rate increases.

Fig. 4.1: Comparison with 2P-TWR system employing DPSK and DFB-MSDD at the relay; constellation size: $M = 2$, phase offset between user A's and B's constellation: $\Delta = 0$, Doppler frequency : $f_d T = 0$.

Fig. 4.2: Comparison with 2P-TWR system employing DPSK and DFB-MSDD at the relay; constellation size: $M = 2$, phase offset between user A's and B's constellation: $\Delta = 0$, Doppler frequency : $f_d T = 0.005$.

Fig. 4.3: Performance of DFB-MSDD at the relay with different observation intervals and different phase offsets. Constellation size: $M = 4$, Doppler frequency : $f_d T = 0$.

Fig. 4.4: Performance of DFB-MSDD at the relay with different observation intervals and different phase offsets. Constellation size: $M = 4$, Doppler frequency : $f_d T = 0.005$.
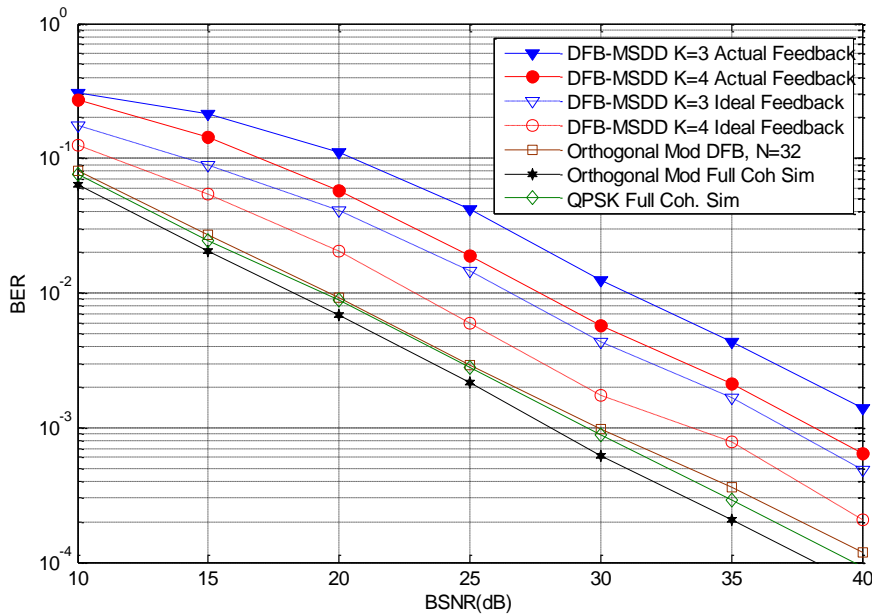
Fig. 4.5: Comparison with 2P-TWR system employing DPSK and DFB-MSDD at the relay; constellation size: $M = 4$, phase offset between user A's and B's constellation: $\Delta = \pi / 3$, Doppler frequency : $f_d T = 0$.
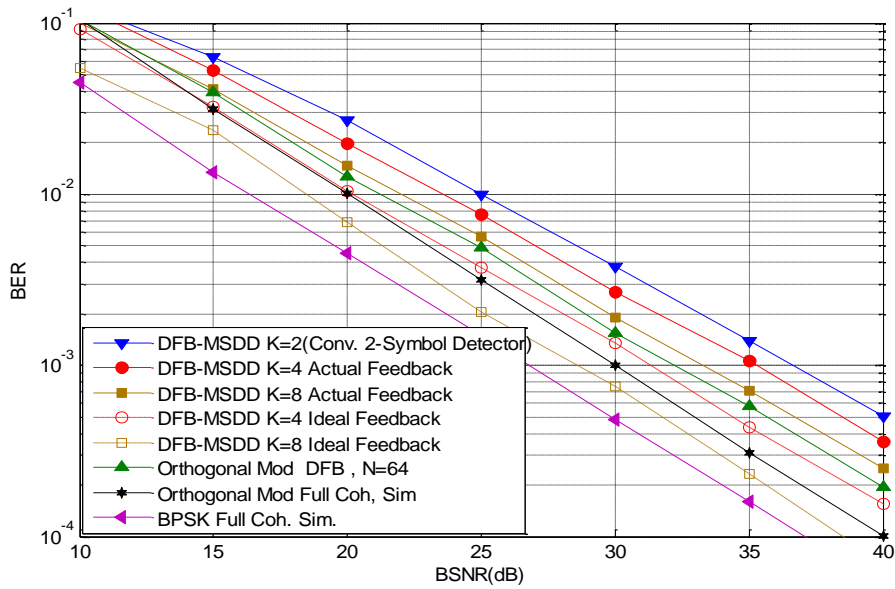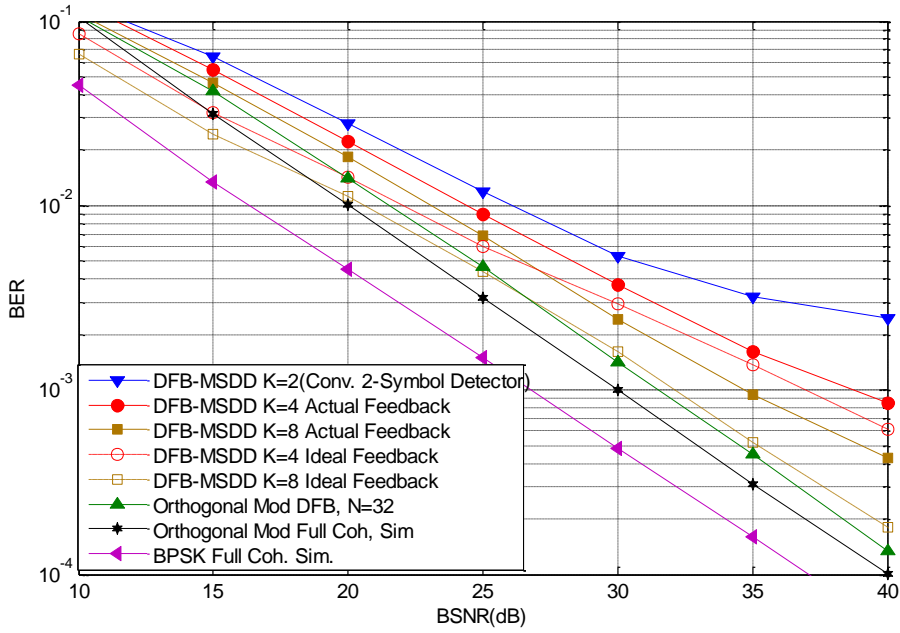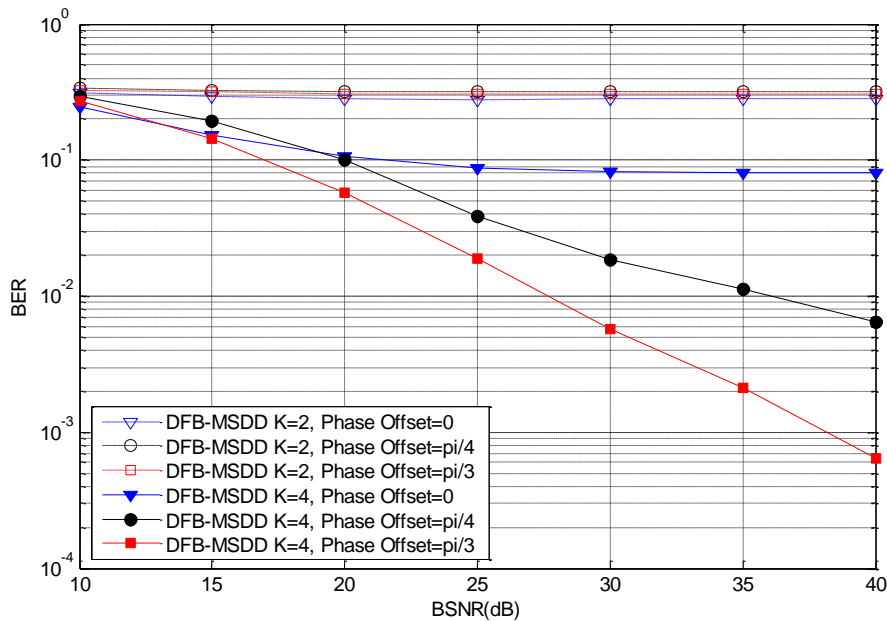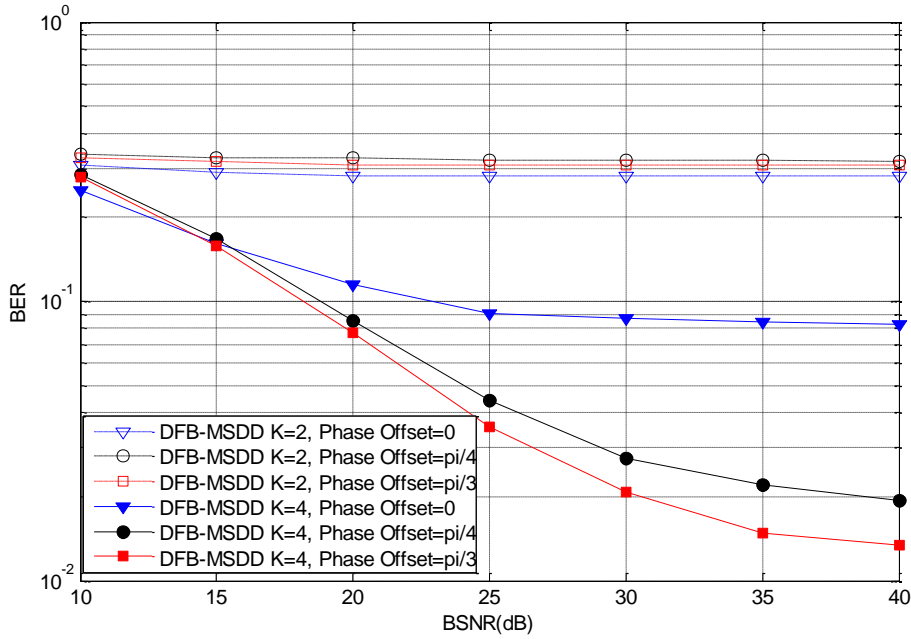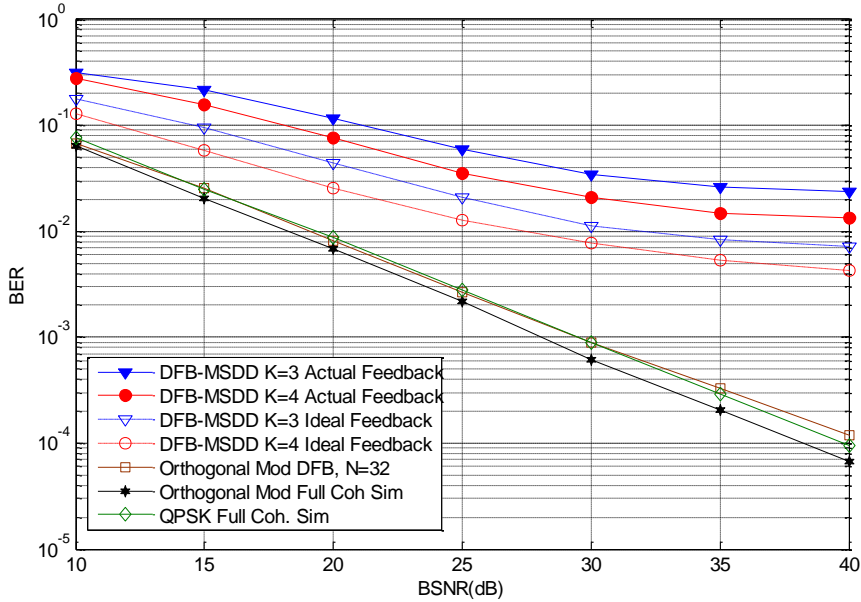
Fig. 4.6: Comparison with 2P-TWR system employing DPSK and DFB-MSDD at the relay; constellation size: $M = 4$, phase offset between user A's and B's constellation: $\Delta = \pi / 3$, Doppler frequency : $f_d T = 0.005$.

While BER is one metric that we can use to compare orthogonal modulations and PSK, another important metric is the spectral efficiency. Both binary and quaternary orthogonal modulations have a raw efficiency of 0.5 bit of information per signal dimension. This is half that of BPSK and QPSK. As a result, the proposed orthogonal modulation systems have roughly half the raw spectral efficiency as their PSK counterparts. However, if we look at the two modulation approaches from a combined coding and modulation perspective, the story on the effective spectral efficiency can be quite different. Consider the M=4 case in Fig. 4.5 where we found that the proposed 4-ary orthogonal modulation system is 8 dB more power efficient than QPSK. One simple way for the QPSK system to make up for this 8 dB gap is to repeat its symbols 6 times, where $10\log_{10} 6 = 8$. This will, however, end up with a combined coding-modulation system with a higher transmission bandwidth than the uncoded 4FSK system. Of course in practice it is not wise to use a repetition code. So suppose we use a rate $R = 1/2$ convolutional code in the QPSK system so that after coding, the QPSK system has the

same power efficiency and more or less the same bandwidth as the uncoded 4FSK system. This requires the use of a code with a free Hamming distance d that satisfies $10\log_{10}(R \times d) = 8$, or $d = 12$. The best rate $R = 1/2$ code having a $d = 12$ is the one having a constraint length of $K = 9$ [23, Table 8.3-1]. A Viterbi decoder for this code has 256 states, which is lots more complicated that our uncoded system. Therefore, although 2/4-FSK has twice the number of signal dimensions per information bit than 2/4-PSK, hence a higher transmission bandwidth at the modulation level, it may still end up having a higher spectral efficiency than PSK if we consider the throughput of a combined coding and modulation system.

4.3. Conclusion

In order to put the performance of the proposed DFB receiver for orthogonal modulations into proper perspective, we compare it against the DFB-MSDD for DPSK in the literature. This reference scheme also employs decision feedback and does not require the transmission of pilot symbols. The BER performance of the DFB-MSDD is simulated and compared against that of the proposed orthogonal modulation system for different combinations of modulation size M, observation interval K, and fade rate f_dT. It is observed that the proposed DFB receiver for orthogonal modulations perform substantially better than DFB-MSDD for DPSK. This is especially true in 4-ary systems where the proposed orthogonal modulation system enjoys a huge 8 dB advantage over DPSK in terms of power efficiency. While one would argue that this is achieved at the expenses of a higher transmission bandwidth requirement and hence a lower spectral efficiency, this is true only if we look at the system at the modulation level. If the spectrum efficiency at the combined coding and modulation level is considered instead, it is highly likely that the proposed orthogonal modulation and demodulation technique can actually lead to a more spectrally efficient system, owing to this huge 8 dB "head start". We also found that DPSK is extremely sensitive to a Doppler shift, while the proposed orthogonal modulation technique is very robust in the presence of time-selective fading.

Chapter 5.

Conclusion and Future Works

5.1. Conclusion

A novel decision feedback (DFB) detector is proposed for the relay of a two-phase (2P) two-way relay (TWR) communication system that employs pilot-less orthogonal modulation in the uplink and physical-layer network coding (PNC) over finite field in the downlink. Through extensive simulation, it is found that the newly proposed relay receiver is able to attain a performance very close to that of a full-coherent detector in the presence of static or time-selective Rayleigh fading and additive white Gaussian noise in the uplink. It also significantly outperforms its differential detection counterpart for differential PSK.

The thesis research began with a literature survey on TWR with PNC. It was observed that the majority of the works focus on PSK systems. Few of them studied orthogonal modulations, such as FSK and CPFSK. From a combined modulation and multiple access prospective, orthogonal modulations appear to be more suitable for TWR with PNC. This is the motivation behind the thesis research. We focus on pilot-less transmission as it is a more challenging problem than simply assuming ideal coherent detection.

In observing that the sum of correlators' output provides a noisy copy of the sum fading gain, irrespective of the symbols transmitted, a novel partial-coherent detector is proposed in Chapter 2. Upperbound on the bit-error-rate (BER) is derived for this detector and it is found that it can provide a 3 dB increase in power efficiency over

standard non-coherent detection, even when no pilot is transmitted. Simulation results validate the analytical approximation.

Although the partial-coherent detector in Chapter 2 enjoys a substantial gain in performance over the non-coherent detector, it still suffers a 7 dB degradation in SNR when compared to the ideal full-coherent detector. This motivates us to propose the DFB in Chapter 3. This receiver performs decision-aided channel estimation by exploiting the property that if the uplink symbols transmitted by the two users are different, then the individual fading gains affecting their symbols can be separated and tracked. The fading estimates obtained this way can then be used in a coherent detector to improve the reliability of the detected data at the relay. Simulation results indicate that with as little as one feedback attempt, the proposed DFB receiver gain a 6dB improvement in SNR over the partial-coherent detector from Chapter 2, i.e. a performance that is within 1 dB of ideal full-coherent detection.

Given that the motivation to study orthogonal modulations is that it seems more compatible with the multiple access nature of TWR with PNC, we verify this intuition by comparing it against differential PSK with decision-feedback (DFB) multiple-symbol differential detection (MSDD), in Chapter 4. Through extensive simulations, we found out the proposed DFB receiver for binary and quaternary orthogonal modulations are 1 dB and 8 dB more efficient than its DBPSK and DQPSK counterparts in static fading channels. The performance gaps widened in the presence of time-selective fading.

Finally, from the implementation perspective, the proposed receiver, with minimum mean-square error (MMSE) channel interpolation, has acceptable complexity as long as the processing block size is not too large. A substantial reduction in implementation complexity is possible through the use of polynomial interpolators instead of MMSE, at the expense of a modest lost in performance.

In conclusion, the proposed DFB for pilot-less orthogonal modulations in TWR with PNC and fading has a lot of potential. Its performance is superior to pilot-less DPSK and

the implementation complexity is acceptable. While it is less spectrally efficient at the modulation level, when combined coding and modulation is considered, orthogonal modulation may actually enjoy a higher spectral efficiency, as its superior power efficiency mean much less coding redundancy is needed.

5.2. Contributions

This dissertation is concerned with a research topic where only limited work has been performed to date. The research embodies the following major contributions:

1. We propose a partial-coherent detector for pilot-less orthogonal modulations in TWR with PNC that is 3 dB power efficient than non-coherent detection.
2. We derive the BER of the partial-coherent detector, which is by no means trivial.
3. We demonstrate how decision feedback should be performaned in pilot-less orthogonal modulation systems in order to achieve a performance close to ideal full-coherent detection.
4. We present not only results for static fading channels, but also results on time-selective fading channels. The latter scenario has largely been ignored in the literature.
5. We show that in the absence of pilot, orthogonal modulations perform substantially better than differential PSK. The difference is 1 dB in the binary case, and 8 dB in the quaternary case, and the gaps increase with time-selective fading.

5.3. Future works

Because of time limitation, this research focuses on the time-selective Rayleigh fading environment. However, we believe that the proposed decision feedback methodology can also be employed in systems operating in a dense multipath environment, such as some variants of the ultra-wideband systems considered in [28]-[29].

A limitation of the proposed DFB receiver is that it is only able to maintain a performance close to ideal coherent detection if the Doppler frequency is no larger than 0.5% the symbol rate. While this is sufficient for most situations, it would be interesting to see what modifications to the existing channel sorting/tracking techniques are required in order to handle faster fading.

References

[1] R. Pabst, B. H. Walke, D. C. Schultz, P. Herhold, H. Yanikomeroglu, S. Mukherjee, H. Viswanathan, M. Lott, W. Zirwas, M. Dohler, H. Aghvami, D. D. Falconer, and G. P. Fettweis, "Relay-based deployment concepts for wireless and mobile broadband radio," *IEEE Commun. Mag.*, vol. 42, no. 9, pp. 80-89, Sep. 2004

[2] R. Nabar, H. Bolcskei, and F. Kneubuhler, "Fading relay channels: performance limits and space-time signal design," IEEE Journal on Selected Areas in Communications, vol. 22, no. 6, pp. 1099-1109, Aug. 2004.

[3] A. Nosratinia, T. Hunter, and A. Hedayat, "Cooperative communication in wireless networks," IEEE Communications Magazine, vol. 42, no. 10, pp. 74-80, Oct. 2004.

[4] J. Laneman, D. Tse, and G. Wornell, "Cooperative diversity in wireless networks: E_cient protocols and outage behavior," IEEE Transactions on Information Theory, vol. 50, no. 12, pp. 3062-3080, Dec. 2004.

[5] L. Xiao, T. Fuja, and J. Costello, D.J., "Mobile relaying: Coverage extension and throughput enhancement," IEEE Transactions on Communications, vol. 58, no. 9, pp. 2709-2717, September 2010. 1

[6] B. Rankov and A. Wittneben, "Achievable rate regions for the two-way relay channel," in *Proc. Int. Symp. Inf. Theory*, pp. 1668-1672, July 2006

[7] S.Liew, S. Zhang, L. Lu,"Physical Layer Network Coding: tutorial, Survey, and Beyond," Physical Communication Volume 6, pp 4-42, March 2013

[8] Y. Wu, P. A. Chou, and S. Y. Kung, "Information Exchange in Wireless Networks with Network Coding and Physical Layer Broadcast," *Proc. 39th Annual Conf. Inform. Sci. and Systems (CISS)*, 2005

[9] C. Fragouli, J. Y. Boudec, J. Widmer, "Network Coding: An Instant Primer," *ACM SIGCOMM Computer Communication Review*, pp. 63-68, vol. 36, no. 1, Jan. 2006.

[10] P. Popovski and H. Yomo, "The anti-packets can increase the achievable throughput of a wireless multi-hop network," in *Proc.IEEE International Conference on Communication*, pp. 3885-3890, June 2006.

[11] S. Zhang, S. Liew, and P. Lam, "Physical layer network coding," ACM Mobicom2006, 2006

[12]S. Katti, S. Gollakota, and D. Katabi, "Embracing wireless interference: analog network coding," in *Proc. ACM SIGCOMM*, pp. 397-408, Aug. 2007.

[13] S. Zhang, S. C. Liew, and L. Lu, "Physical layer network coding schemes over finite and infinite fields," in *Proc. IEEE Global Telecommun. Conf.*, pp. 1-6, Dec. 2008.

[14] F. Gao, R. Zhang, and Y.-C. Liang, "Optimal channel estimation and training design for two-way relay networks," *IEEE Trans. Commun.*, vol. 57, NO. 10, pp. 3024-3033, October 2009.

[15] B. Jiang, F. Gao, X. Gao, and A. Nallanathan, "Channel estimation and training design for two-way relay networks with power allocation," *IEEE Trans.Wireless Commun.*, vol. 9, NO. 6, pp. 2022-2032, June 2010.

[16] T. Cui, F. Gao, and C. Tellambura, "Differential modulation for two-way wireless communications: a perspective of differential network coding at the physical layer," *IEEE Trans.Commun.*, vol. 57, NO. 10, pp. 2977-2987, October 2009.

[17] L. Song, Y. Li, A. Huang, B. Jiao, and A.V. Vasilakos, "Differential modulation for bidirectional relaying with analog network coding," *IEEE Trans. Signal Process.*, vol. 58, NO. 7, pp. 3933-3938, July 2010.

[18] W. Guan and K. J. R. Liu, "Performance analysis of two-Way relaying with non-coherent differential modulation," *IEEE Trans. Wireless Commun.*, vol. 10, no. 6, pp. 2004-2014, Jun 2011

[19] S. Abdallah and I. N. Psaromiligkos, "Partially-blind estimation of reciprocal channels for AF two-way relay networks employing *M*-PSK modulation," *IEEE Trans. Wireless Commun.*, vol. 11, no. 5, pp. 1649-1654, May 2012.

[20] S. Abdallah and I. N. Psaromiligkos, "Blind channel estimation for amplify-and-forward two-way relay networks employing M–PSK modulation," *IEEE Trans. Signal Process,* vol. 60, no. 7, pp. 3604-3615, July 2012.

[21] L. Li, Y. Ding, J. K. Zhang, and R. Zhang, "Blind detection with unique identification in two-way relay channel," *IEEE Trans.Wireless Commun.*, vol. 11, no. 7, pp. 2640-2648, July 2012.

[22] J. Sørensen, R. Krigslund, P. Popovski, T. Akino, and T. Larsen, "Physical layer network coding for FSK systems," *IEEE Commun. Lett.*, vol. 13, no. 8, pp. 597-599, Aug. 2009.

[23] M. C. Valenti, D. Torrieri, and T. Ferrett, *"*Noncoherent physical-layer network coding with FSK nodulation: relay receiver design issues," *IEEE Trans. Commun.*, vol. 59, No. 9, pp. 2595-2604, Sep. 2011.

[24] J.G. Proakis, *Digital Communications*, 4th ed., McGraw Hill, New York, 2011, pp. 713

[25] P. Ho, Z. Songhua, and P. Y. Kam, "Space-time FSK: an Implicit Pilot Symbol Assisted Modulation Scheme," *IEEE Trans. Wireless Commun.*, vol. 6, pp. 2602–2611, July 2007.

[26] M. Schwartz, W.R. Bennett, S. Stein, *Communication Systems and Techniques*, Wiley-IEEE Press, 1996, pp. 590-595.

[27] R. Schober, W. Gerstacker, and J. Huber, "Decision-feedback differential detection of MDPSK for flat Rayleighfading channels," *IEEE Trans. Commun.*, vol. 47, no. 7, pp. 1025–1035, Jul. 1999

[28] H. Gao, X. Su, T. Lv, T. Wang, Z. Wang, "Physical-Layer Network Coding Aided Two-Way Relay for Transmitted-Reference UWB Networks," in *Proc., IEEE Global Telecommun. Conf.*, Houston, Texas, USA, Dec. 2011.

[29] Z. Wang; T. Lv; H. Gao; Y. Li, "A Novel Two-Way Relay UWB Network with Joint Non-Coherent Detection in Multipath," *in Proc., IEEE Vehicular Technology Conference Spring*, Budapest, Hungary, May 2011

Appendix A.

Pair-wise Error Probability Analysis

As mentioned in Chapter 2, there are six types of pairwise error events for each of the non-coherent, full-coherent, and partial-coherent detectors. Type I and Type III error events are valid for both the binary (*M*=2) and quaternary (*M*=4) cases, while the others are only valid for the quaternary case. Also stated in in (2.25) is that each type of pair-wise error events of the three detectors can be expressed in terms of a quadratic form $D = \mathbf{X}^\dagger \mathbf{M} \mathbf{X}$ of complex Gaussian random variables $\mathbf{X}$ being less/greater than a non-negative threshold T_0, where $\mathbf{M}$ and T_0 vary with the detector and error event types. The probabilities of different types of pair-wise error events of the proposed partial-coherent detector will be illustrated in this section and those of the full-coherent detector and the non-coherent detector can be calculated in the similar way.

In the following discussion, (s_A, s_B) denotes the transmitted symbol pair from the two users and $(\tilde{s}_A, \tilde{s}_B)$ an alternative. Without loss of generality, (s_A, s_B) and $(\tilde{s}_A, \tilde{s}_B)$ are set to some representative values, as all error events of the same type can be obtained from the representative case through a relabeling of the correlators (i.e. a permutation). Furthermore the vector $\mathbf{X}$ in the quadratic form is defined as

$$\mathbf{X} = [r_0, r_1, r_2, g_A, g_B]^T, \tag{A.1}$$

where r_0, r_1, r_2 are the the output of the first three correlators [2], and g_A and g_B are the uplink gains.

---

[2] In the binary case, there are only two correlators. As such, r_2 is disabled by forcing the third row and third column of the $\mathbf{M}$ matrix to zero.

Type I error: the same symbols are transmitted, but the alternative $(\tilde{s}_A, \tilde{s}_B)$ differ from (s_A, s_B) in one position

This case can be defined by setting $s_A = s_B = 0$, and $\tilde{s}_A = 0$, $\tilde{s}_B = 1$. A Type I pairwise error event is said to have occurred when $p(\mathbf{r}\,|\,s_A = 0,\ s_B = 0,\ u) < p(\mathbf{r}\,|\,\tilde{s}_A = 0,\ \tilde{s}_B = 1,\ u)$. Given that the components of the received vector $\mathbf{r} = (r_0, r_1, ... r_{M-1})^T$ are $r_0 = u + n_0$ and $r_i = n_i$, $i = 1, 2, ... M - 1$, where $u = g_A + g_B$, this event for both the binary (M=2) and quaternary (M=4) is equivalent to the quadratic form $D_1 = \mathbf{X}^\dagger \mathbf{M}_1 \mathbf{X}$ being greater than

$$T_0 = \ln(1 + \gamma_s),\tag{A.2}$$

where $\gamma_s = \sigma_g^2 / N_0$ (symbol SNR),

$$\mathbf{M}_1 = \frac{1}{N_0}\begin{bmatrix} \dfrac{\gamma_s}{4(\gamma_s+1)} & -\dfrac{\gamma_s}{4(\gamma_s+1)} & 0 & -\dfrac{1}{2} & -\dfrac{1}{2} \\[2mm] -\dfrac{\gamma_s}{4(\gamma_s+1)} & \dfrac{\gamma_s}{4(\gamma_s+1)} & 0 & \dfrac{1}{4} & \dfrac{1}{4} \\[2mm] 0 & 0 & 0 & 0 & 0 \\[2mm] -\dfrac{\gamma_s}{4(\gamma_s+1)} & \dfrac{1}{4} & 0 & \dfrac{\gamma_s}{4(\gamma_s+1)} & \dfrac{\gamma_s}{4(\gamma_s+1)} \\[2mm] \dfrac{\gamma_s}{4(\gamma_s+1)} & \dfrac{1}{4} & 0 & \dfrac{\gamma_s}{4(\gamma_s+1)} & \dfrac{\gamma_s}{4(\gamma_s+1)} \end{bmatrix},\tag{A.3}$$

and

$$\boldsymbol{\Phi}_{\mathbf{xx}} = \frac{1}{2} E\left[\mathbf{XX}^{\dagger}\right] = \begin{cases} N_0 \begin{bmatrix} 2\gamma_s+1 & 0 & 0 & \gamma_s & \gamma_s \\ 0 & 1 & 0 & 0 & 0 \\ 0 & 0 & 0 & 0 & 0 \\ \gamma_s & 0 & 0 & \gamma_s & 0 \\ \gamma_s & 0 & 0 & 0 & \gamma_s \end{bmatrix}, & M = 2, \\[2em] N_0 \begin{bmatrix} 2\gamma_s+1 & 0 & 0 & \gamma_s & \gamma_s \\ 0 & 1 & 0 & 0 & 0 \\ 0 & 0 & 1 & 0 & 0 \\ \gamma_s & 0 & 0 & \gamma_s & 0 \\ \gamma_s & 0 & 0 & 0 & \gamma_s \end{bmatrix}, & M = 4, \end{cases} \quad \text{(Type I)}$$

(A.4)

is the covariance matrix of the vector $\mathbf{X}$ in (A.1).

According to (2.29), the characteristic function of D_1, $\Phi_{D_1}(s)$, is the root of the determinant

$$\lambda(s) = \left\| \mathbf{I}_5 + 2s\boldsymbol{\Phi}_{\mathbf{xx}}\mathbf{M}_1 \right\|, \tag{A.5}$$

where $\mathbf{I}_5$ is a 5x5 identity matrix. Using symbolic computation, we found that the roots of $\lambda(\mathbf{s})$ are

$$p_1 = +\sqrt{1+\gamma^{-1}}, \quad p_2 = -\sqrt{1+\gamma^{-1}}. \qquad \text{(Type I)} \tag{A.6}$$

Substituting (A.6) into (2.26) and (2.27), the probability that a Type I event occurs in both the binary and quaternary case is

$$P_I = \Pr[D_1 \geq T_0] = -\sum_{LHP\ poles} res\left[\frac{\Phi_{D_1}(s)e^{sT_0}}{s}\right]$$

$$= -\frac{p_1 p_2 e^{sT_0}}{s(s-p_1)}\Big|_{s=p_2}$$

$$= \frac{1}{2}(1+\gamma)^{-\sqrt{1+\gamma^{-1}}}$$ (A.7)

$$\approx \frac{1}{2\gamma}(\sqrt{\gamma})^{-1/\gamma} \quad \text{when } \gamma \to \infty,$$

where the last term is the large SNR approximation. Since the term $\left(\sqrt{\gamma_s}\right)^{-1/\gamma_s} \to 1$ as $\gamma_s \to \infty$, this means the above error event probability approaches $\dfrac{1}{2\gamma_s}$.

Type II error: same symbols are transmitted, but the alternative ($\tilde{s}_A, \tilde{s}_B$) differ from (s_A, s_B) in both positions

This case can be defined by setting $s_A = s_B = 0$, $\tilde{s}_A = 1$ and $\tilde{s}_B = 2$. The error event $p(\mathbf{r}\,|\,s_A = 0,\ s_B = 0,\ u) < p(\mathbf{r}\,|\,\tilde{s}_A = 1,\ \tilde{s}_B = 2,\ u)$ is equivalent to the quadratic form $D_2 = \mathbf{X}^\dagger \mathbf{M}_2 \mathbf{X}$ being greater than the threshold T_0 in (A.2), where

$$\mathbf{M}_2 = \frac{1}{N_0}\begin{bmatrix} 0 & 0 & 0 & -\dfrac{1}{2} & -\dfrac{1}{2} \\[2mm] 0 & \dfrac{\gamma_s}{4(\gamma_s+1)} & -\dfrac{\gamma_s}{4(\gamma_s+1)} & \dfrac{1}{4} & \dfrac{1}{4} \\[2mm] 0 & -\dfrac{\gamma_s}{4(\gamma_s+1)} & \dfrac{\gamma_s}{4(\gamma_s+1)} & \dfrac{1}{4} & \dfrac{1}{4} \\[2mm] -\dfrac{1}{2} & \dfrac{1}{4} & \dfrac{1}{4} & \dfrac{1}{4} & \dfrac{1}{4} \\[2mm] -\dfrac{1}{2} & \dfrac{1}{4} & \dfrac{1}{4} & \dfrac{1}{4} & \dfrac{1}{4} \end{bmatrix},$$ (A.8)

and $\boldsymbol{\Phi}_{XX}$, the covariance matrix of $\mathbf{X}$, is the same as that in (A.4). Through symbolic computation, it can showed that the poles of $\Phi_{D_2}(s)$, the CF of D_2, are

$$p_1 = -\frac{1}{2} + \frac{1}{2}\sqrt{1 + \frac{4}{3}\gamma_s^{-1}},$$

$$p_2 = -\frac{1}{2} - \frac{1}{2}\sqrt{1 + \frac{4}{3}\gamma_s^{-1}}, \qquad \text{(Type II)} \qquad \text{(A.9)}$$

$$p_3 = -1 - \gamma_s^{-1}$$

Therefore,

$$P_{II} = \Pr\left[D_2 > T_0\right] = -\sum_{LHP\ poles} res\left[\frac{\Phi_{D_3}(s)e^{sT_0}}{s}\right]$$

$$= \frac{p_1 p_3}{(p_2 - p_1)(p_2 - p_3)}e^{p_2 T_0} + \frac{p_1 p_2}{(p_3 - p_1)(p_3 - p_2)}e^{p_3 T_0}$$

$$= \frac{1}{2}\left(1 - \frac{1}{\sqrt{1 + \frac{4}{3}\gamma_s^{-1}}}\right) \frac{\left(1 + \gamma_s^{-1}\right)}{\left(\frac{1}{2} + \gamma_s^{-1}\right) - \frac{1}{2}\sqrt{1 + \frac{4}{3}\gamma_s^{-1}}}(1 + \gamma_s)^{-\frac{1}{2} - \frac{1}{2}\sqrt{1 + \frac{4}{3}\gamma_s^{-1}}} - \frac{1}{3\left(\frac{2}{3} + \gamma_s^{-1}\right)}(1 + \gamma_s)^{-1 - \gamma_s^{-1}}$$

$$\approx \frac{1}{2}\gamma_s^{-1} \quad when\ \gamma_s \to \infty$$

(A.10)

Type III error: different symbols are transmitted but the alternative $\tilde{s}_A$ and $\tilde{s}_B$ are the same, and $(\tilde{s}_A, \tilde{s}_B)$ differ from (s_A, s_B) in one position

This case can be defined by $s_A = 0$ and $s_B = 1$, and $\tilde{s}_A = \tilde{s}_B = 0$. When the pair $s_A = 0$ and $s_B = 1$ was sent (i.e. a sum bit of $c = 1$), the event that $p(\mathbf{r} \mid s_A = 0,\ s_B = 1,\ u) < p(\mathbf{r} \mid \tilde{s}_A = 0,\ \tilde{s}_B = 0,\ u)$ is equivalent to the quadratic form $D_3 = \mathbf{X}^\dagger \mathbf{M}_3 \mathbf{X}$ being smaller than the threshold T_0 in (A.2), where

$$\mathbf{M}_3 = \frac{1}{N_0} \begin{bmatrix} \dfrac{\gamma_s}{4(\gamma_s+1)} & -\dfrac{\gamma_s}{4(\gamma_s+1)} & 0 & -\dfrac{1}{2} & -\dfrac{1}{2} \\[2ex] -\dfrac{\gamma_s}{4(\gamma_s+1)} & \dfrac{\gamma_s}{4(\gamma_s+1)} & 0 & \dfrac{1}{4} & \dfrac{1}{4} \\[2ex] 0 & 0 & 0 & 0 & 0 \\[2ex] -\dfrac{\gamma_s}{4(\gamma_s+1)} & \dfrac{1}{4} & 0 & \dfrac{\gamma_s}{4(\gamma_s+1)} & \dfrac{\gamma_s}{4(\gamma_s+1)} \\[2ex] \dfrac{\gamma_s}{4(\gamma_s+1)} & \dfrac{1}{4} & 0 & \dfrac{\gamma_s}{4(\gamma_s+1)} & \dfrac{\gamma_s}{4(\gamma_s+1)} \end{bmatrix}. \tag{A.11}$$

In this case, the covariance matrix of $\mathbf{X}$ is changed to be

$$\boldsymbol{\Phi}_{\mathbf{XX}} = \frac{1}{2} E\left[\mathbf{X}\mathbf{X}^\dagger\right] = \begin{cases} N_0 \begin{bmatrix} \gamma_s+1 & 0 & 0 & \gamma_s & 0 \\ 0 & \gamma_s+1 & 0 & 0 & \gamma_s \\ 0 & 0 & 0 & 0 & 0 \\ \gamma_s & 0 & 0 & \gamma_s & 0 \\ 0 & \gamma_s & 0 & 0 & \gamma_s \end{bmatrix}, & M=2, \\[8ex] N_0 \begin{bmatrix} \gamma_s+1 & 0 & 0 & \gamma_s & 0 \\ 0 & \gamma_s+1 & 0 & 0 & \gamma_s \\ 0 & 0 & 1 & 0 & 0 \\ \gamma_s & 0 & 0 & \gamma_s & 0 \\ 0 & \gamma_s & 0 & 0 & \gamma_s \end{bmatrix}, & M=4, \end{cases} \quad \text{(Type III)}$$

$$\tag{A.12}$$

Again, through symbolic computation, we can show that $\Phi_{D_3}(s)$, the characteristic function of D_3, has only two poles:

$$q_1 = 1 + \sqrt{1+\gamma_s^{-1}}, \quad q_2 = 1 - \sqrt{1+\gamma_s^{-1}}. \qquad \text{(Type III)} \tag{A.13}$$

As such, the structure of the probability for a Type III error event is identical to that shown in (2.28), except that the p_i's in that equation is now replaced by the q_i's shown

above. After substituting the roots into (2.27), the probability, P_{III}, for a Type III error event is

$$
\begin{aligned}
P_{III} = \Pr\left[D_3 \leq T_0\right] &= \sum_{s=0 \text{ and all } LHP \text{ poles}} res\left[\frac{\Phi_{D_2}(s)e^{sT_0}}{s}\right] \\
&= \left(\frac{q_1 q_2 e^{sT_0}}{(s-q_1)(s-q_2)}\bigg|_{s=0} + \frac{q_1 q_2 e^{sT_0}}{s(s-q_1)}\bigg|_{s=q_2}\right) \\
&= 1 - \frac{\left(1+\sqrt{1+\gamma_s^{-1}}\right)}{2\sqrt{1+\gamma_s^{-1}}}(1+\gamma_s)^{\left(1-\sqrt{1+\gamma_s^{-1}}\right)} \\
&\approx 1 - \left(\sqrt{\gamma_s}\right)^{-1/\gamma_s} \text{ when } \gamma \to \infty
\end{aligned}
\tag{A.14}
$$

Type IV error: different symbols are transmitted, but the alternative $\tilde{s}_A, \tilde{s}_B$ are identical and $(\tilde{s}_A, \tilde{s}_B)$ differ from (s_A, s_B) in both positions

This case can be defined by setting $s_A = 0$, $s_B = 1$, and $\tilde{s}_A = \tilde{s}_B = 2$. A Type IV error event $p(\mathbf{r} \mid s_A = 0, s_B = 1, u) < p(\mathbf{r} \mid \tilde{s}_A = 2, \tilde{s}_B = 2, u)$ is equivalent to the quadratic form $D_4 = \mathbf{X}^\dagger \mathbf{M}_4 \mathbf{X}$ being smaller than the threshold T_0 in (A.2), where

$$
\mathbf{M}_4 = \frac{1}{N_0}
\begin{bmatrix}
\dfrac{\gamma_s}{4(\gamma_s+1)} & -\dfrac{\gamma_s}{4(\gamma_s+1)} & 0 & \dfrac{1}{4} & \dfrac{1}{4} \\[3mm]
-\dfrac{\gamma_s}{4(\gamma_s+1)} & \dfrac{\gamma_s}{4(\gamma_s+1)} & 0 & \dfrac{1}{4} & \dfrac{1}{4} \\[3mm]
0 & 0 & 0 & -\dfrac{1}{2} & -\dfrac{1}{2} \\[3mm]
\dfrac{1}{4} & \dfrac{1}{4} & -\dfrac{1}{2} & \dfrac{\gamma_s}{4(\gamma_s+1)} & \dfrac{\gamma_s}{4(\gamma_s+1)} \\[3mm]
\dfrac{1}{4} & \dfrac{1}{4} & -\dfrac{1}{2} & \dfrac{\gamma_s}{4(\gamma_s+1)} & \dfrac{\gamma_s}{4(\gamma_s+1)}
\end{bmatrix}
\tag{A.15}
$$

and the covariance matrix of the vector $\mathbf{X}$ is the same one given in (A.10). The poles of $\Phi_{D_4}(s)$, the CF of D_4, are

90

$$p_1 = \frac{1}{2} + \frac{1}{2}\sqrt{1 + \frac{4}{3}\gamma_s^{-1}},$$

$$p_2 = \frac{1}{2} - \frac{1}{2}\sqrt{1 + \frac{4}{3}\gamma_s^{-1}}, \qquad \text{(Type IV)} \qquad \text{(A.16)}$$

$$p_3 = -\gamma_s^{-1},$$

Therefore,

$$P_{IV} = \Pr[D_4 \le T_0] =$$

$$= 1 - \frac{1}{2}\left(1 + \frac{1}{\sqrt{1 + \frac{4}{3}\gamma_s^{-1}}}\right) \frac{\gamma_s^{-1}}{\left(\frac{1}{2} + \gamma_s^{-1}\right) - \frac{1}{2}\sqrt{1 + \frac{4}{3}\gamma_s^{-1}}} (1 + \gamma_s)^{\frac{1}{2} - \frac{1}{2}\sqrt{1 + \frac{4}{3}\gamma_s^{-1}}} + \frac{1}{3\left(\frac{2}{3} + \gamma_s^{-1}\right)} (1 + \gamma_s)^{-\gamma_s^{-1}}$$

$$\approx 1 - \frac{3}{2}\gamma_s^{-1/(3\gamma_s)} + \frac{1}{2}\gamma_s^{-1/\gamma_s} \quad \text{when } \gamma_s \to \infty$$

$$\text{(A.17)}$$

Type V error: symbols in both the transmitted and alternative pairs are different, but ($\tilde{s}_A$, $\tilde{s}_B$) only differ from (s_A, s_B) in one position

This case can be defined by setting $s_A = 0$, $s_B = 1$, and $\tilde{s}_A = 0, \tilde{s}_B = 2$. The Type V error event $p(\mathbf{r} | s_A = 0,\ s_B = 1,\ u) < p(\mathbf{r} | \tilde{s}_A = 0,\ \tilde{s}_B = 2,\ u)$ is equivalent to the quadratic form $D_5 = \mathbf{X}^\dagger \mathbf{M}_5 \mathbf{X}$ being smaller than the threshold $T_0 = 0$ where

$$\mathbf{M}_5 = \frac{1}{N_0}\begin{bmatrix} 0 & -\frac{\gamma_s}{4(\gamma_s+1)} & \frac{\gamma_s}{4(\gamma_s+1)} & 0 & 0 \\ -\frac{\gamma_s}{4(\gamma_s+1)} & \frac{\gamma_s}{4(\gamma_s+1)} & 0 & \frac{1}{4} & \frac{1}{4} \\ \frac{\gamma_s}{4(\gamma_s+1)} & 0 & -\frac{\gamma_s}{4(\gamma_s+1)} & -\frac{1}{4} & -\frac{1}{4} \\ 0 & \frac{1}{4} & -\frac{1}{4} & 0 & 0 \\ 0 & \frac{1}{4} & -\frac{1}{4} & 0 & 0 \end{bmatrix} \qquad \text{(A.18)}$$

and $\mathbf{\Phi_{XX}}$, the covariance matrix of the vector $\mathbf{X}$, is identical to one in (A.10). The poles of $\Phi_{D_5}(s)$, the CF of D_5, are

$$p_1 = \frac{1}{2} + \frac{1}{2}\sqrt{\frac{(3\gamma_s + 4)(\gamma_s + 2)}{\gamma_s(3\gamma_s + 2)}}, \quad p_2 = \frac{1}{2} - \frac{1}{2}\sqrt{\frac{(3\gamma_s + 4)(\gamma_s + 2)}{\gamma_s(3\gamma_s + 2)}}. \qquad \text{(Type V)} \qquad \text{(A.19)}$$

Note that when the threshold is $T_0 = 0$, positive poles should be used to compute the pairwise error event possibility; refer to (2.31). Hence,

$$\begin{aligned} P_V = \Pr[D_5 \leq 0] &= -\sum_{RP\ poles} \Phi_{D_5}(s)/s \\ &= \frac{-p_2}{p_1 - p_2} \\ &= \frac{\sqrt{(3\gamma_s + 4)(\gamma_s + 2)} - \sqrt{\gamma_s(3\gamma_s + 2)}}{2\sqrt{(3\gamma_s + 4)(\gamma_s + 2)}} \\ &\approx \frac{2}{3}\gamma_s^{-1}, \qquad \gamma_s \to \infty. \end{aligned} \qquad \text{(A.20)}$$

Type VI error: symbols in both the transmitted and alternative pairs are different, $(\tilde{s}_A, \tilde{s}_B)$ differ from (s_A, s_B) in both positions, and one of (s_A, s_B) equals one of $(\tilde{s}_A, \tilde{s}_B)$.

This case can be defined by setting $s_A = 0$, $s_B = 1$, and $\tilde{s}_A = 2$, and $\tilde{s}_B = 0$. The probability of a Type VI error event, i.e $p(\mathbf{r}\,|\,s_A = 0,\ s_B = 1,\ u) < p(\mathbf{r}\,|\,\tilde{s}_A = 2,\ \tilde{s}_B = 0,\ u)$, is identical to that of a Type V error event, because both types have identical poles and threshold T_0. As a result,

$$\begin{aligned} P_{VI} = \Pr[D_6 \leq 0] &= \frac{\sqrt{(3\gamma_s + 4)(\gamma_s + 2)} - \sqrt{\gamma_s(3\gamma_s + 2)}}{2\sqrt{(3\gamma_s + 4)(\gamma_s + 2)}} \\ &\approx \frac{2}{3}\gamma_s^{-1}, \qquad \gamma_s \to \infty. \end{aligned} \qquad \text{(A.21)}$$

92

Table A.1 summarizes the poles and threshold for each type of error events for each of the three detectors in Chapter 2.

	Full-coherent	Non-Coherent	Partial-coherent
Type I	$p_1 = \frac{1}{4}\left(1+\sqrt{1+2\gamma_s^{-1}}\right)$ $p_2 = \frac{1}{4}\left(1-\sqrt{1+2\gamma_s^{-1}}\right)$ $\Pr[D < T_0],\ T_0 = 0$	$p_1 = 1+\gamma_s^{-1}$ $p_2 = -p_1$ $\Pr[D > T_0],\ T_0 = \ln\left(\frac{(1+\gamma_s)^2}{2\gamma_s+1}\right)$	$p_1 = \sqrt{1+\gamma_s^{-1}}$ $p_2 = -p_1$ $\Pr[D > T_0],\ T_0 = \ln\left(1+\gamma_s\right)$
Type II	$p_1 = \frac{1}{4}\left(1+\sqrt{1+4\gamma_s^{-1}}\right)$ $p_2 = \frac{1}{4}\left(1-\sqrt{1+4\gamma_s^{-1}}\right)$ $p_3 = \frac{1}{4}\left(1+\sqrt{1+\frac{4}{3}\gamma_s^{-1}}\right)$ $p_4 = \frac{1}{4}\left(1-\sqrt{1+\frac{4}{3}\gamma_s^{-1}}\right)$ $\Pr[D < T_0],\ T_0 = 0$	$p_1 = \frac{1}{2}\gamma_s^{-1}$ $p_2 = -1+\gamma_s^{-1}$ $p_3 = p_2$ $\Pr[D > T_0],\ T_0 = \ln\left(\frac{(1+\gamma_s)^2}{2\gamma_s+1}\right)$	$p_1 = -\frac{1}{2}+\frac{1}{2}\sqrt{1+\frac{4}{3}\gamma_s^{-1}}$ $p_2 = -\frac{1}{2}-\frac{1}{2}\sqrt{1+\frac{4}{3}\gamma_s^{-1}}$ $p_3 = -1-\gamma_s^{-1}$ $\Pr[D > T_0],\ T_0 = \ln\left(1+\gamma_s\right)$
Type III	$p_1 = \frac{1}{4}\left(1+\sqrt{1+2\gamma_s^{-1}}\right)$ $p_2 = \frac{1}{4}\left(1-\sqrt{1+2\gamma_s^{-1}}\right)$ $\Pr[D < T_0],\ T_0 = 0$	$p_1 = 2+\gamma_s^{-1}$ $p_2 = -\gamma_s^{-1}$ $\Pr[D < T_0],\ T_0 = \ln\left(\frac{(1+\gamma_s)^2}{2\gamma_s+1}\right)$	$p_1 = 1+\sqrt{1+\gamma_s^{-1}}$ $p_2 = 1-\sqrt{1+\gamma_s^{-1}}$ $\Pr[D < T_0],\ T_0 = \ln\left(1+\gamma_s\right)$

Type VI	$p_1 = \frac{1}{4}\left(1+\sqrt{1+4\gamma_s^{-1}}\right)$ $p_2 = \frac{1}{4}\left(1-\sqrt{1+4\gamma_s^{-1}}\right)$ $p_3 = \frac{1}{4}\left(1+\sqrt{1+\frac{4}{3}\gamma_s^{-1}}\right)$ $p_4 = \frac{1}{4}\left(1-\sqrt{1+\frac{4}{3}\gamma_s^{-1}}\right)$ $\Pr[D<T_0],\ T_0=0$	$p_1 = 1+\frac{1}{2}\gamma_s^{-1}$ $p_2 = -\gamma_s^{-1}$ $p_3 = p_2$ $\Pr[D<T_0],\ T_0=\ln\left(\frac{(1+\gamma_s)^2}{2\gamma_s+1}\right)$	$p_1 = \frac{1}{2}+\frac{1}{2}\sqrt{1+\frac{4}{3}\gamma_s^{-1}}$ $p_2 = \frac{1}{2}-\frac{1}{2}\sqrt{1+\frac{4}{3}\gamma_s^{-1}}$ $p_3 = -\gamma_s^{-1}$ $\Pr[D<T_0],\ T_0=\ln(1+\gamma_s)$
Type V	$p_1 = \frac{1}{4}\left(1+\sqrt{1+2\gamma_s^{-1}}\right)$ $p_2 = \frac{1}{4}\left(1-\sqrt{1+2\gamma_s^{-1}}\right)$ $\Pr[D<T_0],\ T_0=0$	$p_1 = 1+\gamma_s^{-1}$ $p_2 = -\gamma_s^{-1}$ $\Pr[D<T_0],\ T_0=0$	$p_1 = \frac{1}{2}+\frac{1}{2}\sqrt{\frac{(3\gamma_s+4)(\gamma_s+2)}{\gamma_s(3\gamma_s+2)}}$ $p_2 = \frac{1}{2}+\frac{1}{2}\sqrt{\frac{(3\gamma_s+4)(\gamma_s+2)}{\gamma_s(3\gamma_s+2)}}$ $\Pr[D<T_0],\ T_0=0$
Type IV	$p_1 = \frac{1}{4}\left(1+\sqrt{1+4\gamma_s^{-1}}\right)$ $p_2 = \frac{1}{4}\left(1-\sqrt{1+4\gamma_s^{-1}}\right)$ $p_3 = \frac{1}{4}\left(1+\sqrt{1+\frac{4}{3}\gamma_s^{-1}}\right)$ $p_4 = \frac{1}{4}\left(1-\sqrt{1+\frac{4}{3}\gamma_s^{-1}}\right)$ $\Pr[D<T_0],\ T_0=0$	$p_1 = 1+\gamma_s^{-1}$ $p_2 = -\gamma_s^{-1}$ $\Pr[D<T_0],\ T_0=0$	$p_1 = \frac{1}{2}+\frac{1}{2}\sqrt{\frac{(3\gamma_s+4)(\gamma_s+2)}{\gamma_s(3\gamma_s+2)}}$ $p_2 = \frac{1}{2}+\frac{1}{2}\sqrt{\frac{(3\gamma_s+4)(\gamma_s+2)}{\gamma_s(3\gamma_s+2)}}$ $\Pr[D<T_0],\ T_0=0$

Table A.1: Poles of the characteristic functions of different types of error events.